NAT'L INST. OF STAND & TECH R.I.C.
A11105 039622
NIST
PUBLICATIONS

United States Department of Commerce
Technology Administration
National Institute of Standards and Technology

NISTIR 5047

Cavity Coupling in Vertical-Cavity Semiconductor Lasers

David T. Schaafsma
David H. Christensen

QC
100
.U56
NO.5047
1997

NISTIR 5047

Cavity Coupling in Vertical-Cavity Semiconductor Lasers

David T. Schaafsma
David H. Christensen

Optoelectronics Division
Electronics and Electrical Engineering Laboratory
National Institute of Standards and Technology
Boulder, Colorado 80303-3328

January 1997

U.S. DEPARTMENT OF COMMERCE, Michael Kantor, Secretary
TECHNOLOGY ADMINISTRATION, Mary L. Good, Under Secretary for Technology
NATIONAL INSTITUTE OF STANDARDS AND TECHNOLOGY, Arati Prabhakar, Director

Contents

1 Introduction **2**

1.1 Preface 2

1.2 Motivation 6

1.2.1 The Science of VCSELs 6

1.2.2 VCSEL Technology 8

1.2.3 VCSEL Metrology 11

1.3 Contributions of This Work 12

2 History and Literature Survey **14**

2.1 Pertinent Histories 14

2.2 Multilayer Optics 14

2.2.1 Modeling Techniques and Optimization 14

2.2.2 Refractive Indices in III-V Compounds 15

2.3 Image Theory and Green's Functions 16

2.4 Cavity Electrodynamics 17

2.5 Vertical-Cavity Semiconductor Lasers 19

2.5.1 Cavity Electrodynamics in VCSELs 20

3 Theoretical Background **21**

3.1 Coupling Problems in VCSELs 21

3.2 Mode (Rabi) Splitting 21

3.2.1 Quantum Mechanical Solution 23

3.2.2 Classical (Linear Dispersion) Theory 24

3.3 Radiation Intensity Patterns and Localization Effects 25

3.3.1 Fresnel Analysis 25

3.3.2 Near-Field Limitations 28

3.4 Miscellaneous Relevant Cavity Quantities 29

3.5 Comments 31

3.5.1 Redistribution versus Enhancement 31

3.5.2 Estimation of Magnitudes 32

4 Cross-Sectional Photoluminescence **34**

4.1 Surface-Normal and Cross-Sectional Emission from VCSELs 34

4.2 Description of Tube-Length-Conjugate System 34

4.2.1 Resolution of the Probe 35

4.3 Description of Infinite-Conjugate System 38

4.3.1 White-Light Reflectance Scanning 39

4.3.2 Polarization-Resolved Measurements . . . 40
4.3.3 Surface-Normal Pumping . . . 41
4.4 General XPL Considerations . . . 44
4.4.1 Probe Absorption . . . 44
4.4.2 Waveguiding and Field of View . . . 47
4.5 Ancillary Measurements . . . 48
4.5.1 Spectral Reflectance . . . 48
4.5.2 Double-Crystal X-ray Diffraction . . . 49

5 Emitter Coupling **50**
5.1 VCSEL Cavity Effects and Side Emission . . . 50
5.2 Top- and Side-Pumped XPL . . . 50
5.2.1 Eliminating Competing Processes . . . 51
5.2.2 Measurements in VCSEL Cavities . . . 53
5.3 Modeling the Data . . . 55

6 Mode Coupling **57**
6.1 The Microwave Cavity Experiment . . . 57
6.1.1 Experimental Description . . . 57
6.1.1.1 The Cavity. . . . 57
6.1.1.2 Antenna and Detector. . . . 59
6.1.1.3 Pulses and Causality. . . . 61
6.1.1.4 CW Measurements. . . . 63
6.2 Microwave Results . . . 63
6.2.1 Predictions . . . 63
6.2.2 Pulsed Transmittance Data . . . 65
6.2.3 CW Transmittance Data . . . 66
6.2.4 CW Electrical Reflection Data . . . 68
6.3 Analysis . . . 68
6.3.1 Anomalous Localization Dependence . . . 70
6.3.2 Feedback in Planar Cavities . . . 71

7 Cavity Coupling in VCSELs **72**
7.1 Multimode VCSEL Experiments . . . 72
7.1.1 Specimen Descriptions . . . 73
7.1.2 Emission Models . . . 77
7.1.3 Reflectance Metrology . . . 78
7.2 Multimode VCSEL Results . . . 78
7.3 Analysis . . . 84

7.3.1 The Three-Color VCSEL 84
7.3.2 The Two-Cavity VCSEL 86

8 Conclusion **88**
8.1 Contributions 88
8.2 General 89

References **90**

Appendix A Interdiffusion in GaAs Quantum Wells **99**

Appendix B Multilayer Modeling **103**
B.1 Modeling Optical Response in VCSELs 103
B.1.1 Reflectance Spectra and General Prescriptions 103
B.1.2 Emission Modeling 104
B.1.3 Index Models 105
B.1.4 Pump Field Distributions 110
B.2 Measurement and Modeling Results 112
B.2.1 Determination of Construction Parameters 112
B.2.2 Pump Field Weighting 113
B.2.3 Angular Integration 113
B.2.4 Coherent and Incoherent Summation 117

Appendix C Computing Energy Levels in Semiconductor Quantum Wells **119**

Appendix D The Image Method in Plane-Parallel Geometries **126**
D.1 The Method of Images for a Fabry-Perot Etalon 126
D.2 The Region of Interest 127
D.3 Partially-Reflecting Mirrors 129
D.4 Experimental Results 130
D.5 Return to Validity 134

CAVITY COUPLING IN VERTICAL-CAVITY SEMICONDUCTOR LASERS

David T. Schaafsma

David H. Christensen

National Institute of Standards and Technology
325 Broadway
Boulder, CO 80303

Abstract

The growing sophistication of vertical-cavity surface-emitting lasers, or VCSELs, has fostered questions which have previously lacked a certain relevance. In particular, the gain medium in the laser can now be confined to a very small region of space and moved about within the cavity, and the mode volume of the cavity itself can be reduced to a scale where coupling between the source medium and the emitted radiation and even the quantum nature of light can become significant. This work explores two types of coupling in planar cavities: emitter coupling, a light-matter interaction; and mode coupling, a light-only interaction. Technological applications of coupling effects are discussed, along with novel metrology designed for devices such as VCSELs. A novel experimental technique for probing the side-emission from VCSELs is also described and is used both to probe for coupling effects and to serve as a metrological tool.

Experiments designed to probe for emitter coupling in VCSELs are described and their results show that the effect of the cavity on the emitter can indeed be seen in side emission studies. The results of this experiment show side emission to be a versatile tool not only for examining cavity effects but also for basic metrology and modeling of optical response.

The general effects of mode coupling are illustrated in a simplified experiment designed to show the strong redistribution of energy from a dipole inside an etalon, which is much more pronounced than the normal etalon redistribution effects for light originating outside the cavity. These tests also show that redistribution of intensity patterns does not indicate feedback to an emitter from its own radiation. This type of coupling to cavity modes is then examined in VCSEL structures and shown to be potent enough for device applications.

Keywords: (vertical-cavity) semiconductor lasers, cavity electrodynamics, photoluminescence, Rabi oscillation, cavity modes, multilayer modeling, compound semiconductor metrology.

1 Introduction

1.1 Preface

Vertical-cavity surface-emitting lasers (VCSELs) have been the subject of great technological and scientific interest since the first part of this decade, when relatively simple and reliable fabrication of these devices was realized. Their obvious advantages over edge-emitting technology, notably in the areas of device fabrication tolerances, array production, and overall quality of the optical output, make VCSELs the clear choice for application in long-range, optical-fiber-based telecommunications systems, optical storage readout, optical-gate arrays, smart pixels and a host of other optical computing, communications, and basic science applications. The ease of fabricating large, high-density arrays of VCSELs makes them ideally suited to the demands of multiplexed optical systems. Their superior mode structure and low beam divergence are distinct advantages in nearly any configuration where light is to be transmitted down an optical fiber or into free space.

VCSELs do, however, possess a number of unique qualities that edge-emitting diode lasers and even conventional lasers (such as gas or dye) do not. Foremost among these are the VCSEL's ability to have its gain medium — usually some configuration of quantum wells (QWs) — located with high precision anywhere within (and possibly without) the cavity and its epitaxial limitation on the length of the cavity, which allows it to have extremely low mode volumes, on the order of one cubic cavity-resonance wavelength. Though these two properties, gain localization and small mode volume, have been realized separately in other systems in the past, VCSELs were the first to unite the two.

Perhaps the greatest benefit of this union is an increase in mode control. The cavity length of an edge-emitting diode laser (or any of the surface emitters whose cavity lies in the plane of the wafer) is limited by fabrication tolerances. This means that the mode volumes in these devices are very large, and the free spectral range is very small (often, a large number of wavelength modes will fit within the gain spectrum, as shown in Fig. 1). In contrast, the cavity length of a VCSEL is limited only by epitaxial growth technology, which today can produce single monolayers with precision. VCSELs are thus most often true single-mode devices, wherein only a small portion of the total gain spectrum is used in the lasing mode (Fig. 2).

Lowering the mode volume of a laser also allows for the possibility that the feedback from the mirrors can influence the atom (or whatever source is used) during the interval when the decay is taking place. This is entirely different from the interference that makes the cavity such a strong pass filter; it is a true photon-atom interaction (in the case of semiconductor structures, the "atomic" system is usually identified with an exciton). The manifestations of this phenomenon can have a sizable impact on the emission from the device, both spontaneous and stimulated, possibly even inducing "thresholdless lasing," where the curve of light intensity versus injected current lacks the change in slope that usually marks the onset of lasing. This type of effect, where the emitter's own radiation can change its properties, will be called "emitter coupling" or "feedback" in this work.

Moving the emitter about in the cavity (or changing the length of the cavity) leads to

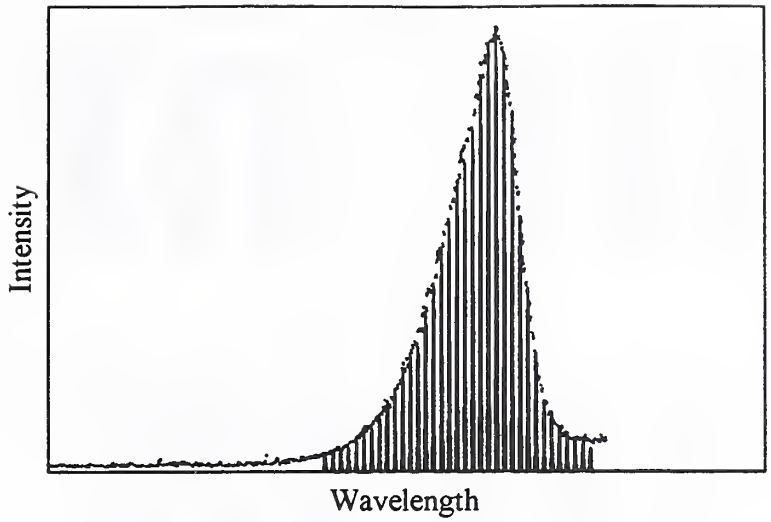

Figure 1: The mode spectrum of a typical edge-emitting diode laser, illustrating the overlap of gain and cavity modes. The dashed line is the gain envelope (QW spontaneous emission) and the solid line is the output of the device.

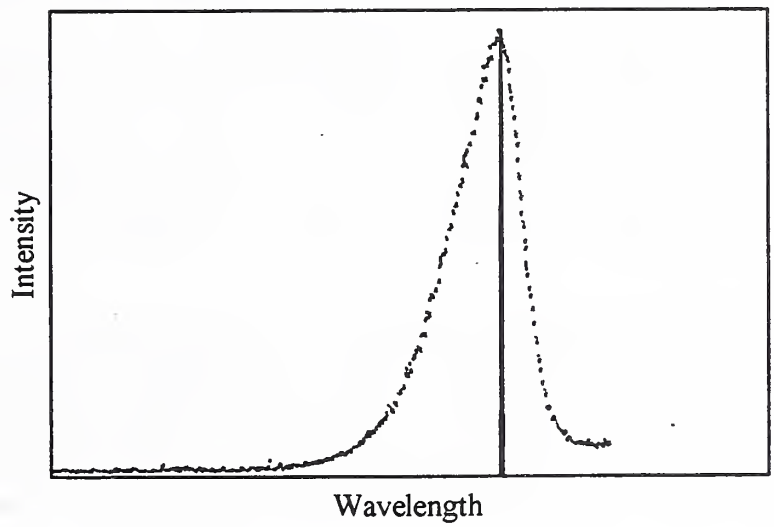

Figure 2: The mode spectrum of a typical VCSEL device, showing true single-mode operation. Again, the dashed line is the QW emission.

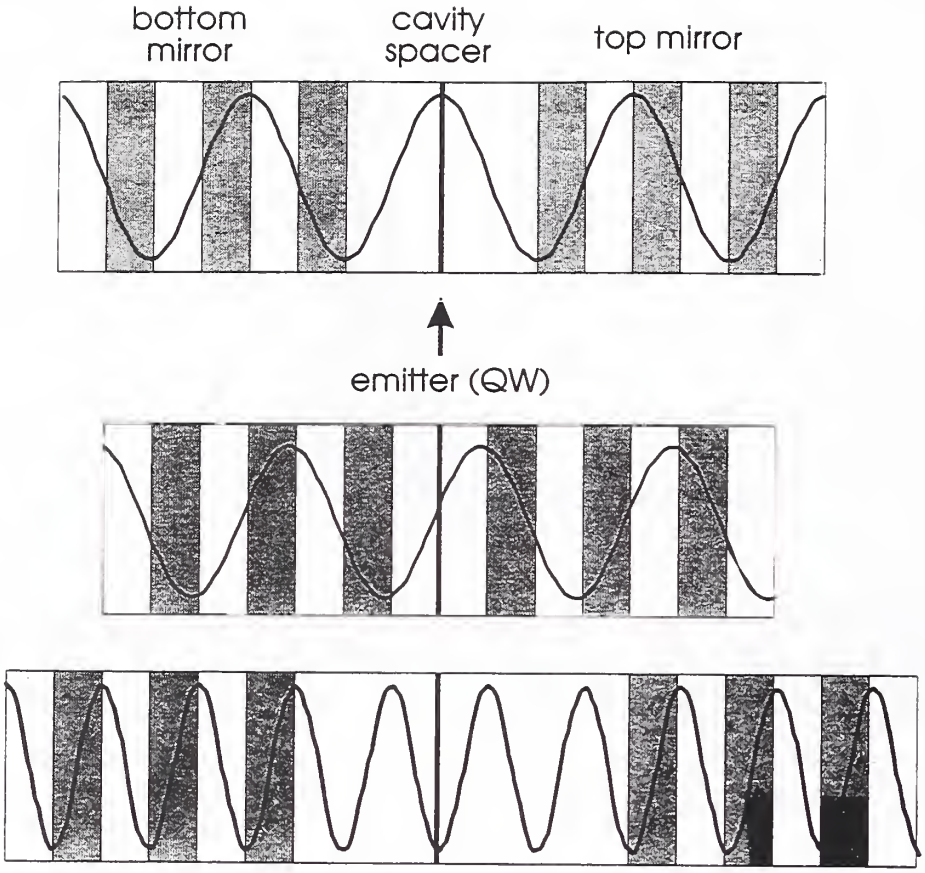

Figure 3: Mode coupling in a VCSEL. The single-wavelength cavity (top) allows light from the dipole at its center to couple strongly into the mode; the half-wave cavity (middle) does not. As shown in the third schematic (bottom), this is not limited to half- or whole-wave cavities, but is just a manifestation of the relative position of emitter and standing field. Since the magnitude of the field at the position of the dipole is of importance to emitter coupling, this type of localization also impacts atom-cavity effects.

another type of coupling, which in this context will be called "mode coupling" or "interference." This effect represents nothing more than a change of the emitter position relative to the standing mode field of the cavity (Fig. 3). Light from an emitter positioned at an antinode of a given mode will couple strongly into that mode, whereas light originating at a node position will not. The primary manifestation of this effect is a change in the intensity of the light output in a given direction, which in turn has a number of technological consequences.

One of the less desirable properties of VCSELs has been their low maximum power output. Fortunately, conventional VCSEL design allows for quite a bit of freedom to increase the total gain volume in the laser. As a greater number (higher density) of emitters helps to minimize optical and electrical losses, there is ample motivation to try and increase the density of QWs in the laser cavity. Throughout the history of diode lasers, multiple quantum wells

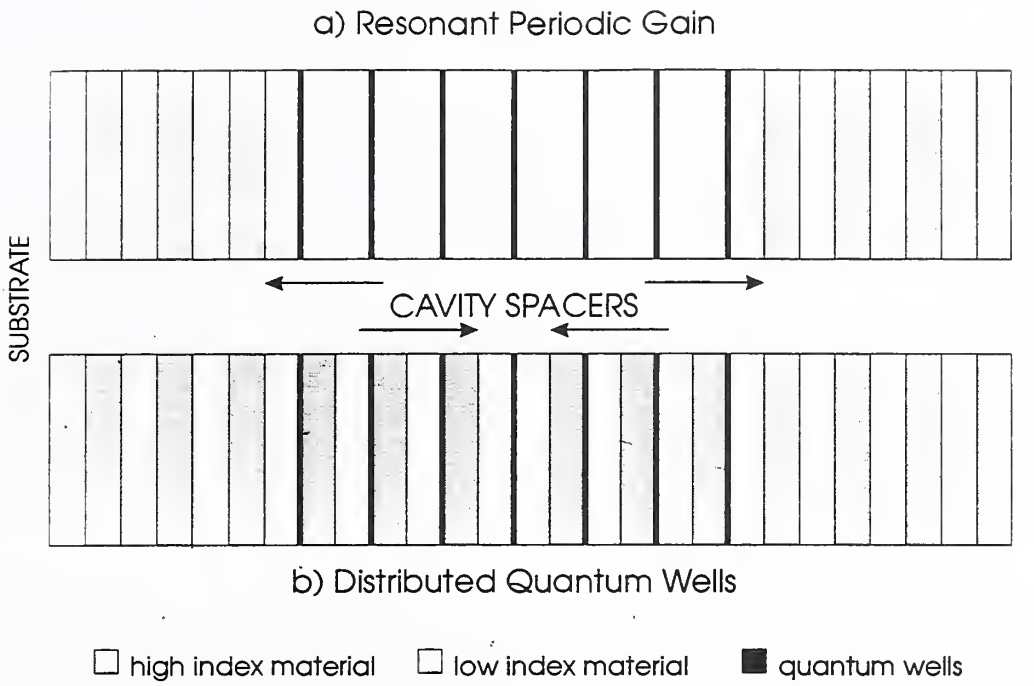

Figure 4: VCSEL schematic, showing distributed-gain techniques.

(MQWs) have been used to augment the power output of the device. This scheme has been employed in VCSELs as well, but it was realized early in the development of the VCSEL[1, 2] that the QWs could now be positioned advantageously in the standing wave of the cavity, as shown in Fig. 4. Specifically, a QW at an antinode of the resonant field experiences greater excitation and re-excitation from the laser build-up in the cavity than one at a node. This configuration of the QW emitters, at half-wave intervals, came to be known as "resonant periodic gain" (RPG), since the standing wave antinodes of the resonant field and the gain sheets were coincident. (In fact, this placement of the emitter in the standing wave can also lead to one type of "enhancement" and "suppression" of the spontaneous emission.) Since the standing wave extends throughout the device, and since the cavity boundary can be ill-defined in distributed feedback (DFB) devices, the point at which the effects of localization disappear is equally unclear.

There are thus two basic ways that a QW (or light emitted from one) can couple to the cavity of a VCSEL: emitter (light-matter) coupling and mode (light-only) coupling. The primary objective of this work was to ascertain how to distinguish and measure feedback (emitter coupling) and interference (mode coupling) effects in VCSELs. As an added dividend, the results obtained also shed light on how well the model of a simple Fabry-Perot with "hard" mirrors (single interfaces) stands up to the complexities of distributed feedback and dispersive semiconductor materials, and helped to develop metrology valuable to the use

of these phenomena to make improved or novel VCSEL devices.

1.2 Motivation

It might be said that science and technology, unlike emission processes in VCSELs, cannot be decoupled, and this is certainly the case in this work. In seeking the answers to basic science questions, new metrology for VCSELs had to be developed, that new areas of technology might be better understood and exploited, though it might just as well have been the other way around.

As might be expected for any project involving compound semiconductors, it was impossible to confine everything to the traditional demesne of physics and not to call on engineering and materials science. The following sections attempt not to delineate where these different disciplines might be confined, but to show where they could be applied to the demands of understanding, designing, and producing VCSELs.

1.2.1 The Science of VCSELs

Often in the history of science, an understanding of basic phenomena has led directly to improved technology and certainly this has been true of semiconductor and laser science. In the case of microcavity lasers, much of the science has been understood for some time, but remains esoteric to modern applications or has not been clearly delineated. In addition, the complexity of the physical properties of semiconductor materials, not to mention the complexity of the devices themselves, only augments the uncertainty as to which measurable property belongs to which physical phenomenon.

One ambiguity that I intend to address here is the distinction between feedback and interference in a cavity, as referred to above; that is, between photon-atom and photon-photon coupling effects. The first of these, the photon-atom (or atom-cavity or light-matter or emitter coupling) effect, is the fulcrum of the burgeoning field of cavity electrodynamics, the origins of which date back to the 1940s and 50s (see Ch. 2 for a complete review of these) — at which time research was concerned exclusively with atomic systems, with discrete energy levels. Naturally, many idealizations — such as single atom systems and perfect mirrors — do not apply to VCSELs, but even in the simplified picture, it is not casually obvious how to discern some of the effects due to feedback (emitter coupling) from those due to interference (mode coupling). Since intensity distribution (and hence emission rate) of light from a Fabry-Perot structure is angularly and spectrally dependent, one might infer that the decay rate at a given frequency could vary with angle. Yet this goes against a fundamental physical viewpoint that scalar quantities like energy and decay rates cannot have vectorial dependence. Even if intensity changes can be correlated with certain cavity conditions, does a change in emitted intensity necessarily imply a feedback process at work?

It is also logical to expect that if feedback did occur, and a means existed to observe the emitter without the distortion of the mirrors, then changes in the emitter itself (such as an alteration of its decay rate or a shift in its energy levels) should be observable from any point relative to it. That is to say, if an observer could "stand inside" the cavity and look at the

radiation source, without the distortion of the mirrors, he should still see changes in its decay rate, or its energy levels, or whatever other manifestation of feedback had occurred. The point is that most of the observables that change as a result of feedback are *scalars*: energy levels, decay rates, and lifetimes. These quantities should not change with the direction of observation. Most notably in the case of planar cavities, this type of modification should be observable in side emission, as will be shown by the data in Ch. 5.

Even when feedback does not occur, the emission pattern can change. The simplified Fresnel-reflection analysis (of a point dipole between two mirrors) presented in Ch. 3 shows that modified intensity patterns arise regardless of the nature of the source of the radiation. If light could simply be "injected" into a cavity at a specific point, this analysis shows that the energy would still redistribute in predictable fashion. This redistribution follows the normal behavior of a Fabry-Perot etalon, save for the fact that it is much more pronounced when the source is inside the cavity. Though the problem of the dipole inside the cavity differs somewhat from the dipole outside, and we might expect entirely different behavior, there is some justification for believing that they should not differ significantly.

As discussed in Appendix D, the image method approach to solving the idealized dipole-in-a-plane-parallel-cavity problem suggests a symmetry which is somewhat counter-intuitive. Specifically, this theory predicts that a dipole a fixed distance outside the cavity, say a half of the cavity length, should see the same mode spectrum as one a half cavity length inside the cavity. The pure simplicity of this problem suggests that it should be very easy to test, and the results of that test (described in part in Ch. 6) will be discussed with the theory in Appendix D.

In general, VCSELs present a unique opportunity to study cavity electrodynamics in visible lasers with very low mode volumes and localized gain media. This means that certain problems of broadening as present in gas lasers and the low free spectral range of conventional diode lasers can be dispensed with. The uncontrollable gain medium present in gas lasers can be replaced by quantum wells that can be grown in any location in the device. The mirrors and the cavity can be grown to accommodate a large range of lasing wavelengths, and the device can be designed to operate in a sizable temperature regime (primarily limited by the shift of the gain peak; about 0.32 nm/°C for GaAs with typical peakwidths of 10–15 nm). The VCSEL, from a rather idealized physical point of view, is a nice laboratory for cavity and quantum phenomena.

Of course, this idealization breaks down very quickly due to the distribution of the cavity (mirror) feedback. In DFB structures, the question of where the cavity ends becomes much more relevant. Though the length of the cavity spacer itself can be made extremely small, the effective cavity length may remain large. Does the distribution of feedback in the mirrors, which leads to the discrepancy between spacer and effective cavity lengths, have an impact on coupling phenomena? Is this effect limited to the larger mode volume described by the effective cavity length or is there a more subtle effect arising from distributed feedback rather than single-interface, "hard" mirrors? Whether the image symmetry mentioned above holds or not, what difference is there when the hard mirrors are replaced with distributed ones? Is the effective cavity length a distinct boundary between regimes or a vague one?

This work will address the question of distinguishing interference and feedback effects in planar cavities (in Ch. 5 and Ch. 6) and will examine their impact on VCSEL design. At the heart of these issues is a novel measurement technique which has a large number of uses in VCSEL metrology (which will be elucidated in Ch. 4).

1.2.2 VCSEL Technology

Whereas the scientific questions pertinent to distributed mirrors, low mode volumes, and localized emitters may seem irrelevant to making a simple VCSEL, their relevance to VCSEL applications, and to advanced VCSEL design, is acute. To begin with, the position of the emitters within the device has a sizeable impact on performance, and there are other areas where VCSEL properties might benefit from this sort of design refinement.

A fine example of this is the RPG VCSEL of Sec. 1.1, which has great gain enhancement, lower amplified spontaneous emission, and stability advantages[3] over its single- and multiple-quantum well counterparts. However, RPG VCSELs have the distinct disadvantage that no one has yet been able to pump them electrically. A thorough understanding of optimal dipole placement in these structures might allow a design whereby the gain could be moved to accommodate the required electrical design. Beyond the minimum requirement of an electrically controlled unit, the design could be further optimized for ultrafast operation[4], greater thermal stability, or lower device aperture size.

Yet even in non-RPG devices, the localization issue is relevant. Since the VCSEL is in essence a Fabry-Perot cavity, its resonance shifts with the angle of light propagation relative to the wafer normal. This is conducive to low-divergence, single-mode lasing, but not to array applications where beam steering is desirable, nor does it make the VCSEL array a very forgiving device where optical alignment is concerned. If the transverse modes could be controlled by moving the quantum wells to different locations in the mode field, a great many applications would benefit.

Dipole localization might even allow the VCSEL designer to harness different spectral and spatial modes in a single device. Figure 5 illustrates a proposed three-color output device that could be used for wavelength-division multiplexing or a number of other multichannel applications. Each of the three QWs in the structure is tuned to a different cavity mode, so each must be placed at an antinode of its respective mode field. Due to dispersion, these fields will not be simple harmonics, so the spacing of the QWs within the cavity is uneven. Though there are some technical difficulties with this design — the outer ring of the structure must be ion-implanted or coated with an insulator to prevent the sidewall contacts from shorting the three quantum wells together and the lithographic tolerances in the vertical direction are extremely small — it illustrates the point of what technological advances might come about using dipole localization.

Another device application which has been explored recently in the literature[5] is the coupled-cavity VCSEL, shown in Fig. 6. The advantages of this device are both scientific and technological: it is a system of as many as four discrete, coupled oscillators as well as a way to get several discrete modes in a VCSEL by growing two single-wavelength cavities rather than one 16- or 20-wavelength cavity. In addition, the device can be electrically driven,

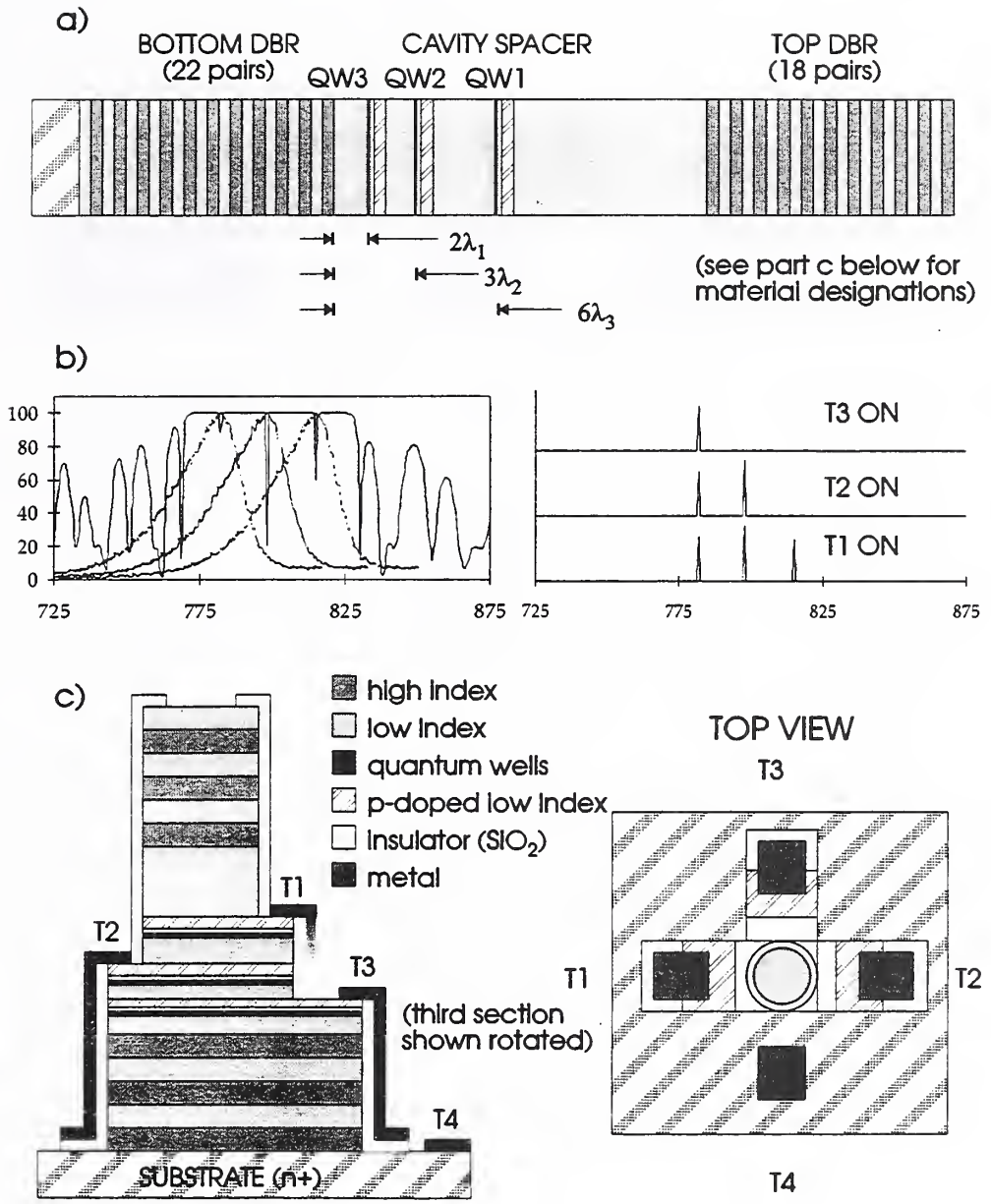

Figure 5: A three-wavelength, four-terminal VCSEL. Top (a): index/material schematic. Middle (b): simulated reflectance spectrum (solid line) and QW gain curves (dashed). Bottom (c): elementary process diagram for isolating the individual gain media.

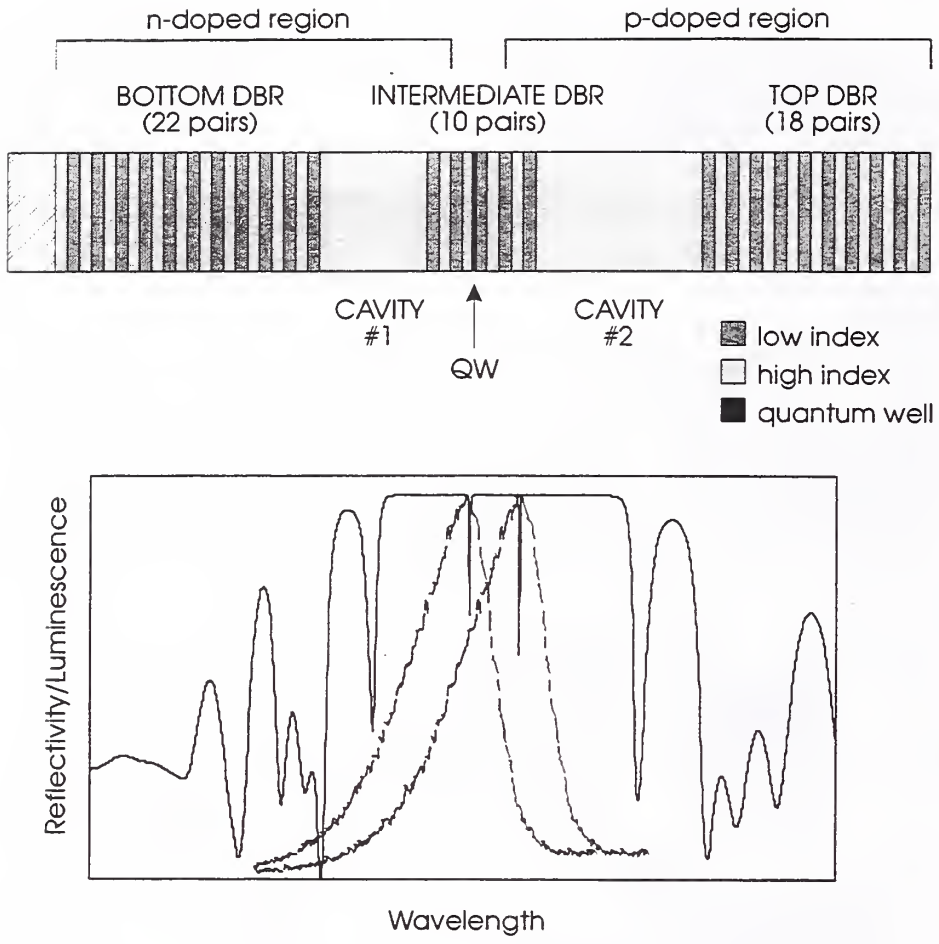

Figure 6: A coupled-cavity VCSEL design.

unlike other devices with quantum-well active media in both cavities. However, the success of this device depends on how well the quantum well in the intermediate mirror can couple to the modes of the two cavities, a topic which will be addressed in Chs. 6 and 7.

Like dipole localization, the lowering of mode volume also plays an important technological role. Since VCSELs with nearly perfect spontaneous coupling produce some highly squeezed statistical states[6, 7], avoiding or maximizing the feedback effect becomes important for design. Just as "true" lasers — producing minimum-uncertainty radiation — are often desirable, the anomalous statistics of a squeezed state device can be equally beneficial. If the coupling into the lasing mode becomes nearly perfect, the threshold should decrease, which has a number of implications for small-signal and high-frequency applications.

One mechanism at the VCSEL designer's control is of course the mirrors themselves, which can be made to lengthen the effective cavity, to grade it, or to sharpen it with higher-contrast layers[8], thus increasing the confinement and possibly the spontaneous coupling. Though somewhat difficult to achieve in epitaxial semiconductor structures, an ideal, three-dimensional cavity would further increase the spontaneous coupling into the fundamental mode[9], lowering the noise figure of the device dramatically.

Yet for a basic understanding of these phenomena, and in particular to connect them with emitter coupling, there is the condition that we must be able to determine unambiguously when such coupling has occurred. In order to manifestly attribute thresholdless lasing, for example, to atom-cavity coupling, it behooves us to produce unequivocal evidence of atom-cavity coupling. Chapter 5 identifies a means for doing so in VCSEL structures.

1.2.3 VCSEL Metrology

A typical VCSEL structure (if one can be said to exist any more) might consist of three or more compound semiconductor materials and from 60 to 200 individual epitaxial layers, all requiring anything from 5 to 20 hours to grow. For production devices, particularly arrays, the tolerances in thickness, alloy composition, dopant level, and interface abruptness are very small, often 1 to 2%. This means that the process control must be very good, and in turn this places a large burden on characterization techniques.

Ultimately, in-situ characterization is most desirable since it can provide instant feedback to the crystal grower and the run can be optimized or the design can even be modified to accommodate growth discrepancies "on the fly." However, much of the in-situ characterization, especially for complex devices such as VCSELs, relies on established ex-situ techniques and modeling.

Of particular importance to semiconductor laser fabrication is the match between the wavelengths of cavity resonance and QW emission. The QW thickness is in this case only part of the equation, since high-efficiency lasers require good interface quality and uniform barrier profiles as well, so techniques such as reflection high-energy electron diffraction (RHEED) can give only part of the picture.

Traditional metrology has long used surface-normal photoluminescence (NPL) as a probe of quantum-well emission wavelength (thickness) and interface quality. In the case of complex multilayer structures, however, the transmission response of the layers themselves can

obscure this information, and in VCSELs this effect is most pronounced. A probe which is insensitive to the cavity effects is thus required; for the plane-parallel geometry of VCSELs, a side-emission measurement, looking at the quantum well luminescence along a direction perpendicular to the cavity axis, appears to fill this role nicely, (and does, in fact, as explained in Ch. 4).

Given this "native" (unperturbed) emission and the proper models for the structure, it is possible to simulate a surface-normal spectrum from the data. Obviously, if this process works in this direction, it can be expected to work in reverse, and thus the cavity-to-quantum-well mismatch information could be obtained from surface-normal photoluminescence and reflectance spectroscopy, both non-destructive techniques which can be easily adapted for in-situ application. This model, developed as described in Appendix B, was unique in semiconductor laser literature in its synthesis of complex refractive index data, including accurate index dispersion for quantum wells, and inside-out Fresnel calculations. In addition, information about other trends (such as thickness and alloy content uniformity) and about basic processes (such as coherent coupling of emitters in arrays and the effect of the QW interfaces in the multilayer response) can be gained from various simple modifications to the basic multilayer model. The nondegeneracy of reflectance and luminescence simulation makes both of them valuable in the fine-tuning of VCSEL structures.

This technique of measuring side-emission in semiconductor structures, which I have called cross-sectional photoluminescence or XPL, can also be used to ascertain other information about VCSELs, such as alloy content uniformity (and even the alloy content itself, which can also be obscured by the transmittance of the mirrors). This surprisingly simple method of turning a cleaved wafer on edge and looking at luminescence from the edge can also yield a great deal of information in applications other than VCSELs (such as interdiffusion, as documented in Appendix A).

Understanding the effects of dipole localization in distributed feedback structures could also contribute to enhanced metrology for periodic gain devices, or for devices such as those shown in Figs. 5 and 6. It is a simple matter to allow the multilayer emission model to account for emitters in the DBR (as in Appendix B), and to account for the various nuances of such configurations. Based on this type of refinement to the model, different, simple measurement techniques could be employed to further reduce the uncertainty in the determination of construction parameters. At the end of the day, these improvements in metrology could also help to foster greater flexibility and efficiency in VCSEL design and application.

1.3 Contributions of This Work

This thesis deals with two types of cavity coupling which occur in VCSEL devices. Underlying this simple delineation of two experimental paradigms is another experiment which played a crucial role in the success of the first two.

This experiment was in fact a detailed examination of cross-sectional luminescence from VCSELs, a technique originally developed in order to determine the match between QW emission and cavity resonance and later extended to facilitate emission modeling in VCSELs,

as described in brief in the preceding section. As documented in Appendix A, this in itself was novel at the time (as documented in Ref. [10]).

The quest for evidence of emitter coupling in VCSELs, really the second major experiment (or theme) in this work, was greatly abetted by side emission measurements. As shown in Ch. 5, side emission can indeed provide unambiguous identification of cavity-induced effects, especially when aided by such simple enhancements as polarization control and variable pump orientation. This work is the first to report such measurements clearly identifying cavity effects in the side emission from VCSELs.

The third experiment was in fact two experiments designed to demonstrate and clarify the effects of mode coupling, both in generic planar cavities and in VCSELs. First, a large-scale mock-up of a microcavity was constructed for a microwave emitter, which was then placed at various locations inside and outside of the cavity. Experiments were performed using a pulsed source (to prevent feedback) as well as a conventional continuous-wave source (to encourage it). Though similar to an experiment by Dowling and co-workers[11], this experiment was unique in that it compared pulsed (no-feedback) measurements with continuous-wave (feedback-possible) ones. The results of these tests have notable implications for VCSELs.

The second part of the mode coupling investigation shifted the focus back onto real VCSEL structures. Having established the basic properties of mode coupling, I applied the results of the first part of the experiment to cavities with distributed mirrors. As expected, the transition to external-cavity behavior in a VCSEL was much less abrupt than in a cavity with single-interface mirrors. This was not only the first extension of the periodic gain concept to gain outside the effective cavity length, but also the first study of the practical aspects, namely coupling the gain to the cavity, of discrete-mode (taken here to mean a few isolated modes, in contrast to the conventional interpretation of the term "multi-mode" as applied to edge-emitting diode lasers, which implies a nearly-continuous spectrum of modes) VCSEL design.

To summarize, the novel parts of this work are:

1. First documentation and demonstration of a novel measurement technique for semiconductor heterostructures — cross-sectional photoluminescence (XPL) — and first measurement of side emission from VCSELs.

2. First application of XPL and XPL depth-profiling to the metrology of buried-layer semiconductor structures.

3. First extension of conventional multilayer modeling techniques to the problem of light emission inside a multilayer dielectric resonator.

4. First observation of cavity-induced effects on the side emission from a quantum well in a VCSEL cavity.

5. Assessment of side emission as a tool for probing cavity coupling effects in VCSELs.

6. First comparison of pulsed (no-feedback) and continuous-wave (feedback) emitters in a plane-parallel resonator.

7. First experimental test of coupling of quantum wells in DBRs to cavity modes.

2 History and Literature Survey

2.1 Pertinent Histories

The subject of VCSELs covers several (traditionally) disparate areas of research; it therefore seems appropriate to present a relevant selection of the history of each of them. In particular, there is a great wealth of information on thin film optics of which a small part pertains to growing and modeling multilayer films of complex refractive index. The theory of images, which represents a part of the motivation for one of the experiments in this thesis, has also been given extensive treatment in the literature. Then there is nearly 50 years of research on cavity electrodynamics (of which a sizable percentage is relevant to the part of this work devoted to finding and discerning different cavity effects) and of course, nearly a decade of intense VCSEL development to be considered.

2.2 Multilayer Optics

The attention given to the problem of light incident on a number of boundary surfaces has been second only, perhaps, to that given the simple harmonic oscillator. It was therefore surprising to discover that no one had abandoned the assumption that the light had to originate outside the system of boundaries. In all the works cited, there is no explanation of or reference to a simple Fresnel-reflection solution to the problem of light originating inside of a system of plane-parallel interfaces (even as few as two). In addition, even with the number of publications concerned with refractive indices for compound semiconductors, choosing models and data that are consistent is still quite difficult.

2.2.1 Modeling Techniques and Optimization

Though the 19th century witnessed the advent of micro-interferometric devices such as the Fabry-Perot etalon[12], the origins of today's modeling techniques for multilayer structures date back to the early 1940s, when the discoveries of Langmuir and Blodgett[13] effectively opened up the field of thin film optics. (Of course, boundary value problems in general had been given exemplary treatment for some time[14, 15].) As thin film manufacturing processes became more and more refined[16] and the interest in anti-reflection coatings on glass grew, theoretical studies flourished in the middle to late 1940s. Though many authors published works on the theory of reflection and transmission of thin films[17, 18, 19, 20, 21], the truly definitive work in this area, for its clarity of both thought and notation and for its completeness, is that of Crook[22].

Designing a filter to have a certain spectral response requires an optimization technique or some kind of curve-fitting algorithm. Most of these are amenable to matrix-method

calculations[23, 24]. This optimization can be accomplished a number of ways from comprehensive searching[25] to taking the inverse Fourier transform of the spectral response to obtain the spatial index distribution[26]. Unfortunately, the latter method has been made to work only for nonabsorbing layers.

For determining construction parameters or fitting previously measured data with a simulated response, the method of attack is nearly analogous. Typical approaches to fitting include the common least squares[27] and finite difference[28] methods, the method of steepest descent[29], Monte Carlo iteration[30], and various techniques for double- or repeated-layer systems such as group optimization[31]. In general, better fits result from a better knowledge of material parameters.

However, even with accurate material parameters and more sophisticated mathematical algorithms, most of these methods are still somewhat "brute-force" approaches. A great many fits to optical response can be greatly improved by the application of some simple physical conditions such as thickness gradients or reflections off of the back surface of the substrate, as documented later in this work (App. B). With recent advances in artificial intelligence, this type of fitting algorithm should be compatible with common desktop computers. Given this sort of technology, in-situ characterization of VCSEL structures could provide a level of process control several orders of magnitude greater than what is currently available.

2.2.2 Refractive Indices in III-V Compounds

All of these optimization methods perform best when used with material systems whose refractive indices are well-known. In the realm of III-V compound semiconductors, only gallium arsenide has been given extensive experimental study in this area. A great deal of attention has been paid to modeling the refractive index dispersion of the $Al_xGa_{1-x}As$ system[32, 33, 34, 35, 36, 37], but the data for the entire system are sparse and lacking in consensus[38, 39, 40, 41, 42]; agreement between measurements is rarely better than 5–10%[43]. Very little index data exist for the $Al_xGa_{1-x}As$ system (for $x > 0$) at wavelengths longer than about 1.1 μm. There is still considerable debate as to where the $Al_xGa_{1-x}As$ X-band minimum crosses past the Γ minimum as the aluminum content in the alloy increases[44, 45] and the relations for the band minima as functions of composition[46]. Cardona and coworkers at the Max Planck Institute have made several ellipsometric studies of various III-V systems[47, 48, 49, 50, 51] to determine the temperature dependence of their critical points. Yet even these results are difficult to apply because the authors do not disclose the critical-point parameters.

The importance of an accurate knowledge of refractive indices in optimization and design of structures such as VCSELs has been underscored by Christensen et al.[52] and Hickernell et al.[53]. In structures with a large number of emitters (quantum wells), such as multiple-quantum-well or resonant-periodic-gain VCSELs, the index dispersion of the quantum wells can play a major role in modeling the optical response[53]. Excitonic features in the QW index spectrum can lead to reflectance features that cannot be fit using normal bulk index models. A great deal of theoretical work has been done on the modeling of GaAs QW

indices by Leburton[54, 55], and these models have been put use in the modeling efforts at NIST[53, 56].

2.3 Image Theory and Green's Functions

The method of images dates back to the dawn of electromagnetic theory in the mid-19^{th} century[57, 58]; the problem of radiating images was pioneered by Sommerfeld[59] to explain the propagation of radio waves along the surface of the Earth. The application of images to the particular problem of a source between mirrors is surprisingly recent, however.

One of the first publications of this sort was a brief discussion by Fong and Kittel[60] in which a solution to the charge induced on a pair of capacitor plates was given (without derivation) as an infinite sum of Bessel functions. Pumplin's paper[61] of 1969 (later amended by Glasser[62]), used an image series to solve for the potential of a point charge between two infinite conducting plates. This solution was claimed to be valid only *between* the plates, as strictly specified by the image method. Since the potential of a point charge goes as the inverse of the distance from charge to observation point, the series in this case is[62] (in cylindrical coordinates):

$$\phi(\rho, z) = Q \sum_{n=-\infty}^{\infty} (-1)^n / [\rho^2 + (z - nD)^2]^{1/2}, \tag{1}$$

where ρ and z are the cylindrical coordinates, Q is the magnitude of the charge, and D is the separation of the plates (the charge is assumed to be equidistant from both plates). Pumplin used a Sommerfeld-Watson transformation to approximate the summation of this series; Glasser pointed out that with the use of some rather elegant mathematical tricks, an exact solution could be had.

Very little was done with the problem for several years after this. Ianovici and Morf[63] used the image method to solve for the potential of a point charge in the presence of three dielectric layers (whereas Hague[64] had used it for permeable and susceptible media), and Silvester[65] used it to calculate the waveguiding properties of microstrip transmission lines. Stehle[66] actually laid out the image series for a dipole radiator in a cavity, but he obtained some dubious results in the summation of the plane wave series.

The advent of microwave electronics, particularly in semiconductor materials and especially in microwave monolithic integrated circuits (MMIC), led to a renewed interest in the subject of localized sources in layered media. The image method in dielectrics requires more images and more work than in conductors, and working in the microwave regime rules out the approximation that the detector is infinitely far away in many cases.

Lindell and Alanen[67] solved the problem in a half-space using dielectrics for various dipole orientations. Fang et al[68, 69] solved the problem of a dipole embedded in dielectric media for various polarizations using spectral Green's functions (the Fourier transform of the Green's functions for the spatial-domain image series, given by the Sommerfeld identity) and then Fourier-transforming the results. In order to obtain solutions, the problem was broken into three contributions: (a) quasi-static (the low-frequency approximation or the leading

terms in a Taylor expansion, dominant as the radial wavenumber becomes very large); (b) surface waves (dominant in the far-field); and (c) complex images (which they relate to "leaky waves" or the intermediate field). Kipp and Chan[70] then pointed out that these three divisions imply that not all of the poles have been removed from the contour around which the remaining contributions must be integrated.

A very good overview of the general approach to using Green's functions and images to solve a variety of physical problems is given by Barton[71]. His formalism was used by Dowling, Scully, and DeMartini[72] to derive an expression for a radiating dipole in a Fabry-Perot etalon, with an implicit assumption that makes the image problem a great deal easier: if the distance from the source to the observer is sufficiently large that the inverse distances in the field expressions for the images can be neglected, the summation reduces to a simple geometric series. Later Dowling and Bowden[73] applied this to derive a very simple approximate expression valid in the far-field of a dipole radiating at optical frequencies in a photonic band structure.

Milonni and Knight[74] were the only ones to suggest that a symmetry, like the one described here (Ch. 1 and App. D), might exist. Specifically, they stated that a photon reaching the detector after reflection would carry no information as to whether it came from the real dipole or one of its fictitious images. There has been until now no experimental test of this assertion, or of the symmetry of actually exchanging the dipole with one of its fictitious images, as is done in this work.

2.4 Cavity Electrodynamics

The earliest inclination that the states of an atom might be influenced by their surrounding environment came when Lamb and Retherford[75] established in 1947 that the fine structure of the hydrogen atom did not agree with the predictions of Dirac's relativistic quantum mechanics, and Bethe[76] later wrote down Schwinger and Weisskopf's idea that the atom could interact with its own radiation field. The energy level of the atom itself had actually shifted due to this interaction.

The principle behind the Lamb shift may have been realized nearly simultaneously by Purcell[77], who published a suggestion that a cavity could alter the spontaneous emission rate of an atom. He produced without derivation the formula

$$\Gamma_{cav} = \frac{3Q\lambda_0^3}{4\pi^2 V}\Gamma_{free}, \tag{2}$$

where Γ_{cav} and Γ_{free} are the cavity-modified and free-space emission rates, Q is the Q-factor of the cavity, V_e its effective mode volume, and λ_0 is the wavelength of the atomic transition. This implies that the emission rate of an atom in a cavity should go up and down in proportion to Q and to the ratio of "transition volume" to mode volume (λ_0^3/V).

The first direct observation of something similar to Purcell's idea had to wait until 1974, when Drexhage observed a change in the fluorescence decay time for monomolecular layers of dye proximate to a gold mirror[78]. Nearly 10 years later, Goy et al[79] observed differences

in the ionization states of atoms leaving a cavity that had been tuned to different resonant wavelengths, and Hulet et al.[80] measured changes in the time of flight of atoms passing through a parallel-plate cavity. Yet neither of these measured the spontaneous emission in order to correlate changes in it with their other findings. In 1987, Heinzen et al.[81] performed a comprehensive series of tests where the fluorescence of barium atoms in a confocal resonator was measured as a function of mirror separation, both in a direction along the cavity axis and perpendicular to it. All of these save for Drexhage referred to their work using the terms "enhanced" or "inhibited" spontaneous emission.

The consensus amongst these reports on enhanced/inhibited spontaneous emission seems to be that these phenomena are related to the coupling of atom to cavity, or to the radiative feedback between cavity and atom, and that the principal manifestation of enhancement or inhibition is an increase or decrease in the atom's decay rate. Yet even Ref. [81], the only experimental observation of cavity-induced level shifts to date, did not measure the decay rate directly, but relied on intensity measurements. Though measurements of fluorescence decay in cavities have been made (see Sec. 2.5.1), there is still some debate as to the distinction being made, as evidenced in Refs. [81, 6, 82]. Even few of these (save for [81]) make clear distinctions between coupled effects (due to feedback) and photon-only processes (due to interference).

The theoretical debate goes beyond simple measurements, naturally. At the heart of the modified spontaneous emission phenomenon is the question of how spontaneous emission actually occurs. In the semi-classical theory, the time-evolution of the two-level system is a direct result of the time-dependent Schrödinger equation; as Einstein said, it is also necessary for the atom to maintain thermal equilibrium with its surroundings[83]. The actual mechanism for the instability of excited states and the stability of the ground state, however, is not clear in the "neoclassical" picture.

The standard quantum-mechanical view is that the change in state of an excited atom is driven by "vacuum fluctuations," the extra $\frac{1}{2}\hbar\omega$ resulting from the anticommutation of creation and annihilation operators (quantum mechanical analogs of the Fourier components of the classical field) in the quantized field. This topic is covered in great detail in the books by Sakurai[84, pp. 29 ff.], Loudon[85, pp. 134 ff.] and by Sargent, Scully and Lamb[86, pp. 222 ff.]. In this theory, the presence of a cavity perturbs the vacuum fluctuations themselves and hence can change the spontaneous emission of an atom within the cavity. While the expectation value of the energy in vacuum fluctuations is $\frac{1}{2}\hbar\omega$ for every mode in the field, in the quantum theory, the atom, with its accelerated electron, loses energy to radiation, which it then promptly makes up through the contributions of vacuum fluctuations. This view is deemed essential to many to explain the stability of the ground state of atoms[87, p. 321].

Another approach, formulated largely by Barut[88, 89, 90], assumes that no source-free electromagnetic field is physically possible and uses the self-field of the electron to account for spontaneous emission. This formulation can account for such phenomena as the Lamb shift and cavity-induced modifications[91]. In this theory, the electromagnetic field is not quantized and thus vacuum fluctuations cannot exist. Though Crisp[92] has pointed out that the self-field theory has some problems with complex eigenvalues for observable operators

like energy, this is also the case for the perturbed Hamiltonian for a decay-broadened atom reacting to its own radiation[93, 84].

Other than these discrepancies and the explanation of the stability of the ground state, the fundamental difference between the two theories from the perspective of cavity electrodynamics is causality. Vacuum fluctuations and virtual photons represent a noncausal mechanism which can neither be decoupled from the emission process nor verified experimentally in standard microcavity experiments. Even the quantum-mechanical picture of feedback, an atom reacting to its own radiation, or even atoms in an ensemble reacting to their own radiation, contains an element of causality which does not require fictional particles or an æther-like entity in which they may travel. Since this picture is not necessary to explain microcavity effects on emission spectra, I will bypass this debate in favor of the simple feedback picture.

2.5 Vertical-Cavity Semiconductor Lasers

Though most of the development of VCSEL technology has occurred since about 1986 (in the United States; 1979 in Japan), the idea for a vertical-cavity diode laser was proposed by Pankove[94] in 1963 and demonstrated using an n^+pp^+ InSb injection diode by Melngailis[95] in 1965. After this, work virtually ceased in the area of vertical-cavity (but not in grating-coupled[96] or mirror-coupled[97]) devices until the 1980s.

In 1979, Soda et al.[98] reported a vertical-cavity design very similar to Mengailis' (using InGaAsP and InP with gold mirrors), and later improved on this basic design[99, 100]. This achievement was replicated by Passner et al.[101] in 1980. Growth of multilayer mirrors (distributed Bragg reflectors or DBRs) was demonstrated by Ogura et al. in 1983[102]. Four years later, the first DBR VCSEL was made by Kojima et al.[103]. The obvious advantages of higher-reflectance mirrors, lower cavity losses, lower threshold, higher quantum efficiency, higher modulation speeds, and single-mode operation quickly brought these devices into the limelight. By 1991, workers at AT&T were able to summarize[104] the technological aspects of VCSEL production.

A number of material systems have been used to make VCSELs, but most of the work has been done in III-V compound semiconductors, particularly in the $Al_xGa_{1-x}As$, $In_xGa_{1-x}As$, and $In_xGa_{1-x}As_yP_{1-y}$ systems. Studies have been made in these systems to optimize the doping of the mirrors and reduce the series resistance[105, 106, 107], to improve the temperature stability of VCSEL devices[108] (often by offsetting the QW emission and the cavity resonance[109, 110]), and to improve electrical and optical confinement by means such as ion implantation[111] and ion-beam etching[112] to define the active volume.

Recently, techniques such as mirror oxidation[8] have been used to improve the mirror reflectance, and hence to lower the cavity losses. Huffaker and Deppe[113] have reported that this process also increases the mode confinement and increases the spontaneous coupling into the lasing mode, resulting in a threshold reduction.

Threshold properties of VCSELs are indeed of great concern: since the current density increases dramatically[104] with the thickness of the intrinsic layer (in a *pin* structure), thus

limiting the amount of gain material, higher lasing efficiency is essential. Lower thresholds also improve the small-signal and high-speed response of the devices[114, 115], can lead to higher maximum output power[116], and can improve the device lifetime[117]. It is understandable in this context that one of the developments that has sparked quite a bit of interest has been the connection of enhanced spontaneous emission and thresholdless lasing.

2.5.1 Cavity Electrodynamics in VCSELs

The first report of thresholdless lasing may have come in 1982[118], but one of the first experiments to be published in English was performed by DeMartini et al.[119] in 1988. Both of these were performed using metallic cavities and Langmuir-Blodgett (LB) films. The DeMartini paper does indeed show differences for the measured laser output versus pump intensity for two different cavity lengths, but it is unclear whether several other factors (such as film thickness and pump field) were also kept constant while the cavity length was changed. Yokoyama et al[120] repeated a similar experiment using semiconductor distributed-Bragg-reflector (DBR) mirrors and an LB film.

QW laser thresholds can be made extremely low, in contrast to conventional *pn*-junction diode lasers[121]; VCSEL threshold current densities are now well below the 1 kA/cm^2 level[122, 123]. Some workers[124] have attributed threshold current reduction to increased spontaneous coupling efficiency (due to cavity-QED modifications), but there has been no report of a thresholdless VCSEL nor has anyone demonstrated that low thresholds are not simply intrinsic to QW VCSELs made from high-quality materials.

Much of the work on cavity-QED in VCSELs has been done by Yamamoto et al[125]. They have reported[126] a coherent pumping experiment wherein the input/output characteristic of a VCSEL device showed a spontaneous coupling factor β approaching unity, but have not clarified what part of this is due to enhanced emission and what to the normally low thresholds of VCSEL devices.

This paper was also among those who have reported Rabi oscillations or mode-splitting in semiconductor microcavities. From photoluminescence excitation (PLE) measurements at 4 K, they conclude that the exciton-polariton normal modes have been split by a VCSEL cavity, but do not mention how the PLE data were obtained (surface-normal probes have problems with reflectance and with field distributions, as discussed in Ch. 4 and App. B). Among the others reporting mode-splitting was the work by Houdré et al.[127], which measured bimodal distributions in the absorption spectra of semiconductor microcavities. This report recognized the work of Zhu et al.[128], which argued that vacuum Rabi splitting can also be described using linear dispersion theory, a product of resonant absorption (and hence resonant index of refraction).

All of these factors are compounded by localized gain media, such as quantum wells, where the entirety of the gain medium can be placed at a plane in the cavity mode field profile. Huang et al.[129] and later Lei et al.[130] measured intensity patterns from QWs at different positions in a microcavity and concluded that the spectral interference effects they saw were due to interference between simultaneous wavepackets emanating from the same emission event. The cavity could in this case "control" the spontaneous emission from the

QWs, but, again, single-photon events were not measured, and only spectral patterns in a single direction were taken into account.

At the very least, the connection between emitter coupling (feedback) and device performance is unclear: are lower thresholds the result of emission enhancement or simply lower cavity losses? Does nearly perfect spontaneous coupling into the lasing mode truly result from atom-cavity coupling or from extremely high quantum efficiency in the devices (as has been achieved in noncavity devices[131])? If successful in making a thresholdless device, how would one ascertain what mechanism to which to ascribe the success and perhaps harness it again in the future? At the heart of this lies the fundamental ability to discern feedback effects from all other phenomena in VCSELs, which, as stated in the introduction, is covered in this thesis.

3 Theoretical Background

3.1 Coupling Problems in VCSELs

This work aims to distinguish between two different types of coupling in VCSEL devices. The first of these is the coupling of light to the electromagnetic modes of cavity (mode coupling), and the second is the coupling of light back into the "atomic" (excitonic) system (emitter coupling). While the solution to the first involves finding only the electric field as a function of wavelength and observation point, the theory behind emitter coupling phenomena depends on the phenomenon to be examined.

Later in this work (Ch. 5), I will present evidence which shows a splitting in the peak of the emission spectrum from a quantum well in a VCSEL cavity. As this splitting will be attributed to emitter coupling in the form of mode splitting due to Rabi oscillation, an overview of that part of the theory is given herein.

3.2 Mode (Rabi) Splitting

The theory of strong-signal transition probabilities for a driven two-level system was originally worked out for magnetic resonance experiments by Rabi[132]; hence the theory bears his name. An excellent discussion of this theory is given by Sargent, Scully, and Lamb[86]. The subject has also been treated by Jaynes and Cummings[133], Agarwal[134], and Weisbuch et al.[135]. The treatment here summarizes much of what is in those works.

One very succinct way of viewing this phenomenon is to consider the coupling of various sets of discrete harmonic oscillators, as illustrated in Fig. 7. There are three regimes which segregate different types of behavior, from the strong coupling of two discrete oscillators to the weak continuum behavior. The first case corresponds to the venerable analogy to coupled pendula, wherein the two oscillators exchange energy back and forth indefinitely and can oscillate in harmony in different modes than they would individually. As Rabi showed, in this instance the transition probability (or probability of occupancy of the ground state B)

without outside help. Furthermore, the coupling constant $\mathcal{V}_0$ depends on the strength of the electromagnetic field in the cavity. If there is no cavity field (i.e., no photons), $\mathcal{V}_0 = 0$ and the effect disappears.

Finally, it is worth emphasizing again (in light of the forthcoming experiments) that this interaction fundamentally changes the energy levels of the emitter system and thus the radiation that emanates from it in all directions should reflect this fact. In addition, these changes to the energy levels can happen *only* if the potential $\mathcal{H}_{int}$ can cause transitions between the two states: if the absorption spectrum of the emitter and the cavity mode do not overlap in frequency space, there is no resonant interaction.

3.2.2 Classical (Linear Dispersion) Theory

This phenomenon, too, is not limited to a quantum-mechanical description. As Zhu et al.[128] have shown, the (resonant) absorption of the oscillators themselves, when transformed by the Kramers-Kronig integrals, leads to changes in the index of refraction which can cause the round-trip phase condition (which determines the modes) to be satisfied more than once. This can be thought of as a change in boundary conditions, either "lengthening" or "shortening" the cavity to achieve the same phase match. For strongly absorbing atomic systems (many atoms in the cavity), two new maxima appear when the *magnitude* of the detuning (between cavity mode and atomic resonance) frequency difference matches the absorptive phase change. The fundamental resonance also disappears because of the enhanced absorption effect.

The biggest difference between the quantum and classical treatments is that classically the cavity line is split by a frequency difference

$$\Omega_c = \left[\frac{\alpha_0 L\sqrt{R}}{2(1-R)}\Gamma_0\Gamma_c - \frac{(\Gamma_0 - \Gamma_c)^2}{16}\right]^{1/2} \tag{10}$$

(Γ_0 = atomic decay rate, $\Gamma_c = \delta\omega_c/2$ = cavity "decay rate," R = reflectivity, $\alpha_0 L$ = absorption), whereas the quantum-mechanical case does not explicitly involve decay rates (broadening) or absorption or reflectivity. However, as noted above, the quantum derivation is predicated on the assumption that the applied field ($\mathcal{V}_0$) can connect the two states. If the transition truly has no broadening factors (which is unphysical), then the interaction part of the Hamiltonian must be multiplied by the delta function $\delta(\omega_0 - \omega)$. Rabi oscillations then occur only when $\omega = \omega_0$ and the emission line does not split.

The question most relevant to this work is: do the actual energy levels of the atom shift (that is, is this feedback)? One could argue, in analogy to the pendula, that ω_0 is simply the equivalent of the mass of the pendulum, which need not change in order for the normal modes to change. On the other hand, the classical, resonant-absorption picture suggests that only the full system changes. If the mode splitting is simply a matter of satisfying different phase conditions, then the whole phenomenon might be seen as simply an interference effect.

Whatever the case may be, this difference is testable. If the energy levels do indeed change, the split should be observable in the side emission spectrum of an emitter in a

cavity. If mode splitting is observed in end emission, and not in side emission, then it is safe to conclude that the actual energy levels of the emitter have not changed. However, as pointed out in a later chapter (Ch. 5), there are distinctions to be made in the types of side emission one might observe.

3.3 Radiation Intensity Patterns and Localization Effects

The normal Fabry-Perot interferometer passes a given frequency along its cavity axis and then rejects this in favor of bluer frequencies along axes nonparallel to the surface normal. At a single frequency, the spatial distribution of intensity has a strong peak along an axis at some angle to the cavity axis, a marked difference from an arbitrary free-space pattern. This device filters (redistributes) certain frequencies of light without regard to the source that has emitted them; such redistribution should therefore not be construed as an indicator of feedback without correlation from another type of observation.

In a like manner, the Fabry-Perot etalon will also redistribute radiant energy from a localized source placed between its two reflectors. However, in this case, the redistribution effect can be much stronger than the normal interferometer case. As will be shown below, the ratio of transmitted intensity to free-space intensity for the emitter inside the etalon can greatly exceed unity (in a given direction), which is not possible for the normal interferometer. The foundation for interpreting the results of this work (in Ch. 5 and 6) is the basic picture of a dipole between two mirrors.

As referenced in Ch. 2, the full solution to the mode field of a dipole in a cavity can become highly entangled, if certain assumptions are not made. The complete field for an oscillating electric dipole is[136, p. 395]:

$$E(k,r) = k^2(\mathbf{n}\times\mathbf{p})\times\mathbf{n}\frac{e^{\imath kr}}{r} + [3\mathbf{n}(\mathbf{n}\cdot\mathbf{p}) - \mathbf{p}](\frac{1}{r^3} - \frac{\imath k}{r^2})e^{\imath kr}, \tag{11}$$

where $\mathbf{n}$ is a unit normal radius vector and $\mathbf{p}$ is the dipole moment vector. Since the Fresnel coefficients at a given boundary do not change with the form of the incident field, it is possible to solve Eq. 11 exactly to yield the allowed wavenumber k values, which in most cases will contain a very small contribution from the near field terms. As will be shown below, this form of the solution is not practical for calculations, and even other solutions which take into account the $1/r$ dependence are a great deal less tractable and yield only scantly better results for our purposes here than those which do not.

3.3.1 Fresnel Analysis

Figure 8 shows a schematic of a dipole situated between two mirrors, a distance a away from mirror 2 and $l_c - a$ from mirror 1. The observation point is at a distance ρ from the specimen, at an angle θ with respect to the cavity ($\hat{z}$) axis. The mirrors and the plane of dipole are assumed to be infinite in extent, so the emitted ray drawn in Fig. 8 will be repeated an infinite number of times along the line of the mirrors.

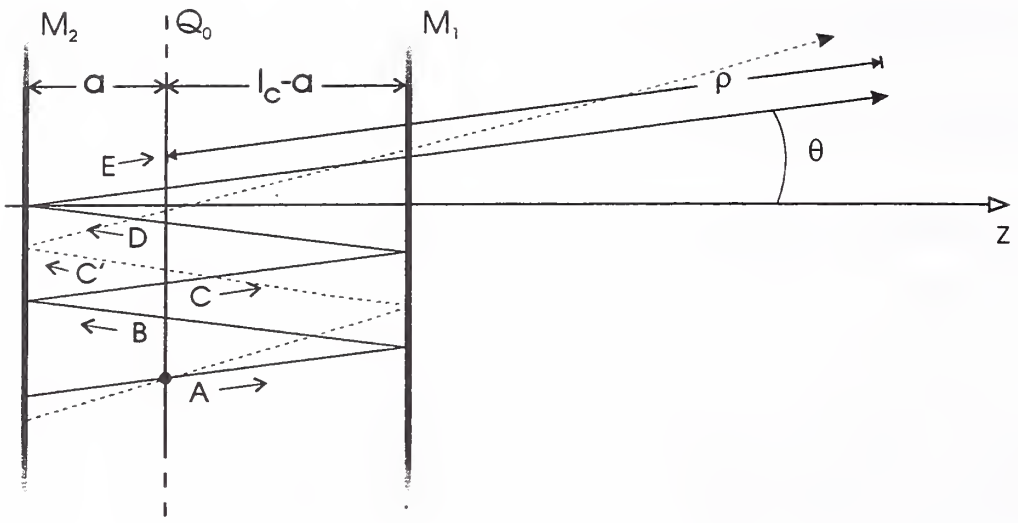

Figure 8: Diagram showing emission from inside a Fabry-Perot cavity. The mirrors (M_1 and M_2) and the source plane (Q_0) are assumed to be infinite in the directions perpendicular to the z-axis.

To digress just slightly, the rays considered in the analysis can be considered as originating at a single dipole, as shown in Fig. 8. In this case, the summation of all the rays represents an average of all the waves (or photons) from the single source. This is entirely equivalent to considering only a single ray (at a fixed position and angle) and decomposing it into an infinite set of rays which originate at fixed points along the line Q_0. Thus, as long as the incoherence between dipoles in the line Q_0 may be neglected, the emission may be viewed as a statistical average for a single dipole or as an ensemble average of a collection of dipoles.

Consider only the rays that enter the detector at an angle θ; then only the emission corresponding to rays A, B, C, D, E, etc. will be counted in the total. Emission along the ray C′, for example, will not get to the point of observation in this single-ray approximation. (This is tantamount to a detector with a numerical aperture of zero.) In this analysis, it is assumed that the source emits plane waves, but this need not be the case, as discussed in Sec. 3.3.2.

Using the Fresnel coefficients r_1 and r_2 for the reflectivities of the two mirrors and t_1 and t_2 for the transmissivities of the mirrors, the sum of all the waves (rays), arriving at the observation point at ρ, emitted initially toward mirror 1 (A, C and E in the drawing), is the geometric series (omitting the time dependence)

$$\frac{E_{k,1}(r)}{E_0} \approx \frac{e^{\imath k\rho}}{\rho}\left[t_1 + r_1 r_2 t_1 e^{\imath k 2\delta_C} + r_1^2 r_2^2 t_1 e^{\imath k 4\delta_C} + \cdots\right], \tag{12}$$

where the abbreviation $\delta_C = l_c \cos\theta$ has been used. The geometric construction in Fig. 9 shows the calculation of path differences.

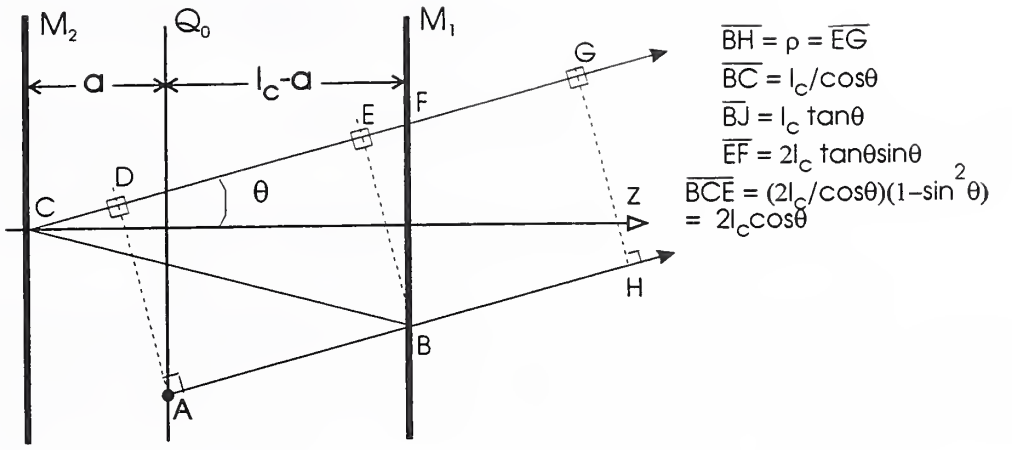

Figure 9: Geometric construction of rays for a dipole emitting inside a Fabry-Perot cavity. The path length computation is shown beside the figure.

Similarly, the sum of all rays emitted initially toward mirror 2 (B and D in the drawing) is

$$\frac{E_{k,2}(\rho)}{E_0} = \frac{e^{\imath k\rho}}{\rho}\left[r_2 t_1 e^{\imath[k2\delta_2+\pi]} + r_1 r_2^2 t_1 e^{\imath[k(2\delta_2+2\delta_C)+\pi]} + r_1^2 r_2^3 t_1 e^{\imath[k(2\delta_2+4\delta_C)+\pi]} + \cdots\right], \qquad (13)$$

with $\delta_2 = a\cos\theta$. Here, the factors of π in the exponentials account for the phase changes on reflection from the mirrors (with the waves emitted toward mirror 2 undergoing an odd number of reflections and the waves emitted toward 1 an even number). This phase difference can also be accounted for by changing the sign of the Fresnel coefficients for opposing incidence directions. (The phase change does not always have to be exactly π: if the boundary has some non-negligible inductance, an additional, material-dependent, phase change must be included. For simplicity, it is assumed here that the materials are noninductive.)

The Airy formula[137] for the infinite geometric series then allows Eqs. 12 and 13 to be summed (since r_1, r_2, and $e^{\imath k\{\}}$ are all less than unity)[1] and the result is

$$\begin{aligned}\frac{E_k(r)}{E_0} &= \frac{e^{\imath kr_0}}{r_0}\left\{t_1 \sum_{m=0}^{\infty} r_1^m r_2^m e^{\imath 2mk\delta_C} + r_2 t_1 e^{\imath[k2\delta_2+\pi]} \sum_{m=0}^{\infty} r_1^m r_2^m e^{\imath 2mk\delta_C}\right\} \\ &= \frac{e^{\imath kr_0}}{r_0} t_1 \left(\frac{1 + r_2 e^{\imath(k2\delta_2+\pi)}}{1 - r_1 r_2 e^{\imath 2k\delta_C}}\right). \qquad (14)\end{aligned}$$

[1]For modest reflectances, $r \approx 0.6$, this converges very quickly, so the infinite approximation is good. In other cases, one can truncate the series at the ring-down time as in [72].

The intensity is the square magnitude of this field and is proportional to the power received by the detector. Multiplying Eq. 14 by its complex conjugate gives

$$\mathcal{T}_I = \frac{I_k(r)}{I_0} = \frac{T_1}{\rho^2}\left(\frac{1+R_2+2\sqrt{R_2}\cos(2k\delta_2)}{1+R_1R_2-2\sqrt{R_1R_2}\cos(2k\delta_C)}\right), \tag{15}$$

where the intensity coefficients $T_1 = |t_1|^2$, $R_1 = |r_1|^2$, and $R_2 = |r_2|^2$ have been used. This equation differs from the normal Fabry-Perot interferometer transmission function

$$\mathcal{T}_O = \frac{I_k}{I_0} = \frac{T_1T_2}{1+R_1R_2-2\sqrt{R_1R_2}\cos(2k\delta_C)}, \tag{16}$$

only in its numerator, yet this makes a large difference in the behavior of $\mathcal{T}_I$. The internal-dipole form contains a term which accounts for the relative position of the dipole, and the limiting values of both equations can be shown to be 1 (Eq. 16) and ∞ (Eq. 15). The somewhat remarkable implications of this result will be discussed below (Sec. 3.5).

3.3.2 Near-Field Limitations

To illustrate the difficulty in obtaining a solution from the full form of Eq. 11, it suffices to begin with the standard far-field form (rather than the full form of Eq. 11):

$$E_k(\rho,t) = E_0\frac{e^{\imath(k\rho-\omega t)}}{\rho} \tag{17}$$

(which assumes the dipoles are polarized along the $\hat{y}$ axis; a $\sin\theta$ term must be included for dipoles along the $\hat{x}$ axis). The distance ρ represents the distance from source to observation point by whatever path the field takes (that is, including bounces). The sum of wavefronts corresponding to Eq. 12 is then

$$\frac{E_{k,1}(\rho)}{E_0} = t_1\frac{e^{\imath k\rho}}{\rho} + r_1r_2t_1\frac{e^{\imath k(\rho+2\delta_C)}}{\rho+2\delta_C} + r_1^2r_2^2t_1\frac{e^{\imath k(\rho+4\delta_C)}}{\rho+4\delta_C} + r_1^3r_2^3t_1\frac{e^{\imath k(\rho+6\delta_C)}}{\rho+6\delta_C} + \cdots \tag{18}$$

The above equation is of the form

$$\sum_{m=0}^{\infty}\frac{K^m}{\rho+m\alpha},$$

which may or may not converge depending on the values of ρ and α. An analytical form of the field for a dipole inside a cavity is thus quite difficult to obtain.

However, it is true that the emission pattern can be accurately described (see App. B) by combinations of Airy functions, which correspond to plane waves, as in the case of transmission through a Fabry-Perot etalon, for example. This implies that the above treatment, using plane waves, is a good approximation. A justification for this is as follows: if $\rho \gg m\alpha$ up to some integer M in the series where $r_1^Mr_2^M$ becomes negligibly small, then the higher

terms where ρ and $m\alpha$ are comparable have vanishingly small numerators. The essential theme here is that the power function r^m decays faster than the linear function $m\alpha$ increases. If this is the case, all the terms in the series beyond the M^{th} term may be approximated as zero and the approximate form becomes

$$\sum_{m=0}^{\infty} \frac{K^m}{\rho + m\alpha} \approx \sum_{m=0}^{\infty} \frac{K^m}{\rho},$$

and the inverse distance dependence may be negelected in the summation. For optical frequencies, even where microcavities are concerned, it is easy to make good on the approximation that $1/(r-a) \approx 1/r$. For other cases, one can note that the Fourier transform of e^{ikr}/r is a constant and use the spectral Green's function method to sum the series, as is done by Fang, Yang and Delisle[68].

As an example, let us consider the error introduced by this approximation at the m^{th} term of the series. This is

$$\delta = \frac{\frac{r^{2m}}{\rho} - \frac{r^{2m}}{\rho+m\alpha}}{\frac{r^{2m}}{\rho}} = \frac{m\alpha}{\rho + m\alpha} = \frac{1}{1 + \frac{\rho}{m\alpha}}. \tag{19}$$

So if the desired accuracy is 0.1% and the reflectivity is $R = 0.99$, then the power series must decay to $r^{2m} = R^m \approx 0.001$, in which case $m \approx 680$. We can safely truncate the series at this point if δ introduces no further error, or $\delta \leq 0.001$. We thus have the constraint that $\rho/m\alpha \geq 999$ or $\rho/\alpha = \rho/l_c \cos\theta \geq 680000$. For microcavities, this is not difficult at all. For lower reflectivities, the constraint is much more lenient: at $R = 0.8$, the ratio of observation distance to cavity length need only be greater than 30 000 for 0.1% accuracy.

The general result is that in order to observe near field effects in emission from dipoles inside a Fabry-Perot etalon, the point of observation must be quite close to the near field.

3.4 Miscellaneous Relevant Cavity Quantities

A number of the calculations in this work will depend on various parameters, such as Q factor and finesse, that are relevant to laser cavities. In order to facilitate a standard of reference for these quantities, a brief discussion follows. The elements of this compendium may be found individually in Verdeyen[138], Yariv[139, 140], Fowles[141], and Born and Wolf[142].

The Q factor of a Fabry-Perot cavity, like the Q of any resonance phenomenon, may be defined as the ratio of the center frequency to the halfwidth of the resonance peak,

$$Q = \frac{\omega_0}{\Delta\omega_{1/2}}, \tag{20}$$

and it may be found from computing the ratio of the energy stored in the resonator to the power dissipated by it. (Often the definition and the computation are reversed.) Another way to find Q is to maximize the function given in Eq. 16 and then find its half-maximum

points:

$$\begin{aligned}
\frac{I_k}{I_0}|_{max} &= \frac{T_1 T_2}{(1-\sqrt{R_1 R_2})^2}, \\
\frac{I_k}{I_0}|_{1/2} &= \frac{T_1 T_2}{2(1-\sqrt{R_1 R_2})^2} \\
&= \frac{T_1 T_2}{(1+R_1 R_2 - \sqrt{R_1 R_2}\cos(2n\omega_{\pm 1/2}\delta_C/c)};
\end{aligned} \tag{21}$$

the solution is

$$Q = \frac{2\pi l_c}{\lambda_0}\frac{(R_1 R_2)^{1/4}}{1-\sqrt{R_1 R_2}}, \tag{22}$$

where $\lambda_0 = 2\pi c/\omega_0$. The photon lifetime, or decay time, in the cavity is

$$\tau_p = \frac{Q}{\omega_0}. \tag{23}$$

In traditional optical etalons, the ratio of cavity length to resonance wavelength is a very large number, so the need for another, more manipulable quantity, arose. This quantity, known as the finesse, is defined as the ratio of the free spectral range $\Delta\omega_{FSR}$ to the resonance halfwidth $\Delta\omega_{1/2}$,

$$\mathcal{F} = \frac{\Delta\omega_{FSR}}{\Delta\omega_{1/2}}. \tag{24}$$

The free spectral range is nothing but the spacing between the modes of the cavity — $\Delta\omega_{FSR} = c/2l_c$, so the finesse is thus

$$\mathcal{F} = \frac{\pi(R_1 R_2)^{1/4}}{1-\sqrt{R_1 R_2}}. \tag{25}$$

This is called in some books the *reflecting finesse*, and is distinguished from the function

$$F = \frac{4\sqrt{R_1 R_2}}{(1-\sqrt{R_1 R_2})^2}, \tag{26}$$

which is sometimes called the *coefficient of finesse*. "Finesse," as used in most texts, usually refers to the quantity defined by Eq. 25. The transmittance and reflectance functions are sometimes also denoted by script letters:

$$\mathcal{T} = \frac{I_k^t}{I_0} \tag{27}$$

$$\mathcal{R} = \frac{I_k^r}{I_0}. \tag{28}$$

The resolving power of an instrument can be defined in terms of the Taylor criterion, which states that two spectral lines are resolved if their curves cross at any point lower than

or equal to the half-maximum intensity point. (This leads to a fringe contrast close to 1.37:1 for a Lorentzian curve, 1.25:1 for a Gaussian.) For a Fabry-Perot etalon, this works out to a number proportional to the finesse:

$$RL = m\mathcal{F} = m\pi \left(\frac{(R_1 R_2)^4}{1 - \sqrt{R_1 R_2}} \right), \tag{29}$$

For a microscope objective, the resolving power is defined in a similar fashion, but in this case diffraction theory leads to an entirely different lineshape. For a uniform beam illuminating an objective, the pattern produced on a screen at the image point is a Bessel function, the zeroes of which determine the resolution limit and are given by

$$R_0^U = \frac{0.61\lambda}{\mathrm{NA}}, \tag{30}$$

where NA is the numerical aperture of the objective. For a Gaussian beam input into an objective, the pattern produced is Gaussian and the radius of the $1/e^2$ points is conventionally taken to determine the resolution. This leads to the formula

$$R_0^G = \frac{\lambda}{\pi \mathrm{NA}}. \tag{31}$$

The contrast in this case works out to about 3.77:1. Further, $R_0^G / R_0^U = 0.5$, so a Gaussian beam will give approximately twice the resolution as a uniform one.

Finally, the *round trip phase condition* inside a cavity is the requirement that the field of a wave return to its original phase after a transit of the cavity in order to create a resonance:

$$\frac{2n_R \omega l_c \cos\theta}{c} = 2m\pi. \tag{32}$$

3.5 Comments

3.5.1 Redistribution versus Enhancement

Heinzen and Feld[81] have asserted that changes in the emission intensity are "*not* a 'spatial redistribution' of the spontaneous-emission probability." They argue that decreases in the side emission intensity of a dipole in a cavity which follow increases in the surface emission happen "because of a decrease in the excited-state atomic population, caused by an increase in the total decay rate." Though they apply to a confocal rather than a plane-parallel resonator, these statements are included here because they illustrate a very important distinction to be made.

It is entirely reasonable to expect that if the decay rate of an atomic system increases, then more transitions will take place in a given time and more optical energy will be output in that time. Consider for a moment such a system of N_0 single-frequency, perfect, two-level atoms, being excited by some means (a laser, for example) that can be pulsed. The power (energy) available to the system from the excitation source is fixed. When the atoms are

in free space, let us say that a fraction $\eta = N/N_0$ of them absorb photons of frequency ω_0 from the pump and then decay, re-emitting N photons at ω_0. In the absence of all other considerations, if somehow the decay rate of the atoms could be changed, then those N photons would be emitted in a shorter time interval, leading to a higher measured intensity.

There is a paradox here: changing the decay rate, which can be achieved by purely passive means such as placing the atoms in a cavity, seems to cause more energy to come out of the dipole, in a seeming violation of the principle of conservation of energy. However, there is a safety mechanism. If the decay rate has gone up according to Eq. 5, then the energy level of the atom has also shifted. In the truly monochromatic approximation, the atoms, now resonant at $\omega_0 + \Delta\omega$, no longer absorb the pump light at ω_0. If the lines are broadened, then the cross section of the atoms has simply gone down; the N atoms that were excited at ω_0 will be $N - \Delta N$ at $\omega_0 + \Delta\omega$. If the pump is polychromatic, then the only difference is the frequency at which the N photons will be absorbed and then re-emitted. There is no way, even for passive feedback mechanisms (and ignoring other loss mechanisms and nonlinear effects), for N photons at ω_0 to become N photons at $\omega_0 + \Delta\omega$ simply through the decay of N atoms.

Yet if the energy is available from the pump, the intensity can increase when the lifetime decreases. If a few assumptions are made about the cavity lineshape and the radiative process, the decay rate then varies as the Q factor, as in Purcell's result[77]. However, since that result depends also on the ratio of λ_0^3 to the effective mode volume, in the ideal Fabry-Perot resonator (where the mode volume is indeterminate), this effect should not be observable for any value of Q. (In less perfect structures such as VCSELs, refractive index variations can be used to reduce the effective mode volume.)

On the other hand, the electrodynamic modes of the cavity can also redistribute the intensity spatially. This effect is different when the dipole is in the cavity (as opposed to being far from it, as illustrated by Eqs. 15 and 16) and can account for in-cavity to free-space intensity ratios along a given direction (the end, for example) greatly in excess of unity. Therefore, conservation of energy demands that the ratio along some other direction (such as the side) be decreased to compensate. Thus the question becomes one of how to separate intensity changes due to changes in the emitter's decay rate from those due to simple spatial redistribution of energy. Something more than angular intensity patterns of light emitted out of the surface of the etalon, for example, is needed.

3.5.2 Estimation of Magnitudes

In the discussion surrounding Eq. 15, I noted that the redistribution of light energy from a dipole inside an etalon could lead to enhancement of the intensity ratio I/I_0 beyond normal values. The following example serves testimony to this effect. Assuming that $R_A = R_B = 0.95$ and $\delta_2 = \delta_C/2 = m\pi/2$ (dipole at the center of the cavity, on resonance), the first order mode has a lower ratio than free space (as emitted by the isolated dipole),

$$\frac{I_{m=1}}{I_0} = (0.05)\left(\frac{1 + 0.95 - 2\sqrt{0.95}}{1 + 0.9025 - 2(0.95)}\right) \approx 0.02, \tag{33}$$

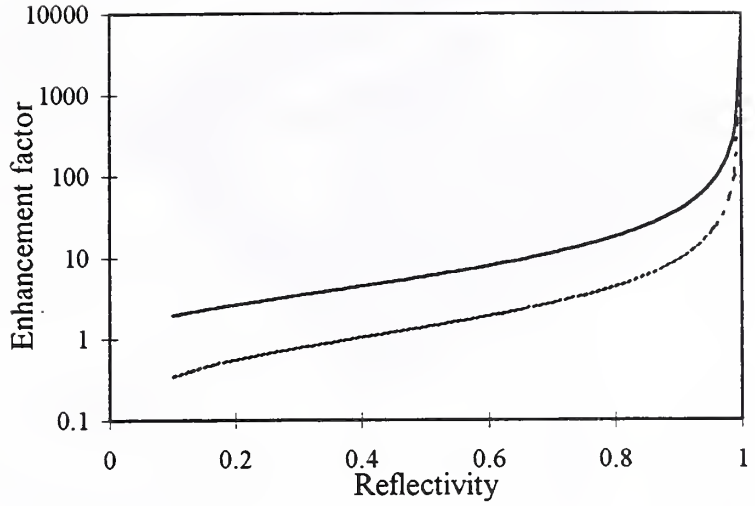

Figure 10: A comparison of the Γ factor and the peak intensity ratio (of free field to the cavity spectrum) for an ideal, lossless cavity with $\lambda_0^3/V_e = 1$ as a function of the mirror reflectance R. The dashed line is the intensity ratio.

whereas the second order mode has a much larger ratio:

$$\frac{I_{m=2}}{I_0} = (0.05)\left(\frac{1+0.95+2\sqrt{0.95}}{1+0.9025-2(0.95)}\right) \approx 78. \tag{34}$$

Thus, the question is again how significant is the magnitude of this effect when compared with the possible lifetime enhancement. Figure 10 compares the emitter Γ ratio (proportional to the cavity Q) of the ideal cavity (where λ_0^3 is equal to the effective mode volume V_e) with the peak value of the intensity function, given by Eq. 15. Apparently, the two are essentially the same order of magnitude across the range of mirror reflectivity. Since both effects depend on the position of the dipole, and since the intensity patterns emitted out the ends of the etalon will be the same for both, some other measure — such as changes in the decay rate or a shift in the emission energy — must be used to determine when feedback has actually occurred.

Finally, in a cavity structure like a VCSEL, the effects of refractive-index dispersion cannot be neglected. If all the frequencies of a given quantum-well spectrum are treated as independent transitions (which is a fair approximation at room temperature), then the lifetime of each can be changed independently. If the causality condition ($\lambda_0^3 < V$) is not met at some frequency, it may yet be satisfied at another frequency where the effective cavity length has shortened due to index dispersion.

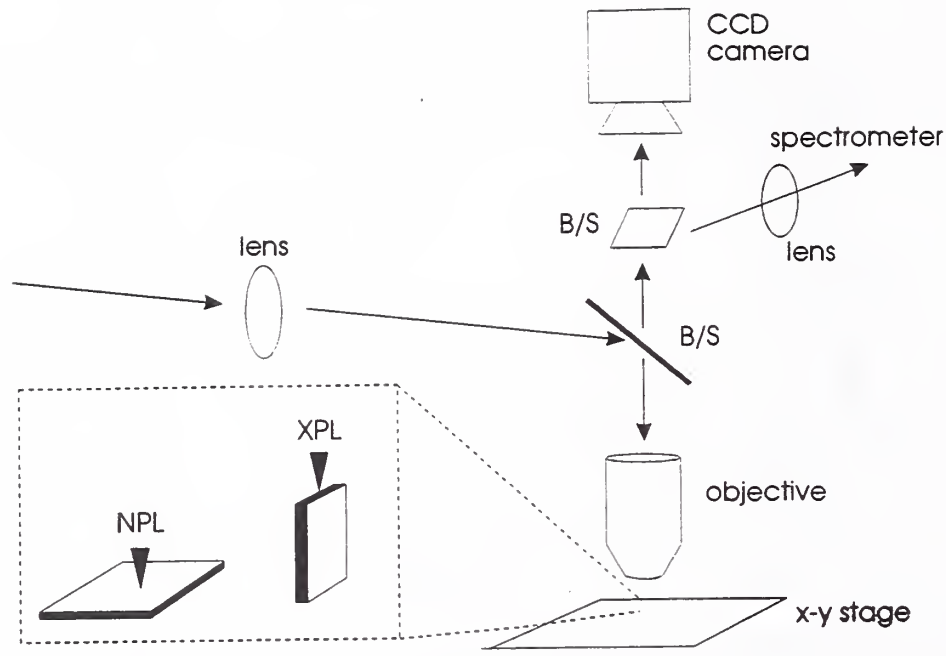

Figure 11: Schematic of the cross-sectional photoluminescence (XPL) system.

4 Cross-Sectional Photoluminescence

4.1 Surface-Normal and Cross-Sectional Emission from VCSELs

This experiment, a very simple technique which later found utility in a number of applications, was originally developed at NIST to yield information about the match between the wavelengths of quantum-well emission and cavity resonance in order to provide better metrology of VCSEL devices. This was then extended to include an attempt to create a model that would allow side-emission data to be extracted from surface-normal data solely with the aid of other nondestructive measurements. It also served as the genesis for later measurements on cavity effects in VCSELs as well as the primary evaluation tool for a novel study on alloy interdiffusion in quantum wells (documented in App. A). The resolution of the system was such that a profile of cross-sectional emission intensity versus depth into the epitaxial structure could also yield useful information about growth variations and localized QW emission.

4.2 Description of Tube-Length-Conjugate System

Figure 11 shows a diagram of the experimental apparatus first used to make XPL measurements. The system was a slightly modified version of a commercial microscopic-PL setup, designed for objectives corrected for a tube length of 160 mm. Since the flexibility of this system was somewhat lacking, another optical apparatus was constructed, as described below (Sec. 4.3). However, the performance of this setup was found to be quite adequate for many VCSEL measurements.

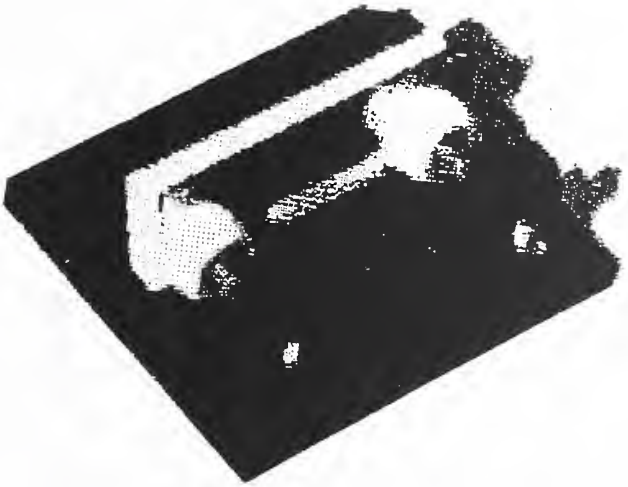

Figure 12: Photograph of the specimen mount used for XPL measurements.

To optimize the resolution of the system, the pump and collection axes were kept as close as possible to collinear and the orthogonality between the cleaved edge and the pump beam was conscientiously preserved. Small apertures were used to spatially filter the light before it entered the first (objective-filling) lens. The specimen platform was mounted on a motor-driven, x-y stage with a step size of 0.1 μm. The objective could be changed between a 40×/0.6 NA and a 10×/0.2 NA, both lacking near-infrared correction. These objectives were not coated to increase their transmissivity in the near-infrared, nor was their chromatic aberration minimized in this region. The second XPL setup described in Sec. 4.3 resolved these and other problems.

The spectrometer used had a (double-pass) path length of 0.85 m, an aperture of f/6.9, double, 1200 groove/mm, holographic gratings, and entrance, exit and intermediate slits adjustable from 0 to 3000 μm. Its (manufacturer-specified) dispersion at 514.5 nm was 0.4 nm/mm leading to a maximum wavelength resolution of 0.004 nm. (The actual measured dispersion at 546 nm was about 0.45 nm/mm.) In most of these experiments, the slit settings were left at 100 to 200 μm, giving a spectral resolution of approximately 0.05 to 0.1 nm.

Specimens were turned on edge and held securely (see Fig. 12) to obtain the cross-sectional spectra. Great care was taken in cleaving the specimens in order to present the most pristine edge possible; specimens were often recleaved to remove oxidation or scarring. Due to the cleavage preference in GaAs crystals, measurements were most often made along the facets of the (011) or (0-11) axes.

4.2.1 Resolution of the Probe

The minimum spot radius in the case of a Gaussian laser beam focused by an objective is given by Eq. 31, and should be about half the resolution limit for a uniform beam through the same objective, as given by Eq. 30. However, for cross sectional probes which are absorbed by the barriers (around the QW), carrier diffusion can make the effective resolution larger

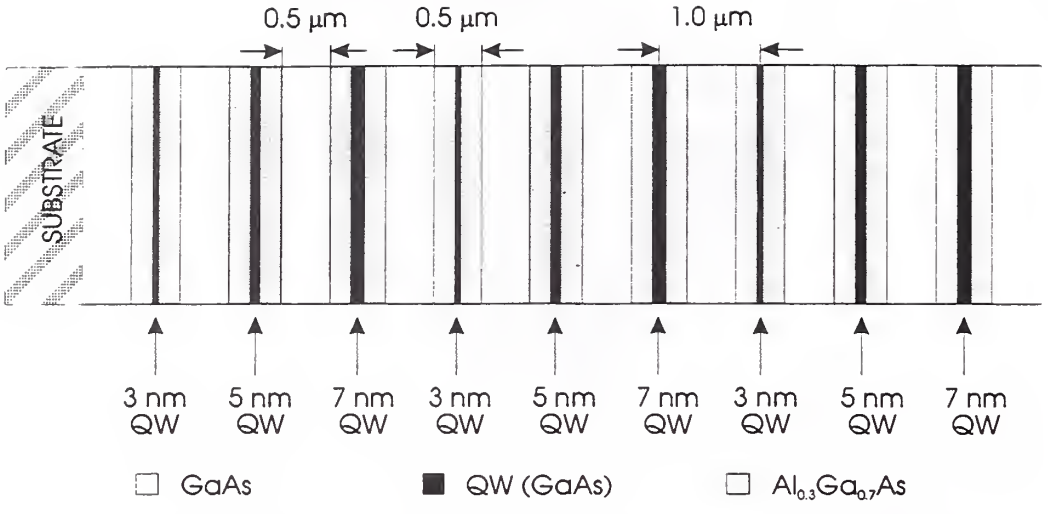

Figure 13: Schematic of nine-QW resolution test structure.

than the actual spot size. In order to gauge the magnitude of this effect, a simple test of the resolution appeared to be in order.

Figure 13 shows the design of a test structure used to measure the resolution of the side emission probe, consisting of nine quantum wells, spaced 1 μm apart. The design thicknesses of the wells were 3, 5, and 7 nm and they were arranged in three sets of three so as to present a pattern (working down from the surface) of 7/5/3, 7/5/3, 7/5/3.

The room-temperature surface-normal luminescence of this structure quite clearly does not tell the whole story. Figure 14 shows the surface-normal photoluminescence (NPL) of the structure, in which only one peak of the nine can be seen. On the other hand, cross-sectional photoluminescence (XPL) can resolve each of the wells individually, as shown in Fig. 15. The 7 nm QW emits at about 820 nm, the 5 nm at about 800, and the 3 nm at roughly 760. The bottom graph in Fig. 15 shows that the third 3 nm QW (QW9), which is closest to the substrate, is also a little thinner than its counterparts closer to the surface (emitting at about 730 nm). From a measurement standpoint, Figs. 14 and 15 illustrate the utility of the XPL measurement: what lies on top of a certain target area is irrelevant to probing it, nor is it necessary to cool the specimen to cryogenic temperatures to resolve relatively broad peaks that are closely spaced in wavelength but spatially separated.

Figure 16 shows a set of spatial scans (along an axis parallel to the growth direction) where the nine QWs have been resolved in spatial order. The first three curves represent three different emission wavelengths — 820, 800, and 760 nm — which were held constant during the scan, corresponding to the peak emission of each of the three wells. The fourth curve was taken at 730 nm to resolve the bottommost QW. The extra peaks in the curves at the locations of the other QWs (emitting at different wavelengths) are actually the emission tails of those wells. The average spacing as measured by the scanning apparatus was about

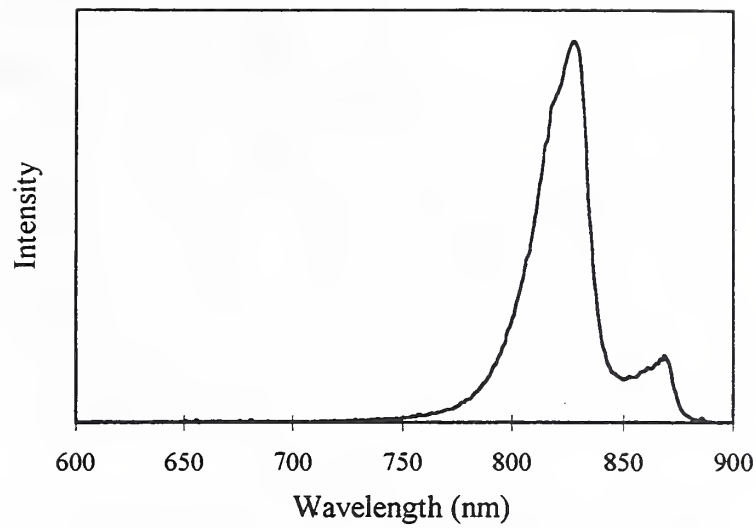

Figure 14: Surface-normal emission of nine-QW structure.

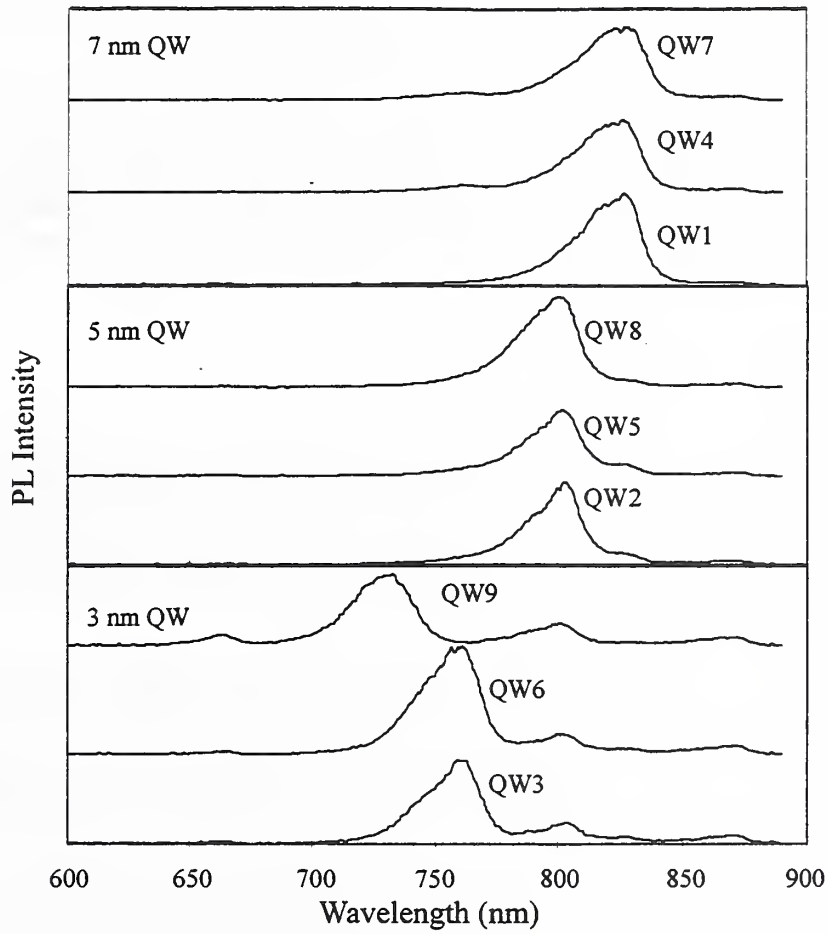

Figure 15: Side emission of nine-QW structure.

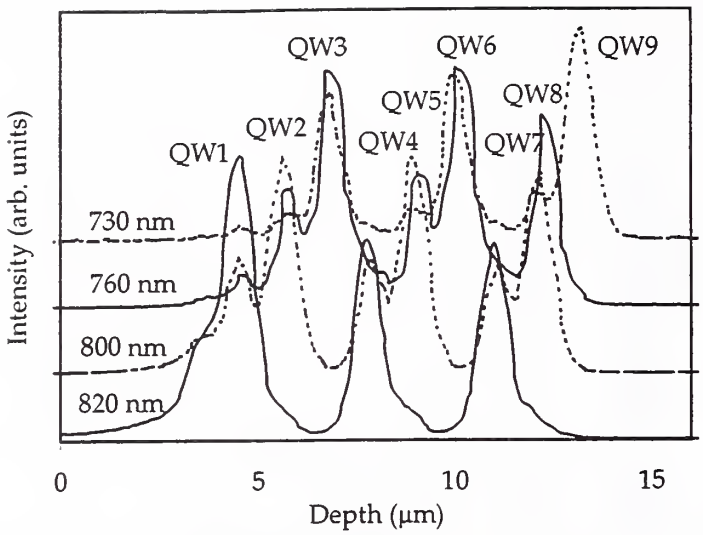

Figure 16: XPL Depth profile of 9-QW test structure.

1.4 μm, which compares favorably with the spacing of 1.2 μm measured by transmission electron microscopy (TEM). The reproducibility of this spacing, approximately ± 0.05 μm, was well within the uncertainty of the mechanical system, 0.1 μm.

In addition, the full width at half maximum of the peaks averaged slightly greater than 0.5 μm, which is very close to the diffraction-limited minimum spot size for uniform 488 nm excitation through the 40× objective. These data suggest that the diffusion effect, coupled with the distortion of the beam by the various optics used to steer it, makes the effective resolution closer to the uniform-beam case rather than the Gaussian. In subsequent calculations, therefore, it will be assumed that Eq. 30 is valid for the spot radius.

4.3 Description of Infinite-Conjugate System

In order to resolve some of the measurement uncertainties in the original apparatus, a new microscopic-luminescence system was constructed to allow greater control of the measurement parameters such as polarization and pump angle, to improve the system's response in the near-infrared, and to allow greater flexibility to perform a wider array of measurements (such as luminescence and reflectance) in the same spot on the specimen (and using the same optics). Some of these additions are documented below.

The schematic for this setup is given in Fig. 17. The stages on which the objective is mounted decouple the vertical ($\hat{y}$) scanning motion from changes in the optical imaging. Horizontal ($\hat{x}$) scanning is accomplished by moving the specimen stage. As changes in the focus cause changes in the conjugate path length, the system is limited to "infinite"-conjugate objectives.

Again, an iris was used to spatially filter the pump beam and attention was scrupulously paid to preserving orthogonality and collinearity. The objectives used were: 65×, 0.55 NA; 50×, 0.42 NA; 15×, 0.25 NA; 6×, 0.1 NA. In this case, however, the resolution is slightly different in that it depends on the actual size of the collimated beam rather than the filling

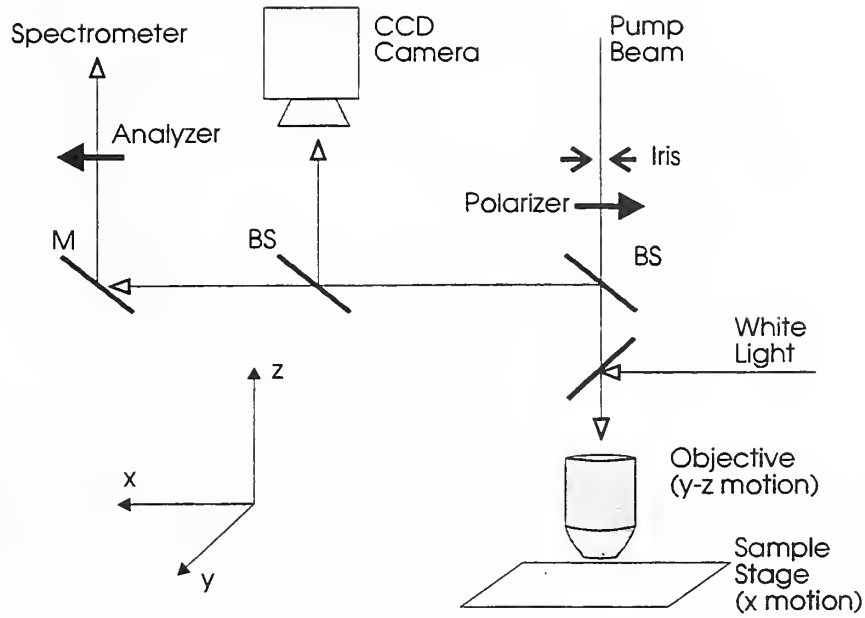

Figure 17: Schematic for the modified luminescence system.

of an objective. The (Gaussian) beam diameter was estimated at about 5 mm, while the smallest entrance pupil (on the 50× objective) measured about 3 mm. Since a smaller spot (into the same lens) will decrease the numerical aperture,

$$\begin{aligned} f/\# &= \frac{F}{D} = \frac{1}{2NA} \\ NA &= \frac{D}{2F}, \end{aligned} \tag{35}$$

(D = lens diameter, F = focal length), and as the resolution goes as the inverse of the numerical aperture, reducing the size of the input beam beyond the size of the exit pupil only decreases resolution. The theoretical resolution limits of the objectives listed above (when uniformly filled) are (at 750 nm): 0.83 μm (65×); 1.1 μm (50×); 1.8 μm (15×); and 4.6 μm (6×).

4.3.1 White-Light Reflectance Scanning

Since the system was also designed to perform reflectance measurements, the lower magnification objectives have a usefulness for VCSEL measurement which the high-power ones do not. When obtaining data from a resonant and angularly sensitive device like a VCSEL, a large collection angle effectively integrates over a large number of states of the system (see Appendix B). The collection (half) angle of an objective is related to its numerical aperture by

$$\theta_c = \sin^{-1}(\mathrm{NA}/n_0), \tag{36}$$

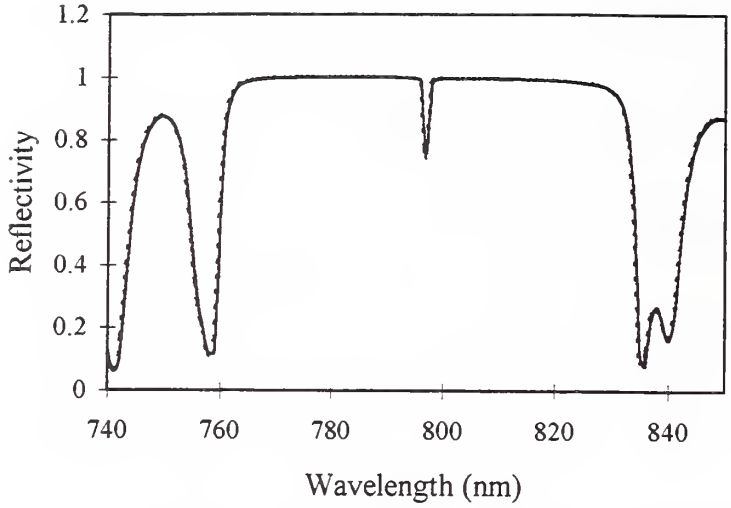

Figure 18: Simulated reflection spectrum of a typical VCSEL structure. The solid line is the 0° reflection spectrum with a collection angle of 0°, the dashed line is the same spectrum integrated over 5.7°, corresponding to the 6× objective used in the experiments.

where n_0 is the index of the surrounding medium (in this case, air; $n_0 = 1$). It stands to reason that the 6× objective, with its 5.7° collection angle, is the best suited to performing reflectance measurements since the lower collection angle will not blur the reflectance features as much as a high-angle objective; Fig. 18, which shows little difference between the 0° simulated reflection spectrum of a VCSEL and the same simulation integrated over 5.7°, bears this out. There is little difference in the spectra, and little change in the resonance wavelength or its Q factor. As noted in Sec. 4.5.1 below, this system was best suited to high-resolution (spectral) measurements.

4.3.2 Polarization-Resolved Measurements

Also included was a rotating mount for a polarizer, at a point in the collection path (see Fig. 17) where only the emitted light would be affected. The most important application of polarization spectroscopy to this work is that the emissions from quantum wells corresponding to light- and heavy-hole recombination are orthogonally polarized due to the magnetic quantum number selection rule for transitions between the conduction ($J_z = \pm 1/2$) and light- ($J_z = \pm 1/2$) or heavy-hole ($J_z = \pm 3/2$) levels. The selection rules arise from the strength of transition matrix, which involves the dot product of the light polarization (ε) and the dipole moment ($e\mathbf{r}$)[143, p. 338][144, p. 60],

$$f = \frac{2m\omega}{\hbar} < f|\varepsilon \cdot \mathbf{r}|i >, \tag{37}$$

which means that the most probable transitions will be of electric-dipole character. The heavy-hole $\Delta J = \pm 1$ ($J_z = \pm 3/2 \rightarrow \pm 1/2$) transitions are allowed under electric dipole selection rules, but the $\Delta J = \pm 2$ ($J_z = \pm 3/2 \rightarrow \mp 1/2$) are quadrupole transitions. For the light holes, the $\Delta J = 0$ ($J_z = \pm 1/2 \rightarrow \pm 1/2$) dipole transitions have twice the oscillator

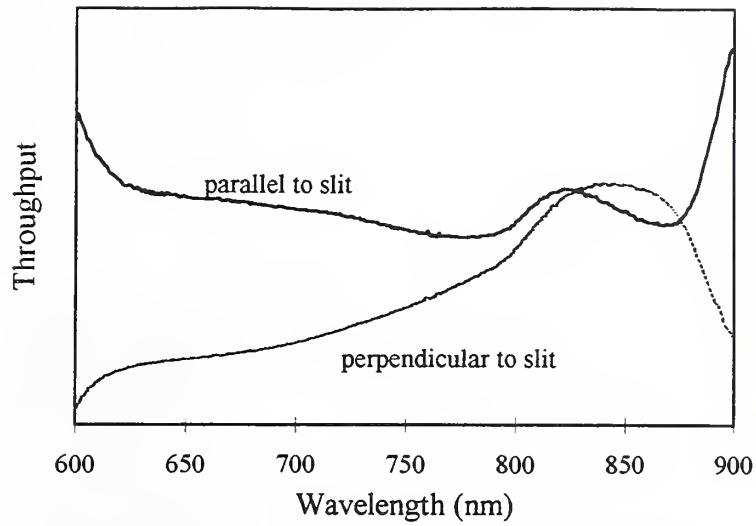

Figure 19: Spectrometer throughput of different polarizations, parallel (solid line) and perpendicular (dotted line) to its entrance slit. The data are normalized to an arbitrary value; the average ratio is approximately 2:1 in favor of the parallel polarization (which is also the direction of the grating rules). The features at the ends of the spectra are due in part to the decrease in source intensity in those regions and (at the long-wavelength end) to the response tail of the photomultiplier.

strength[144] of the $\Delta J = \pm 1$ transitions. Since the absorption coefficient for TE-polarized dipoles is larger than the TM coefficient, most of the optically excited dipoles in the QW are polarized in the plane of the layer. The heavy-hole transitions should thus produce light polarized in the plane of the epilayer and most of the radiation from the light-hole transitions should be polarized perpendicular to this. It is thus possible to discern the side emission from the two states simply by analyzing the collected light. The polarizers used here were Glan-Thompson type, with nominal extinction ratios in excess of 10,000:1.

Since the spectral dependence of the spectrometer throughput for the two polarizations (perpendicular and parallel to its entrance slit) figures largely in making polarized-emission measurements, the measured response is shown in Fig. 19. The throughput ratio evidently changes most dramatically in the 750 to 850 nm region, precisely the region of interest in this study. It is thus important to ascertain the magnitude of the distortion introduced by the spectrometer into the data. Figure 20 shows the corrected and uncorrected data for the light- and heavy-hole recombination for a 3 nm QW. The change in the relative intensity between light- and heavy-hole peaks, apparently, is not substantial, and the only difference in the two sets of curves is a slight decrease in overall intensity. As this effect is not significant, the spectra shown in this work are not corrected for the spectrometer polarization.

4.3.3 Surface-Normal Pumping

In addition to the "standard" XPL experiment where the pump and collection axes were collinear, experiments were also performed with the pump at 90° to the collection path,

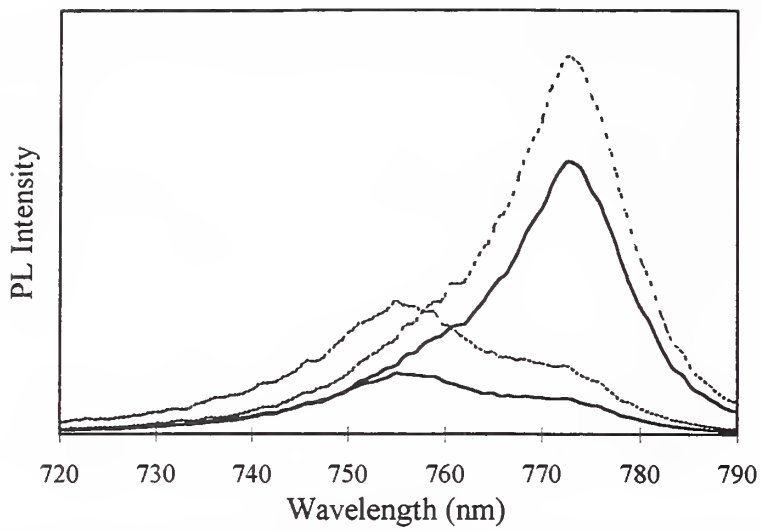

Figure 20: The spectra for the conduction to light- and heavy-hole recombination, including corrections for the spectrometer polarization preference. The solid lines are the uncorrected data, dashed are corrected.

so that the pump beam hit the surface of the specimen perpendicularly. The reason for performing both types of measurements is that as the excitation spot approaches the facet, the emitters will begin to couple more light into the free-space (or continuum) modes. More transverse modes of the cavity will give way to internally reflected guided modes or free-space modes as the point at which the light originates moves closer to the facet. As the quantum well has a relatively high absorption coefficient, if the pump does not excite the barriers in a standard XPL experiment all the recombination will occur a very short distance from the cleaved edge. A rough, order-of-magnitude calculation follows.

Viewing the multilayer mirrors in a VCSEL as an aggregate cladding with an index of approximately 3.2, total internal reflection (TIR) occurs at approximately 18°. A 20-pair mirror of roughly 2.5 μm total thickness thus describes a depth of about 0.8 μm where the totally internally reflected ray will hit the edge of the cleaved facet. The situation is depicted in Fig. 21: the angle β represents all the rays that escape the structure without coupling to a cavity mode. For emission at A, $\beta = \pi - 2\theta_{TIR}$, its minimum value. The last point at which β is a minimum (considering only the direct ray) is B, where the TIR ray hits the edge of the structure. At point C, β is larger purely due to geometry and continues to grow (to a value of π; the maximum full angle, however, is $2\pi - 2\theta_{TIR}$) as the point of emission gets closer to the facet. The excitation point should thus lie at least 1 μm from the cleaved edge in order to probe more of the cavity modes and cavity effects.

For a typical quantum well with an absorption coefficient of 4 μm^{-1}, 99 % of the pump power will be absorbed in a region about 1 μm from surface of the facet and $1/e^2$ of it within 0.5 μm. Owing to the high surface recombination of the cleaved edge, few of the carriers should diffuse far enough in the quantum well to pass far beyond the 1 μm point. The side-pumped XPL measurement is thus a very shallow surface probe, which yields the energy configuration of the quantum well with little influence from the cavity.

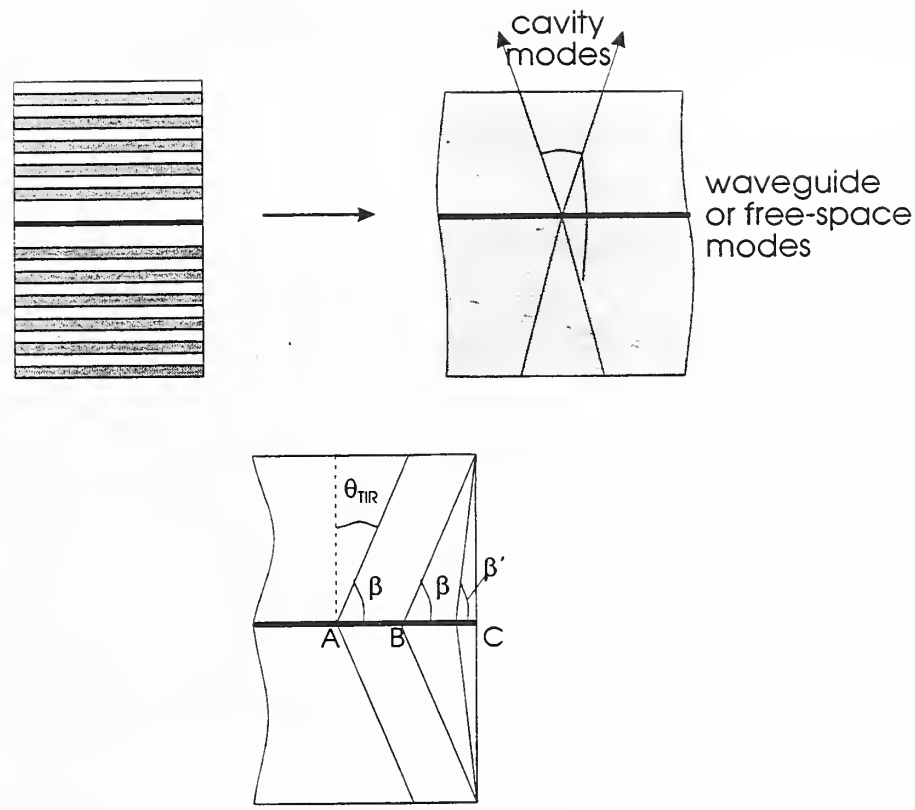

Figure 21: Diagram of internal reflection and coupling to cavity or free-space (continuum) modes for emission from different points inside a VCSEL. All the radiation emitted into angles less than β goes into guided or free modes, all that into angles less than θ_{TIR} goes into cavity modes.

Pumping from the top of the structure (through a low reflectance point in the mirror), on the other hand, allows regions beyond the (roughly) 1 μm limit to be probed, and collecting the emission from the side allows acquisition of spectra that are free from the etalon-filtering effects of surface-normal emission. Comparison of these two techniques, for points not greatly disparate on the wafer, should reveal cavity-induced effects, such as level shifts and mode splitting, in the energy configuration of the quantum wells.

4.4 General XPL Considerations

4.4.1 Probe Absorption

There are several important reasons for concern over the difference in how much pump light is absorbed in XPL versus standard NPL: under higher excitation levels, the bottom of the band can become saturated with carriers (the Burstein-Moss shift); the index of refraction is dependent on the free carrier density and hence multilayer structures can "bleach" at high power; the emission efficiency, especially in quantum wells, can start to degrade as more carriers are excited, then thermally decay into the band, and more phonons are generated; and, perhaps most importantly, the heating of the specimen under high excitation shifts the energy gap and hence the emission peak. In order to generate an order-of-magnitude comparison, a calculation of absorbed power for typical NPL and XPL experiments follows.

Even when the input power is kept constant, the excitation (absorbed power) can vary dramatically between the surface-normal and cross-sectional probes. This difference arises from the fact that the pump power available for excitation in the top-surface-normal case is limited only by the diffusion length of the carriers (and by heterostructure barriers such as the ends of the cavity spacer in a VCSEL), whereas the side pump is limited by the depth of focus of the system. In the top-pumped case, the thickness of the quantum well will always be less than the depth of focus of the objective, but in the side-pumped case, the lateral extent of the structure is almost guaranteed to be greater than the depth of focus of the objective. In other words, the top pump can possibly excite both the barriers and the QW over the entire area of the beam, whereupon the carriers that diffuse into the QW will recombine and the emitted light will be imaged properly in order to be detected. The side pump can excite regions outside its depth of field, but these will not be imaged properly, and the carriers that contribute via diffusion must recombine in the region of the QW that lies in the focal plane.

As an example, consider a simple quantum well structure, GaAs surrounded by AlGaAs, with a focused excitation beam incident from either the surface or the side, as shown in Fig. 22. The beam is taken to be Gaussian (though the radial variation will be ignored because all calculations will implicitly involve an integration over the radius of the beam), and the AlGaAs of sufficient purity that carriers can diffuse the entire length of one of the barriers (in order to recombine in the QW). For simplicity, consider first the case where the pump wavelength is such that the barriers do not absorb it.

In the surface pump configuration, the energy density incident on the imaged area of the QW is a function of the area of the Airy disk and the thickness of the well. The fraction of

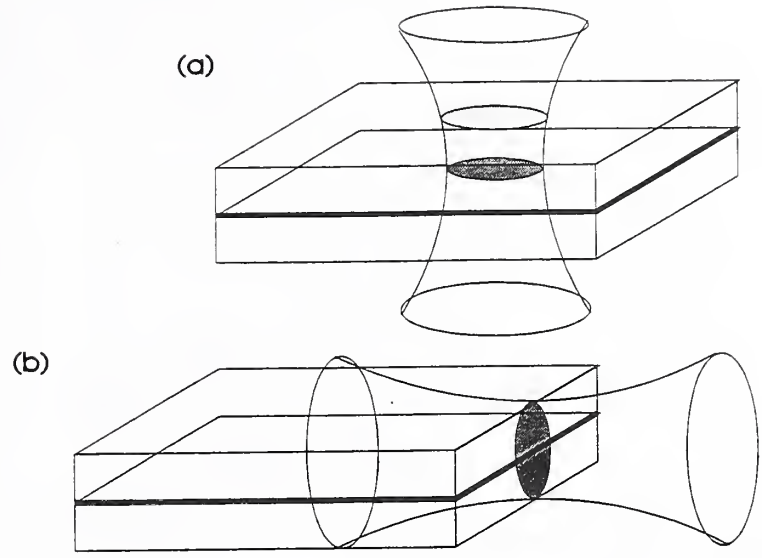

Figure 22: Excitation differences in (a) top and (b) side pumping.

the total energy absorbed is thus proportional to

$$\frac{I_{QW,N}}{I_0} = 1 - e^{-\alpha_{QW} z_{QW}}, \tag{38}$$

where z_{QW} is the thickness of the QW and α_{QW} is its absorption coefficient. (An example of bulk versus QW absorption coefficients is given by Fig. 23.) For a 0.75 μm beam and a 10 nm QW with $\alpha_{QW} \approx 3\ \mu\text{m}^{-1}$, the total absorbed power works out to about 3 percent of the beam.

In the side pump case, only the profile of the QW is presented to the beam; in this case only 0.015 μm^2 out of 1.77 μm^2. There is a further limitation (even for extremely long diffusion lengths) in that an NPL measurement can effectively confine the emitting region within its depth of field, whereas XPL is always limited to the depth of field of the system. Note that this pertains to the entire imaging system: the depth of focus of whatever is used to image the signal onto the spectrometer slits will also have an impact on what gets recorded. Only if the objective is f/#-matched to the spectrometer is the "system depth of field" approximately that of the objective (in this case, roughly 5–15 μm, depending on the definition; see Refs. [146, p. 28] and [142, p. 489–490]). In the example above, the beam will be reduced by 99% after approximately 1.5 μm, which is quite a bit smaller than the depth of field of the objective. In this case, the optics at the entrance slit focus to f/8, which is a lower divergence than the spectrometer at f/6.9.

Assuming that this situation pertains, the fraction of total energy absorbed is approximately the ratio of areas:

$$\frac{I_{QW,X}}{I_0} \approx \frac{2 z_{QW} w_0}{\pi w_0^2}, \tag{39}$$

which turns out to be about 0.008, or about one-quarter of the surface pump.

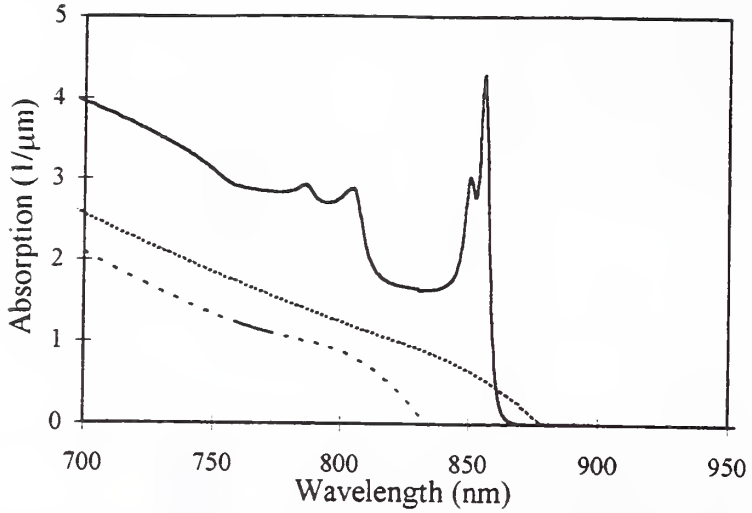

Figure 23: Absorption coefficients for a QW (solid line), bulk $Al_{0.05}Ga_{0.95}As$ material (dashed line) and bulk GaAs (dotted line). The bulk absorption is from the model of Terry[37] and the QW absorption is from a model by Leburton[145].

It is also instructive to ascertain the effect of carrier diffusion on the two pump orientations. In order that this should resemble a VCSEL experiment, the thicknesses of the barrier should be close to the value for a typical single-wavelength cavity, say $z_{cav} = 0.5$ μm (0.25 μm for each barrier). The absorption coefficient depends on the alloy composition, of course, but at 750 nm, only alloy compositions below about 17% Al will absorb the pump. For $Al_{0.05}Ga_{0.95}As$, the absorption coefficient at this wavelength is roughly 1.34 μm^{-1}, meaning that 99% of the beam will be gone in about 3.4 μm. As this is a sizable distance on this scale, it is worthwhile to consider the profile of the beam.

Taking the z-axis as the growth direction (perpendicular to the plane of the QW) as in Fig. 22b, with the QW at $z = 0$, the radius of the waist of the beam propagating along the z axis is

$$w(z) = \sqrt{w_0^2 \left(1 + \frac{z^2 \lambda}{\pi w_0^2 n}\right)}, \tag{40}$$

where w_0 is the minimum waist. If $w_0 = 0.75$ μm and $\lambda = 0.75$ μm, the waist at the surface of the structure (assuming it is focused at the QW) is only about 0.5% larger than the minimum waist (for $n = 3$). Thus it is adequate to treat the beam as a cylinder. From a point in the cylinder near the middle of the top barrier, the disk focused on the QW subtends a solid angle of $2\pi \tan^{-1}(2w_0/t) \approx 2.8\pi$, so the fraction of carriers that diffuse into a detectable region, assuming $\mathcal{L}_D \gg 0.25$ μm and that any carrier has equal probability of scattering along any direction, is roughly $2.8\pi/4\pi = 0.7$. Taking $\alpha = 1.34$ μm^{-1}, 28.5% of the beam is absorbed by each barrier, and 3% by the QW, so $0.7 \times 2 \times 28.5 + 3 \approx 43$ percent of the beam is absorbed and contributes usable electron-hole pairs to the recombination process.

For the side-pump case, the contribution of the QW remains the same (as when the barriers did not absorb), but now the barriers can contribute as well. Carriers which contribute

to properly imaged recombination will be generated within a sphere of radius approximately equal to the diffusion length and centered about the QW (at the facet). The distance over which the entire pump is absorbed (3.4 μm) is on the order of magnitude of some of the best diffusion lengths reported in AlGaAs alloys[147], so let us set $\mathcal{L}_D = 3.4$ μm for this calculation just to have an estimate. If this value correct, then half of the carriers will diffuse a distance of 3.4 μm or more. Though the solid angle subtended by a sheet through the middle of a hemisphere from any point inside the hemisphere is an integral of arctangents which has no indefinite form or approximations, the maximum value is apparently close to 2π (for a point next to the sheet), and the minimum is half the solid angle subtended by a circle at a point one radius above its center, or about $2\sqrt{2}\pi/16\pi \approx 0.18$.

If one fourth of the carriers inside the sphere diffuse to the QW, the fraction of the beam converted to useful electron-hole pairs is then $0.25 + 0.008 = 0.258$, which is about 30 times larger than when the barriers did not absorb the pump. This is now a factor of two closer to the surface-normal absorption and that most of the carriers are generated outside the QW (as in the surface-normal case).

The trade-off (which of course must exist) for greater excitation is that higher absorption in the barriers means greater heating. When heat is generated only in the QW, a large thermal mass on either side provides great stability. In addition, one might expect that the surface-normal case, being fully surrounded by dielectric material rather than partially surrounded by air, would suffer a slower onset of thermal effects, but in the case of a VCSEL, the distribution of the pump field (see Sec. B.1.4), can negate these other considerations entirely.

The net result of all this is that the contribution of carrier diffusion can help to compensate for the area differential between cross-sectional photoluminescence measurements and surface-normal ones, even though greater heating may occur. It can thus be advantageous to pump the barriers in an XPL experiment. All spectra taken for this work, however, were taken at power levels where thermal effects were insignificant.

4.4.2 Waveguiding and Field of View

As mentioned previously, there is reason to be concerned about the coupling of side emission to waveguide modes, thereby altering the measured XPL spectrum. A VCSEL, viewed as a slab waveguide, has a number of modes with very non-uniform intensity distributions. However, since all the light in the waveguide modes is confined to the structure itself, it is prudent to ask first how much of the surface of the facet is sampled in an XPL experiment.

Although the size of the laser spot is effectively diffraction-limited and, as shown above, often of sub-micrometer radius, the field of view of the objective is in general many times larger. This is what determines the sampled area of the facet.

This area is limited primarily by the dimensions of the spectrometer slits and the diameter of the collection lens ahead of the slits. If the beam is collimated, the width of the image of the slits (at the focal plane of the collection objective) is given by the ratio of the focal lengths of the lenses. For the 50× objective, the focal length is approximately 3 mm; the collection lens has $f \approx 40$ mm. Typical maximum slit settings in this work were 200×200 μm, so the

slits cut the sampling off at approximately 15 μm, which is greater than the thickness of a simple VCSEL structure. The field of view (in the focal plane) is found from

$$y = \frac{fy'}{l}, \tag{41}$$

where f is the focal length of the lens, y' is the field-stop radius (in this case the collection lens), and l is the distance from the lens to the field-stop. For a lens 12.5 mm in radius, 1 m away from a lens with $f = 3$ mm, this works out to a field of view (radius) of about 40 μm, so the lens does not vignette the collected light. Given the slit limitation of 15 μm the system pictured in Fig. 17 thus samples the entire facet of a typical VCSEL and redistribution of light intensity by waveguiding effects is not of concern as long as the collection path is not spatially filtered to a much greater degree than described above.

Even if the field of view is smaller than that calculated above, modeling of the VCSEL as a slab waveguide shows that the coupling to the guided modes is not very strong and that the spatial distribution of those modes lies mostly in the mirror layers (for all the low-order modes studied). Thus, any spectral effects that arise because of a spatial redistribution of guided modes can also be expected to be minimal due to the small coupling and uniform redistribution.

4.5 Ancillary Measurements

Since modeling plays a significant role in this work, it is important to discuss briefly how some of the construction parameters for the models were obtained. The quantities of most concern in a VCSEL are thicknesses and alloy concentrations, both for the mirrors and for the cavity spacer. Since ordinary cross-sectional photoluminescence is very good at determining alloy concentrations (or at least peak emission energies from the alloys), the problem remains to determine the thickness of the layers.

4.5.1 Spectral Reflectance

Spectral reflectance measurements were performed on one of two systems. The first was a commercial spectrophotometer, limited to approximately 2 nm wavelength resolution. The second was a modification of the XPL apparatus discussed above, using the double-pass spectrometer (0.01 nm resolution). The disadvantage to the second system was that it was necessary to use objectives and other transmissive optics to collimate the light. The absolute calibration of measured reflectivity with standards (aluminum mirrors) using the spectrophotometer was thus more accurate than the spectrometer system.

Thicknesses were determined by matching modeled data to experimental observations, often using "canned" optimization routines built into commercially available software. Fine tuning could be done by varying the layer thicknesses individually or allowing for thickness gradients.

With adequate optimization routines, a reflectance modeling algorithm can often actual determine layer thicknesses with a good degree of accuracy provided that the match to the

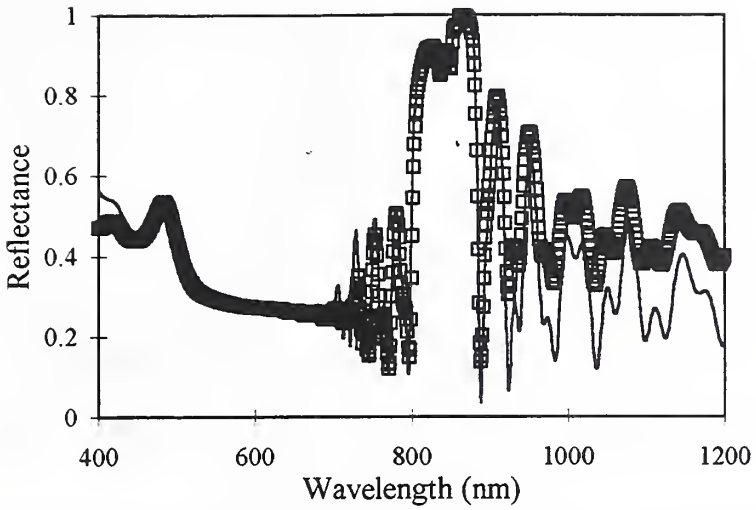

Figure 24: An example of a well-modeled spectral reflectance curve. The open squares are the data; the solid line is the model.

target data is not terrible to begin with, as illustrated in Fig. 24. (The mismatch at long and short wavelengths in Fig. 24 also highlights the importance of accurate index models, as discussed in detail in App. B.) Mathematically, however, a particular fit to a reflectance spectrum need not be unique (see App. B), so it is practical to have a second measurement to corroborate the thicknesses determined by reflectance modeling.

4.5.2 Double-Crystal X-ray Diffraction

X-ray rocking curves were taken with a double-crystal diffractometer, with 0.1 arc-second resolution. The primary collimation of the X-ray beam was accomplished with a GaAs crystal cut along its (004) facet. The source was the Cu$K\alpha$ doublet at approximately 0.154 nm; a mechanical slit system was used to filter out the $K\alpha_2$ radiation from the more intense $K\alpha_1$ line.

The azimuthal rotation of the specimens was optimized for the maximum Bragg reflection and measurements were taken at 0° and 180° in order to correct for slight misorientations of the epilayer and substrate planes. Information on mirror pair thickness can be obtained simply from the spacing of the satellite peaks in the X-ray diffraction spectrum, as exemplified by Fig. 25. Analysis of the data (often involving a curve-fitting process similar to the reflectance analysis) was carried out after the fashion described by Christensen et al.[52]. As documented therein, the discrepancy in alloy contents in the $Al_xGa_{1-x}As$ system between X-ray diffraction and luminescence is approximately 1.8 percentage points of Al. The disagreement in thickness determination (with spectral reflectance and transmission electron microscopy), however, is as low as 0.8%.

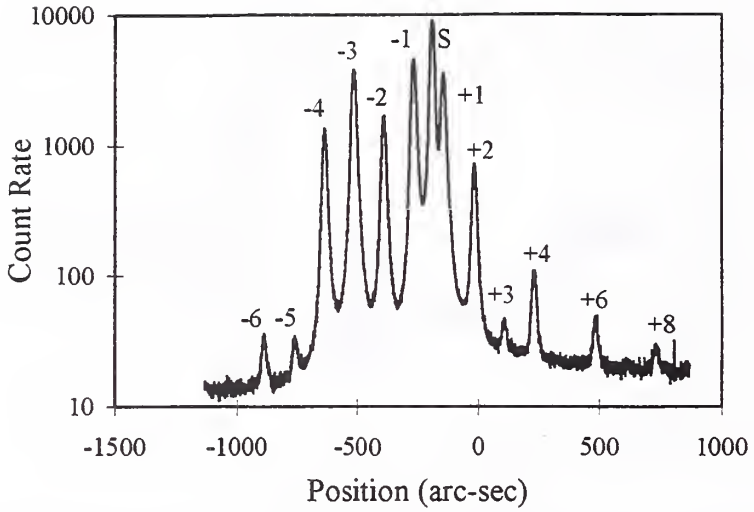

Figure 25: An example of a double-crystal X-ray rocking curve for a VCSEL. The order of reflection is noted beside each interference peak; "S" denotes the substrate peak.

5 Emitter Coupling

5.1 VCSEL Cavity Effects and Side Emission

When attempting to model the surface-normal emission data, the question of the validity of using the cross-sectional data as a basis arises. A number of factors n the side emission spectra do not exist in the surface-normal. Beyond the simple concerns, there is the larger question of whether cavity coupling even plays a significant role in planar structures (where there is no mode degeneracy and the mode volume is extremely large) with distributed feedback (where the feedback from the mirrors within the range of causality may not be large enough to have an effect). Can we detect cavity-induced effects using a side-emission probe?

Indeed, modeling and metrology are not the only reasons to look for cavity effects in VCSELs using side emission. Though the reports of cavity-induced modifications in emission from and performance of VCSELs are numerous (see Ch. 2), there have been no reports of side emission measurements from such devices. Yet few unambiguous probes of cavity modifications in VCSELs are as simple or as revealing as side emission measurements. When coupled with some very simple modifications such as polarization selection and alternate pump orientations, side emission does indeed become a very powerful tool for examining cavity effects.

5.2 Top- and Side-Pumped XPL

In order to probe sections of the VCSEL structure where cavity effects would be more significant (see the discussion in Sec. 4.3.3), the specimen was excited surface-normally (from the top) while the side emission was measured. The difference between top- and side-pumping,

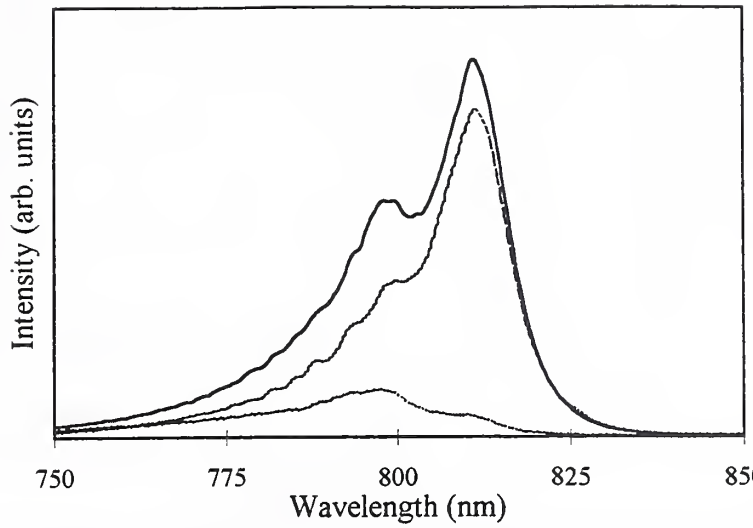

Figure 26: Polarization-resolved side emission from a simple, single quantum-well structure. The solid line is the unpolarized data; the dashed and dotted are orthogonal linear polarizations of the emitted light.

as explained earlier, is the difference between exciting emitters at point A in Fig. 21 or exciting them at point C. However, a number of other effects could result in spectral behavior similar to mode-splitting, and these need to be accounted for first, before emitter coupling can be given credence.

5.2.1 Eliminating Competing Processes

Two structures were used for this study. The first was an ordinary quantum well, sandwiched by $Al_{0.3}Ga_{0.7}As$ barriers, used as a control. The second was a single-quantum-well, single-wavelength-cavity VCSEL with mistuned cavity resonance and quantum well emission peaks. Because the Rabi splitting should vary with the detuning, this specimen was expected to be a good candidate for such behavior.

Among the other possibilities that must be ruled out before a bimodal spectrum can be attributed to Rabi oscillations is the lifting of the valence band degeneracy in a quantum well: conduction electrons can recombine with light and heavy holes to emit radiation of different energies. As has been documented[144, Ch. 3], these transitions have different selection rules and produce radiation that is orthogonally polarized. Thus, simple polarization selection can identify this phenomenon easily.

Figure 26 shows the side emission from a simple quantum well structure, with both emission polarizations resolved. The unpolarized emission (solid line) clearly segregates into two distinct peaks (dashed and dotted lines), corresponding to the light- and heavy-hole recombination.

Another important consideration is the "subtractive filtering" of the etalon. As shown in Sec. 3.3.1, the normalized intensity transmitted at a given frequency along any angle can greatly exceed unity (when the emitter is between the mirrors), and as explained in

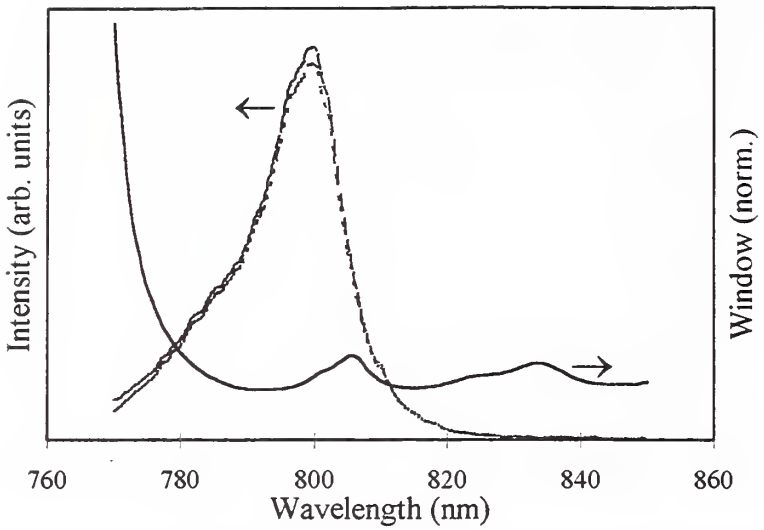

Figure 27: Subtractive filter window for a single quantum well VCSEL. The basis spectrum (dashed line) does not change much when the subtractive filter effects are accounted for (solid line).

Sec. 3.5.1, conservation of energy demands that those frequencies favored in surface emission (up to the total internal reflection point) should be absent from the side emission. Since the redistribution is very strong at the cavity resonance, we anticipate seeing a strong attenuation of frequencies near that point in the side emission. If Eq. 15 is applied to a VCSEL and then integrated, we may obtain a "window" that describes the subtractive filter for the XPL spectrum caused by the conservation of energy constraint.

The filter window, for a single-quantum-well VCSEL specimen — that which exhibits a mode splitting — is shown in Fig. 27, which also plots the impact of this filtering on the XPL spectrum of the emitter. Though one might expect a sort of step-function response, owing to the continuous blue-shift of the cavity resonance, this is not the case in Fig. 27. The reason for this is simple: as the cavity resonance blue-shifts with increasing angle, so does the dip at the long wavelength end of the high-reflectance band. The combination of the two serves to flatten the overall response. As is apparent from Fig. 27, the actual spectrum is not greatly altered by this effect, in this particular device.

Finally, there are general concerns of how well the emission spectra for top and side pumping should match under noncavity conditions. Figure 28 is the top-pumped side emission spectrum of the quantum well structure, which is identical to the side-pumped spectrum of Fig. 26 (dotted line). The unanalyzed spectrum of Fig. 28 resolves into two polarizations which segregate the two peaks, much the same as in Fig. 26. The higher tail on the long-wavelength side of the top-pumped spectrum may be due to excitation of the GaAs substrate or buffer layer. However, the surface-normal pumping does not change the side emission considerably.

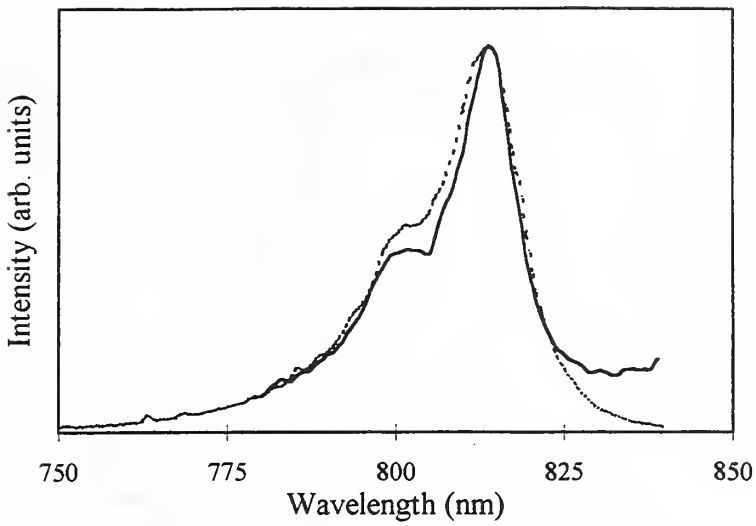

Figure 28: Unpolarized side emission from the quantum well control structure when pumped from the top (surface-normal). The dashed line is the unpolarized data from the side-pumped spectrum.

5.2.2 Measurements in VCSEL Cavities

The side-pumped side emission of the VCSEL structure is shown in Fig. 29; its reflectance spectrum is shown in Fig. 30. For the VCSEL, the mode is at 811 nm and the quantum well peak at approximately 800 nm. The measured Q factor was approximately 2500; since the QW is detuned to shorter wavelength than the cavity resonance, the absorption at 811 nm is low and this Q is probably very close to the cold-cavity value.

Figure 31 shows the side emission obtained from the VCSEL when pumped from the top, along with the two orthogonal polarizations. Due to the resonant distribution of the pump field in the VCSEL structure, the power density was reduced significantly when pumping from the top, from approximately 2.5 mW/μm^2 (250 kW/cm^2) to 0.1 mW/μm^2. However, in both cases — side- and top-pumped — no evidence of thermal effects was observed. The three spectra in Fig. 31 have been normalized to a common value for comparison. The obvious distinction between orthogonal polarizations as seen in Fig. 29 is absent from Fig. 31, indicating that the two peaks are not just a different ratio of the emission from the two valence bands.

As indicated in the analysis above, the subtractive filtering for this structure is not likely to have a significant impact on the side emission. The absence of polarization differences strongly indicates that light- and heavy-hole emission is not responsible for the two peaks in Fig. 31. A great number of other factors such as impurities and structural defects can be dismissed as causes of the differences between the top-pumped (Fig. 31) and side-pumped (Fig. 29) spectra, simply by the fact that dramatic changes like this, occurring in within a few micrometers of each other, are not consistent with the measured uniformity of the wafer and by the fact that this difference reproduces at varying locations on the wafer.

One remaining consideration is the effect of reabsorption of light (propagating along the

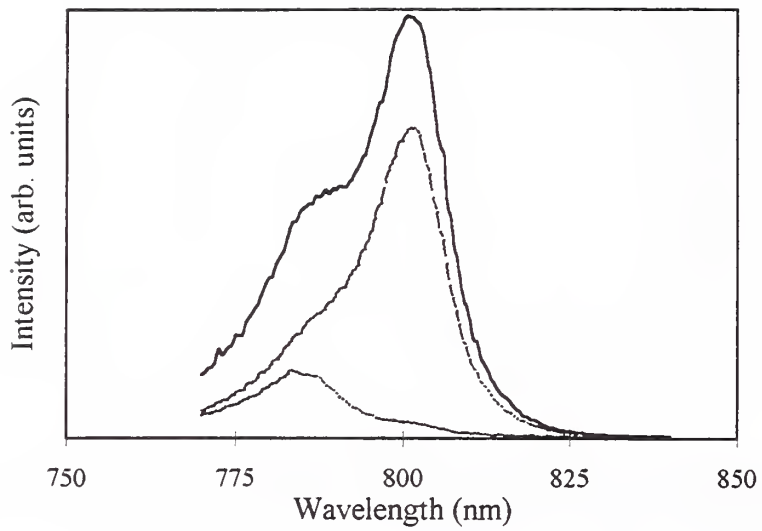

Figure 29: Side emission from the detuned VCSEL structure when pumped from the side, perpendicular to the cavity axis. The solid line is the unpolarized data, the dashed line is polarized in the plane of the QW, and the dotted line perpendicular to it.

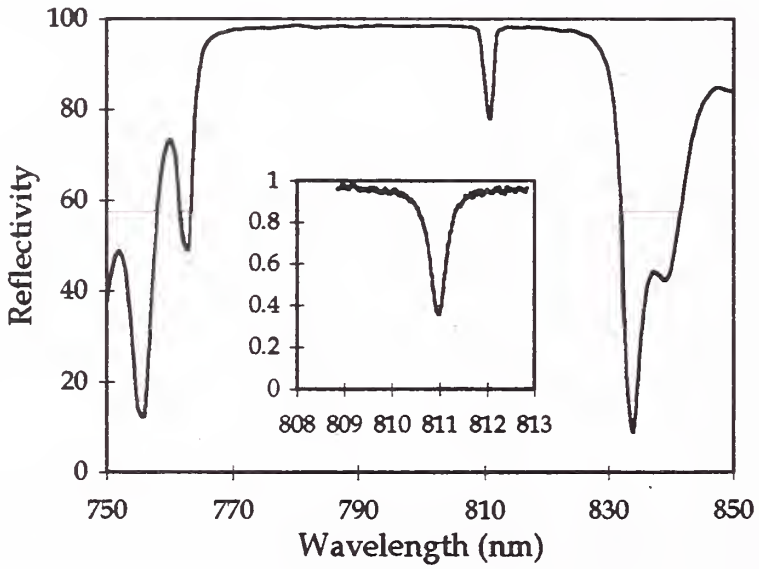

Figure 30: Reflectance spectrum of the VCSEL structure, showing the cavity resonance in detail (inset). The mode at the point where the emission measurements were taken occurs at approximately 811 nm.

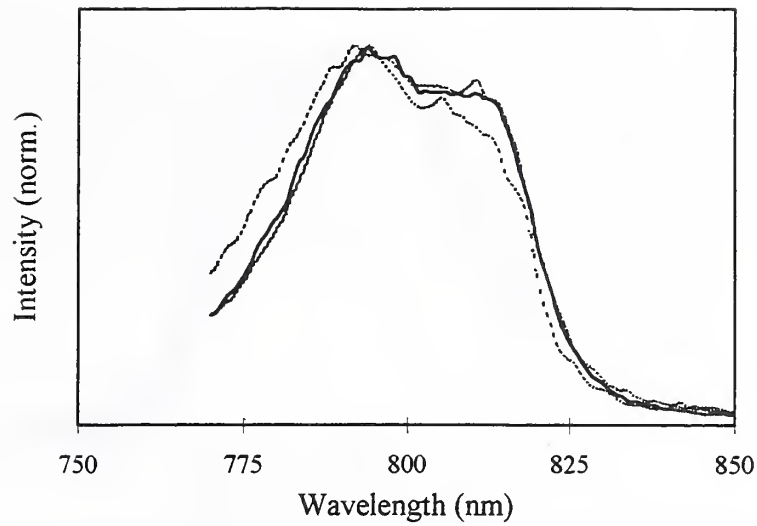

Figure 31: Side emission from the detuned VCSEL structure when pumped from the top. The solid line is the unpolarized data, the dashed is polarized in the plane of the QW, and the dotted perpendicular to it.

waveguide) by quantum well excitons, as is known to happen in edge-emitting lasers. That the dip in the spectra of Fig. 31 is not a manifestation of an absorption phenomenon different from the resonant absorption of Rabi oscillations was determined by moving the excitation spot further from the facet, whereupon the character of the spectrum remained constant (though its overall intensity decreased). Neither did the spectrum change character when the pump wavelength was changed, indicating that pump-coupling effects are not significant here.

Thus, with the other significant causes eliminated, it seems reasonable to conclude that this splitting is due to Rabi oscillation, but it is also possible (and logical) to compare the magnitude of this splitting with theoretical predictions and with other values obtained for VCSELs.

5.3 Modeling the Data

As shown in Sec. 3.2.1, the splitting between the levels in a coupled system is (Eq. 8)

$$\mathcal{E}_n^+ - \mathcal{E}_n^- = \hbar\omega_{n,\delta} = 4\hbar\sqrt{|\mathcal{V}_0|^2(n+1) + (\omega_0 - \omega)^2} = \hbar\sqrt{\Omega_R^2 - \delta^2}. \tag{42}$$

By fitting the data with a pair of Lorentzian lines, as in Figure 32, the magnitude of the splitting ($\hbar\omega_{n,\delta}$) can be gauged. The fit we arrive at from the data in Fig. 32 works out to a splitting of roughly 40 meV. Using Eq. 42, then, we can estimate the so-called vacuum-field Rabi splitting,

$$\hbar\Omega_R = 2\hbar g\sqrt{n+1} = e\mathbf{r}\cdot\mathbf{E}_{cav}, \tag{43}$$

and by some manipulation of Eq. 42,

$$\hbar\Omega_R = \sqrt{(\hbar\omega_{n,\delta})^2 - (\hbar\delta)^2}. \tag{44}$$

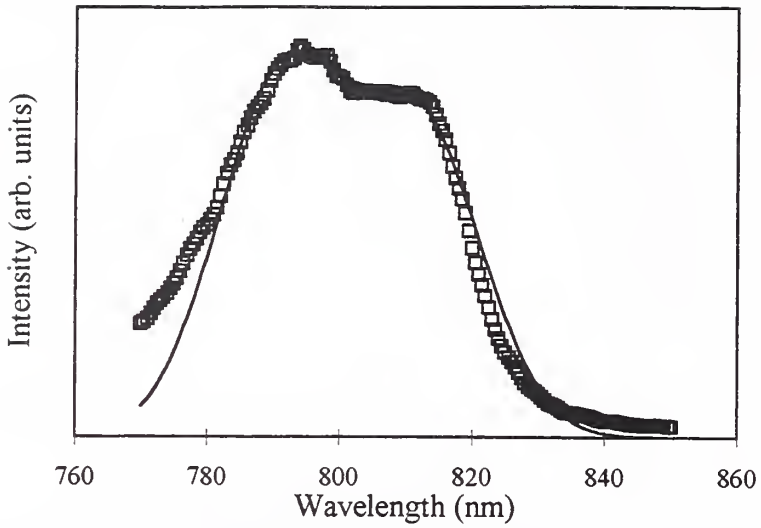

Figure 32: Fit of model (solid line) to data (open squares) for the side emission of the VCSEL structure. The model uses two Lorentzian curves, roughly 11 nm apart and adjusted for slight increases in absorption with longer wavelengths.

The Rabi frequency can be determined by measuring δ (the detuning of QW and cavity) and $\omega_{n,\delta}$ (the splitting of the mode observed in side emission). In this case, the detuning works out to an energy difference of about 21 meV, so $\hbar\Omega_R$ is about 34 meV, or a little less than twice that reported for a simple VCSEL structure by Weisbuch, Houdré, and Stanley[135].

This is not a surprising difference for several reasons. First, the Rabi frequency depends on the magnitude of the cavity (mode) field at the position of the dipole, which can vary quite dramatically even for similar VCSEL structures. As illustrated in Appendix B, the standing field distribution inside the VCSEL is very sensitive to slight changes in construction parameters. Also, though the finesse of this device is very high, the coupling is not truly the analog of discrete oscillators. There are a great many modes in the cavity resonance and a significant thermal broadening to the exciton line, so though the phenomenon can still occur, it is dependent on the overlap of all the mode fields and the spectral profile of the exciton. In addition, the net splitting depends on the integral of all of these overlaps through three dimensions (i.e., the exciton couples to all spatial modes) and the cavity resonance blue-shifts away from the surface normal — in this case, toward the QW peak. The net splitting can thus be larger due to the angular integration, which has not been taken into account here.

Second, the coupling also depends on the effective mode volume, estimates of which can vary significantly in semiconductor microcavities. The degeneracy of modes for an ideal planar cavity is just one, and thus the mode volume is extremely small. In a real VCSEL, however, there are guiding phenomena and other constraints to consider. In any event, any estimate of this number is far from definitive.

Third, the dipole moment estimate used in [135] was based on finding the dipole radius from the oscillator strength via

$$f = \frac{2m_0\omega|<|\epsilon\cdot\mathbf{r}|>|^2}{\hbar}\frac{8}{\pi a_B^2}, \tag{45}$$

where a_B is the three-dimensional Bohr radius of the exciton. These oscillator strengths have been measured and calculated in many sources; Weisbuch et al. draw their data from calculations by Andreani and Pasquarello[148]. The value used in that work was appropriate to a 10 nm GaAs quantum well in 40% AlGaAs, as opposed to 5 nm and an alloy content of 30% in this case. This difference can increase f by as much as 40% and hence $\mathbf{r}$ and Ω_R by about 20%. Taken as a whole, these differences can easily account for a factor of two.

6 Mode Coupling

6.1 The Microwave Cavity Experiment

The purpose of this test of mode coupling was really to determine how to distinguish mode coupling from emitter coupling in plane-parallel cavities. Two system properties had to be controlled in order for the experiment to work: first, the relative positioning of emitter and cavity had to be variable on the scale of $\lambda/4$ or so; and second, the "lifetime" of the source needed to be altered as well. Satisfying the first requirement was easier to do with a large-scale cavity, allowing the work of moving dipoles and cavities relative to each other to be done in dimensions of centimeters rather than nanometers. The second objective — shortening the lifetime of the source so that feedback from the cavity could not occur during the emission cycle, or so that it would only emit during an interval shorter than the time required for light to transit the cavity — would be difficult (to say the least) in a VCSEL, where the transit times across the entire structure can be on the order of hundreds of femtoseconds and the lifetime of the source (usually in the tens or hundreds of nanoseconds) cannot be controlled. On the other hand, this difficulty was easy to overcome with a "mock-up" device using microwaves and a pulsed antenna.

An experiment similar to this one has been performed by Seeley et al[11] (after being proposed by Dowling et al[72]), using a radio frequency emitter and continuous-wave radiation. There are several differences between that work and this one: (1), this microwave experiment was designed to use both pulsed radiation, so that atom-cavity coupling (or antenna-cavity coupling) could not occur, and cw radiation, so that it could; (2), it measured the actual optical power transmitted, rather than taking the difference of incident and reflected power measured through a directional coupler; (3) it compared the transmitted optical power with the reflected electrical power to look for feedback effects; and (4) it was performed on a ground plane, using a monopole source so that coupling to wires and feedthroughs could be eliminated.

6.1.1 Experimental Description

6.1.1.1 The Cavity. The "cavity" itself (see Fig. 33) was made from a 4- by 8-foot block of styrofoam sandwiched between two sheets of square, metallic mesh (of the type often used in leporine enclosures). Several types of mesh as well as metallized plastic and foil-covered ceiling insulation were tested, but a 1/2-inch square pattern mesh had the optimal reflectance

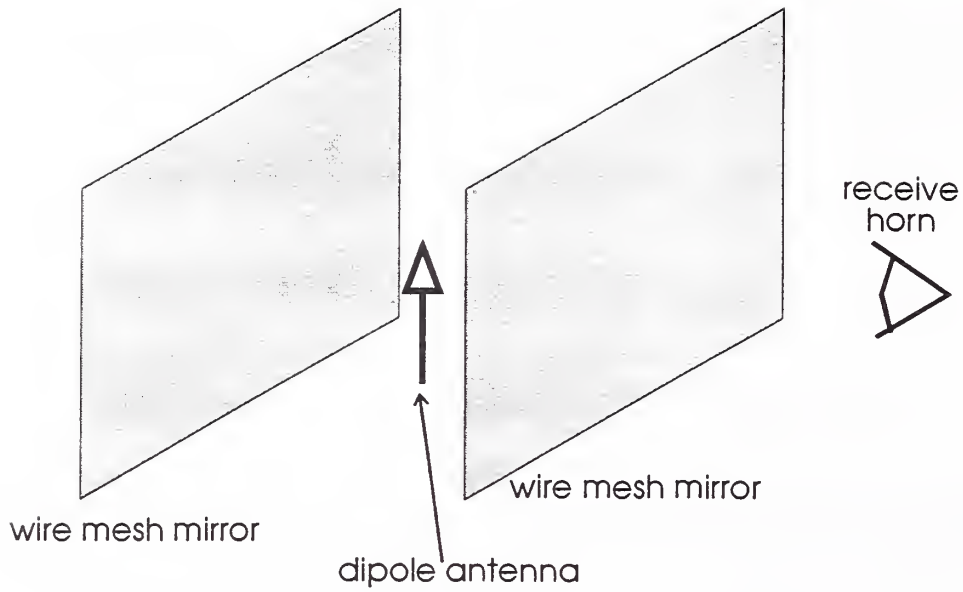

Figure 33: Schematic of the microwave experiment setup.

for our purposes, as calculated from its transmittance, shown in Fig. 34. The reflectivity was chosen by calculating a ring-down time less than the time required for diffracted waves to arrive at the detector. The time differential between the straight ray and the first diffracted ray (which goes directly over the top of the mesh) is

$$\Delta z = \left(\sqrt{z_M^2 + h_C^2} + \sqrt{z_D^2 + h_C^2} - z_M - z_D\right)/c, \tag{46}$$

where z_M is the distance from the monopole to the front mirror, h_C is the height of the cavity, and z_D is the distance from the front mirror to the detector. For $h_C = 1.22$ m, $z_D = 1$ m, and $z_M \approx 0.1$ m, this works out to about 6 ns. The first reflected pulse must transit an extra distance of $2l_c - z_M$, the second $2l_c + z_M$, and so forth. (In this discussion, the term "pulse" may be interchanged with the term "wave" without loss of validity.) For a cavity length of 17.5 cm, this means that approximately 9 reflected pulses (5 that start in the direction of the back mirror and 4 that start in the direction of the front mirror) will arrive at the detector before the diffracted pulse (which must be gated out). The intensity will thus be down (refer to Eqs. 12 and 13) by a factor of $R^{2m} = R^8$. If these first 9 pulses are to approximate the entire series, then the successive terms must contribute little, so it suffices to set $R^8 \approx 0.05$, in which case $R \approx 0.7$. This yields a Q factor of about 13. Higher reflectance, of course means higher Q, but also increases the ring-down time and diminishes the transmittance of the source, the power of which is sufficiently low (and the detector cross section small enough) to warrant concern.

The ideal ($R = 1$) plane-parallel cavity has a mode degeneracy of 1 and zero effective mode volume. For $R < 1$, the transverse modes define the mode volume: as a wave propagates along a nonzero angle (with respect to the cavity axis), the field strength drops by factors of R with each reflection. The lateral distance at which it has fallen to $1/e$ (or $1/e^2$

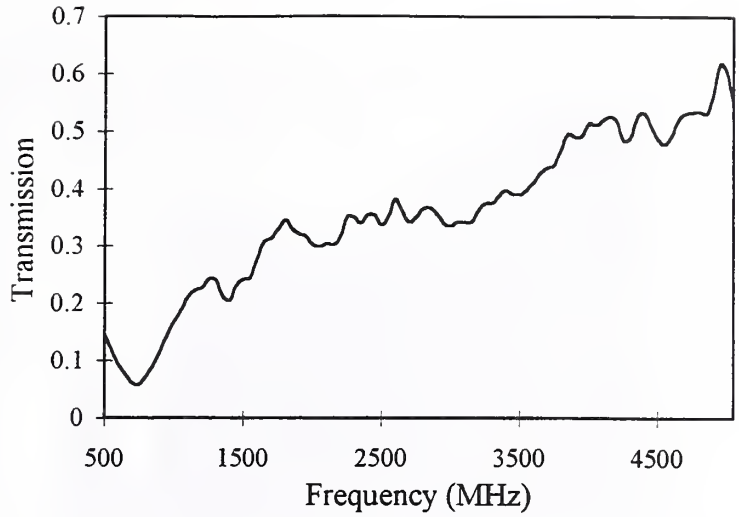

Figure 34: Transmittance spectrum of the square mesh used for the macro-cavity experiment. The dip at ~900 MHz is most likely due to absorption.

or some other convention) of its original strength (when all angles are summed over) can be considered a limit to the mode. In a dielectric cavity such as a VCSEL, other factors such as gain- and index-guiding can also limit the effective mode volume. In this case, a reasonable starting point for the mode volume is the physical volume of the cavity, numerically about 205 000 cm^3. For a fundamental at approximately 1.7 GHz, $\lambda_0^3 \approx 5\ 400$ cm^3. Using Purcell's equation (Eq. 2) in this case means that $\Gamma_{cav} \approx 0.02\Gamma_{free}$, or the lifetime should go up by a factor of roughly 50, if feedback occurs. For $R = 0.7$, the field is down to a quarter of E_0 after only four reflections, so perhaps this estimate is too high. Putting the $1/e$ point at 20 cm off the propagation axis gives a mode volume of about 44 000 cm^3, and $\Gamma_{cav} \approx 0.1\Gamma_{free}$, so the lifetime only goes up by a factor of 10. Apparently, numerical estimates of this effect in planar cavities are difficult to come by. A comparison of the decay rate enhancement and the intensity redistribution, similar to Fig. 10, for this cavity is shown in Fig. 35.

The physical length of the cavity was 17.5 cm, but transmission measurements on the cavity, as shown in Fig. 36, revealed a small inductance to the mesh. This inductance caused a larger reflection phase shift than a perfect conductor, but this could be compensated for by using a cavity length of 18.7 cm in the model. Also shown in Fig. 36 is the prediction of the model using the 18.7 cm cavity length. The entire setup was connected to a large ground plane via conductive tape and a monopole antenna was used, so as to represent the upper half-space of the dipole field (thus preventing any interference or coupling from wires run into the cavity).

6.1.1.2 Antenna and Detector. The monopole used was 75 mm long and resistively tapered to suppress resonance and extend the useful frequency range to 3 GHz[149]. The signals were received by a small, resistively loaded TEM horn antenna formed by a half horn and its image in the ground plane, located about 1 m ($\approx 5l_c$) from the monopole.

The detector was enclosed in absorbing material, as shown in Fig. 37, so as to shield

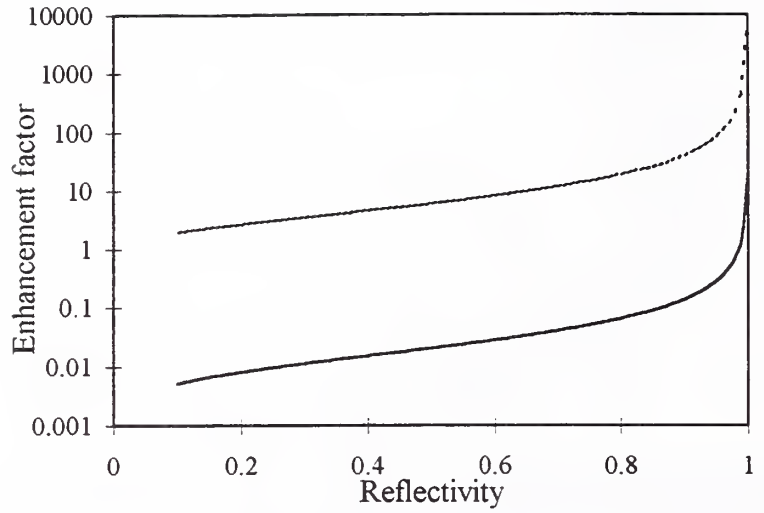

Figure 35: Semilogarithmic comparison plot of enhancement effects in the microwave cavity. The solid line is the lifetime enhancement factor, the dotted line is the normalized intensity ratio on resonance in the surface normal direction. The lifetime calculation is based on an effective mode volume of 44,000 cm^3.

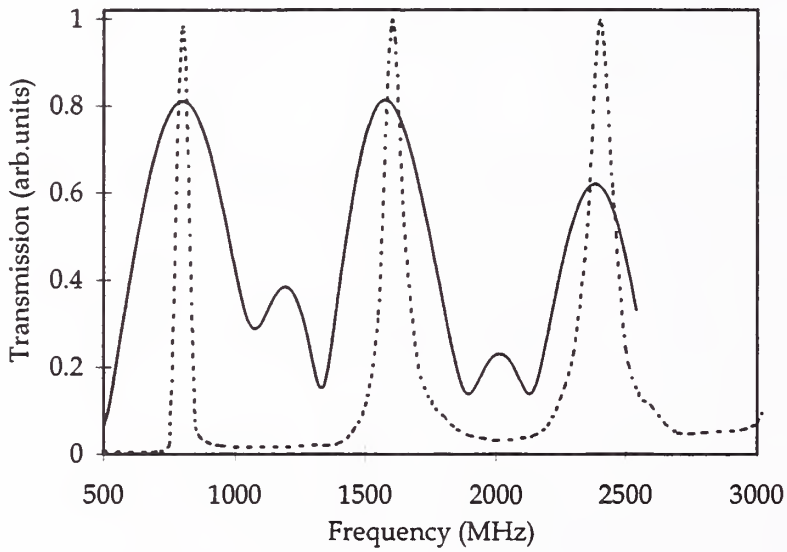

Figure 36: The transmission spectrum of the macro-cavity. The solid line is the (non-normalized) data, measured with a conical (spherical wave) radiator, and the dashed line is the model, based on the transmission measurements of the mesh and a cavity length of 18.7 cm. When normalized, the fundamental mode intensity drops sharply due to the absorption of the mesh below 1 GHz.

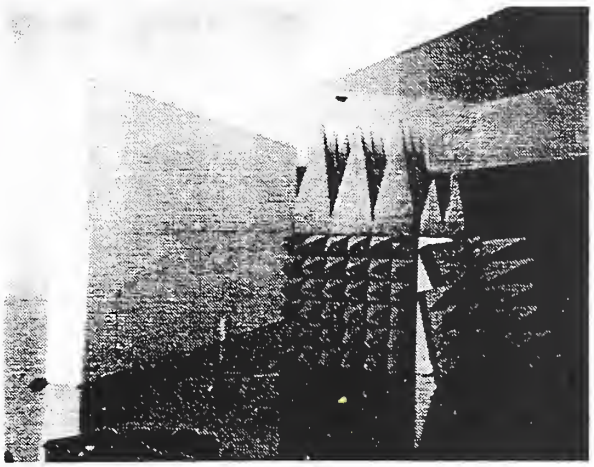

Figure 37: Photograph of the microwave cavity setup, showing the detector enclosure made of microwave absorbers.

it from room reflections and to narrow its cross section (or acceptance angle). Though the distance from the front mirror to the detector was only about five times the cavity length, the low aperture of the detector permitted the spherical nature of the field to be ignored.

6.1.1.3 Pulses and Causality. The experiments were performed in the time domain, using 120 ps pulses of microwave radiation with a useful bandwidth of approximately 3.5 GHz. The Fourier-transformed spectrum of this pulse is shown in Fig. 38a; the pulse itself (in the time domain) appears in Fig. 38b.

The index of refraction of the styrofoam is known to be about 1.02. Given this and the physical length of the cavity, the transit time for light in the cavity works out to approximately 0.6 ns, or 5 times the pulse width. The source, if placed anywhere at a position greater than one-fifth of the cavity length from either cavity wall, should thus have been completely turned off by the time one of its photons could propagate to the edge of the cavity, not to mention back again.

It is entirely possible that feedback could occur, either by damping the actual oscillation in the antenna or by sending electrical signals back to the pulse generator. Yet because the repetition rate of the pulser used was 10 kHz — or the time delay between pulses approximately 0.1 ms — it is difficult to view each pulse as anything other than an independent event. By the time the next pulse is output, the field in the cavity remaining from the last pulse has rung approximately 167,000 times and is down to roughly $R^{330,000}$ $(= 0 \; \forall \; R < 1)$ of its original value. Given these circumstances, it is safe to rule out feedback in this case.

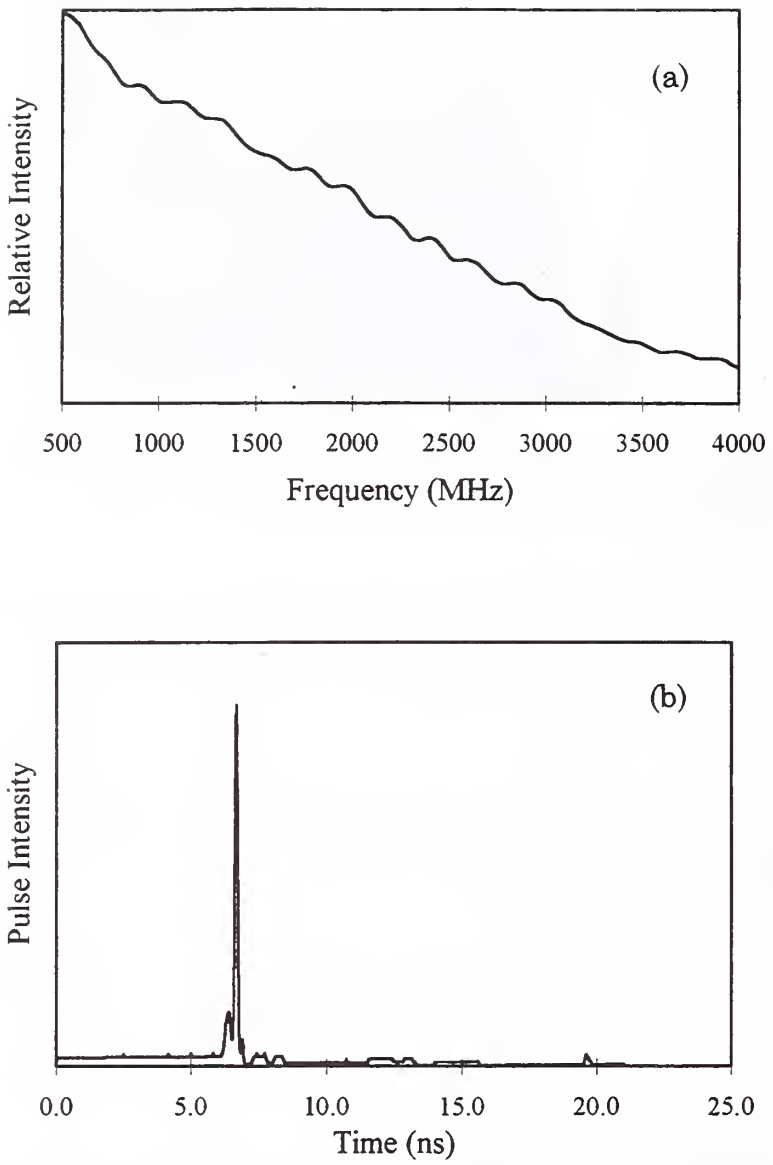

Figure 38: The frequency (a) and time (b) signatures of the microwave pulse used in the macro-cavity experiment.

6.1.1.4 CW Measurements. The continuous-wave experiments were carried out with a network analyzer capable of synthesizing frequencies from 300 kHz to 3 GHz. Optical power was measured using the apparatus described in Sec. 6.1.1.2. The reflected electrical power was also measured in this case, aided significantly by the multiple test ports available on the network analyzer.

Spectra were taken automatically at a sweep rate of 5 s per 801 points across the frequency band, corresponding to an IF-limited bandwidth of 3 kHz. This sweep rate means that each frequency measurement samples the cavity response for approximately 6 ms, which means that the first wave will have bounced about the cavity nearly ten million times. This sampling interval thus allows more than adequate time for the signal to stabilize.

6.2 Microwave Results

The transmittance was measured with the monopole in four different locations along the cavity or $\hat{z}$ axis:

1. in the middle of the cavity ($z = 0$);
2. one quarter of one cavity length from the screen farthest from the detector ($z = -l_c/4$);
3. one quarter of one cavity length behind the cavity ($z = -3l_c/4$); and
4. one half of one cavity length behind the cavity ($z = -l_c$).

The external measurements were made as a control for the internal, in order to ensure that any observed spectral changes were not random. The receiver was located at approximately $z = 5.5l_c$. The time domain data were gated to eliminate the pulses diffracted over the top of the mesh and reflected from the walls of the room (a window of approximately 12 ns), averaged over a few thousand cycles, and then deconvolved by a fast Fourier transform. A reference signal, taken with the cavity removed, was similarly processed and used to normalize the data.

6.2.1 Predictions

The predictions for the dipole located inside the cavity, based on Eq. 15, are shown in Fig. 39. A similar prediction, for the dipole outside the cavity, based on Eq. 16 for the normal transmittance function of a Fabry-Perot etalon, is shown in Fig. 40. The latter is based on the normal transmission function of a Fabry-Perot etalon, which is independent of the location of the source.

Indeed the most noteworthy difference between the predictions for the transmission from the two regions (inside and outside the cavity) is that one of them (Fig. 39) shows a strong dipole-localization dependence, while the other (Fig. 40) does not. The first harmonic at 1.6 GHz clearly disappears from the spectrum of the emitter at cavity center. This localization sensitivity, as shown in Sec. 3.3.1, is characteristic of the energy redistribution for a dipole inside an etalon.

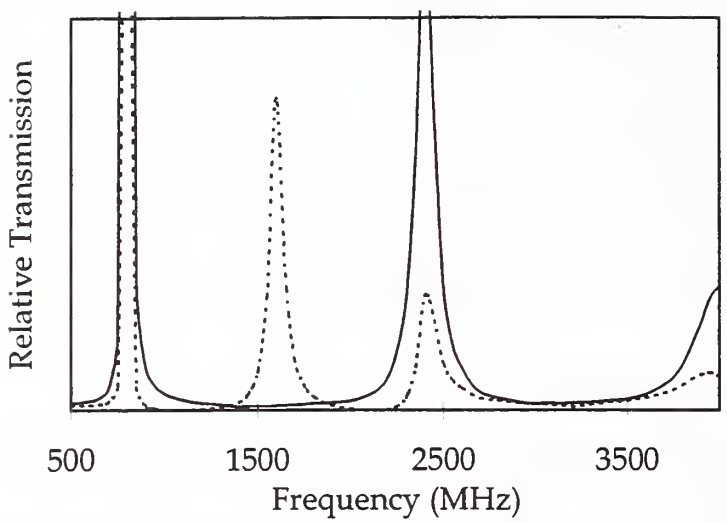

Figure 39: Predictions for the dipole spectrum emitted from inside the cavity. The solid line is for the emitter in the center of the cavity, the dashed line for the emitter a quarter of a cavity length from the back mirror.

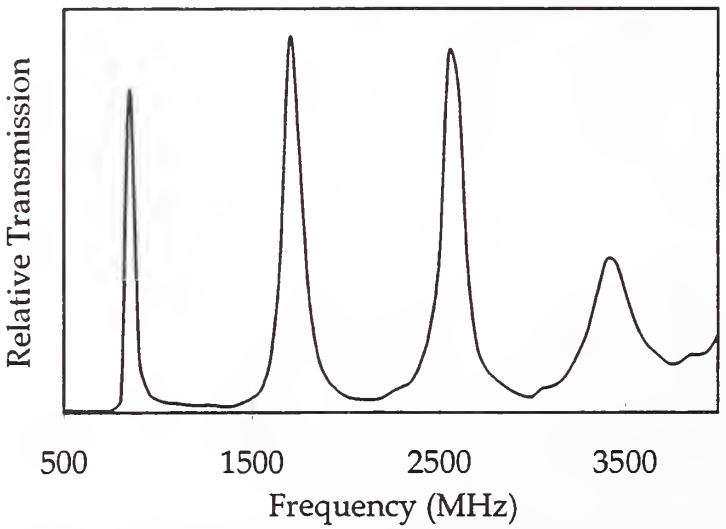

Figure 40: Predictions for the dipole spectrum emitted from behind the cavity, in a normal transmission mode.

What of the linearity of this system? As described above, both cw and pulsed measurements were performed, but it is entirely logical to expect that the cw data should simply be the Fourier transform of the pulsed data. If the system does not respond identically in time and frequency, then there is some nonlinear effect at work, which category feedback might easily fall into. Thus, though the approach may seem redundant, the cw data were taken along with the pulsed simply to verify that feedback had not occurred.

It is also worth considering the mechanism for feedback in this experiment in order to clarify this point. In a true microcavity arrangement, the large field in the cavity would "dress" the atom itself, causing its energy levels to shift and its decay rate to alter (hence changing the flux rate of photons). The physical mechanism underlying this is simply a distortion of the electronic orbitals of the atom by the electromagnetic field.

If the atom is replaced with an antenna, then, what is the mechanism? To begin with, the cavity field can do work against (or with) the driving field in the antenna. From there, it can also conceivably do work against the driving source itself, if the link between source and antenna is bidirectional. Since this experiment uses directional couplers in the case where feedback might occur, the possibility of feedback to the microwave source (somewhere in the electronics of the network analyzer) is greatly reduced.

Thus we need only consider the work done against the driving field in the antenna. If the feedback from the cavity field inhibits radiation (lowers the decay rate), then the flux rate goes down. This is *not* a direction-dependent effect: electrons in the antenna are actually being accelerated (or decelerated) by the external field and are thus emitting fewer photons in *all* directions. By conservation of energy, then, if the incident power from the source is known, the sum of transmitted (optical) and reflected (electrical) power should still equal the input. If less power is transmitted optically, then it must be reflected electrically. The expectation then is that if feedback causes a (spectral) mode to be inhibited (i.e., attenuates its emission), there should be a corresponding increase in the (relative) reflected power. The opposite also pertains: if a mode is enhanced by feedback, then it should reflect relatively less power.

Both of these predictions, localization sensitivity and changes in feedback coupling, should be resolvable in the data below. The comparison of transmitted and reflected power should reveal something about the magnitude of the feedback effect in this cavity, and the measurements at different locations should show a marked difference due to mode coupling.

6.2.2 Pulsed Transmittance Data

The pulsed results for cases 1 and 2, as described above, are shown in Fig. 41. The solid line in Fig. 41, for the dipole in the center of the cavity, shows only one strong mode, at roughly 2.4 GHz where the theory predicts the second harmonic ($3f_0$) should lie, and a small peak at about 800 MHz, where the fundamental should appear. The weak response of the fundamental in this and all subsequent spectra can be attributed to absorption by the mesh, as evidenced by the dip in the transmission spectrum of Fig. 34.

The dashed line in Fig. 41, for the monopole in position 2, shows two strong modes, one corresponding to the second harmonic at 2.4 GHz and another at about 1.6 GHz correspond-

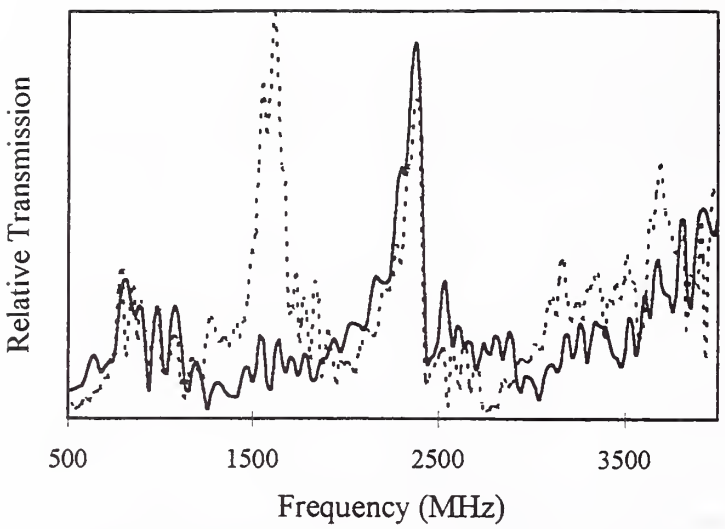

Figure 41: Measured pulsed spectra of the monopole inside the cavity. Solid lines is a half cavity length in front of the back mirror, dashed is a quarter cavity length in front of it.

ing to the first harmonic ($2f_0$). According to Fig. 39, this is exactly the behavior predicted for the dipole inside the cavity.

Figure 42 shows the pulsed illumination spectra of the monopole situated one-quarter of a cavity length (solid line) and one-half of a cavity length (dashed line) behind the rear wall of the cavity (cases 3 and 4 above). In both cases, the three modes (f_0, $2f_0$, and $3f_0$) are again present to varying degrees, but there is no distinct evidence of mode enhancement or mode suppression as in Fig. 41. In fact, there is no indication here at all of any sensitivity to the position of the dipole. The differences in the peaks at 3.2 GHz can be ascribed to the poor signal-to-noise ratio of the source itself in that region (as seen in Fig. 38a). In general, these spectra follow more closely the predictions of Fig. 40, for the usual Fabry-Perot transmittance which does not depend on the location of the illumination source. In any event, the differences between the pulsed spectra of Fig. 41 are much more pronounced than those between the two spectra of Fig. 42, as the mode coupling prediction said they should be.

6.2.3 CW Transmittance Data

The cw emission spectra for the dipole inside the cavity, shown in Fig. 43, show a remarkable resemblance to the same data taken with the pulsed source, in Fig. 41. In both cases, there is a sensitivity to dipole placement which is predicted by the Fresnel-reflection analysis of Ch. 3.

On the other hand, the cw spectra for the monopole outside the cavity (Fig. 44) are somewhat different from their pulsed counterparts. In fact, the external-dipole spectra of Fig. 44 show a localization dependence which is reminiscent of the predictions of the image construction discussed in Appendix D, though the suppression of the first harmonic mode is exactly opposite of that prediction. Yet neither can the simple Fresnel reflection analysis

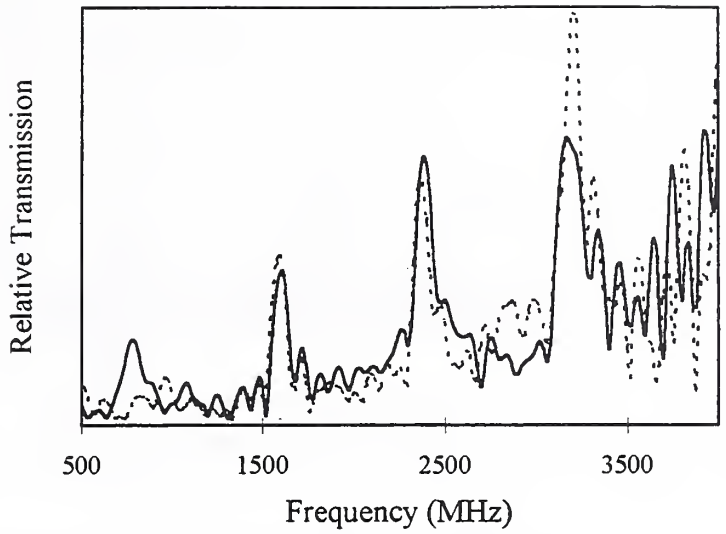

Figure 42: Pulsed transmittance data for the monopole outside the cavity. The solid line represents a half cavity length spacing, the dotted line a quarter cavity length.

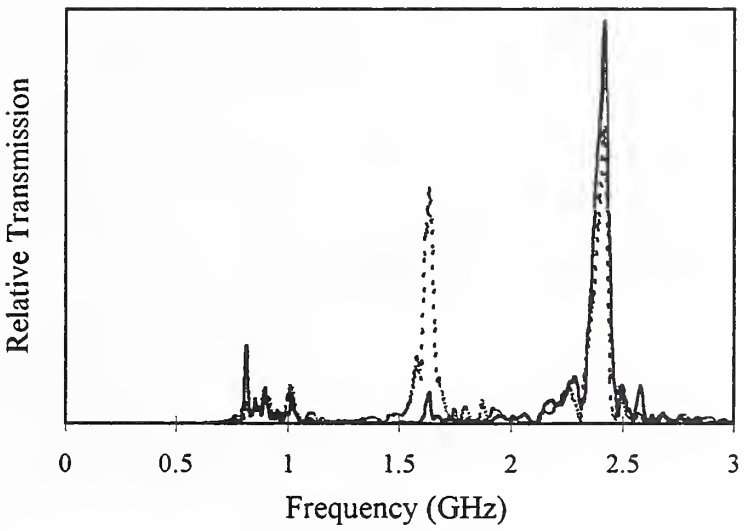

Figure 43: cw spectra for the monopole inside the cavity. The solid line is again the emission from cavity center.

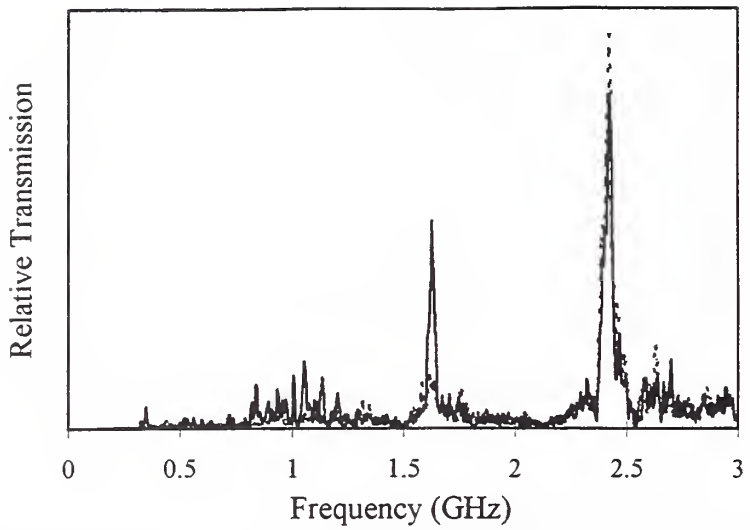

Figure 44: cw transmittance data for the monopole outside the cavity (solid line = position 4, dashed = position 3).

account for the localization sensitivity. There are some suggestions as to how the spectra in Fig. 44 might arise, but it is best to leave these for a later section (Sec. 6.3.1).

6.2.4 CW Electrical Reflection Data

Returning to the feedback question, it remains to examine the cw electrical reflection data taken for the monopole inside and outside of the cavity. For the monopole inside, Fig. 45 shows two spectra which follow closely the related transmission spectra in Fig. 43. For the cavity center position, the first harmonic is suppressed, whereas it is not in the position 2 data. These spectra are normalized to a spectrum taken with the cavity removed altogether, in order to remove the source-intensity dependence and the room effects.

This is precisely the opposite of what the feedback model called for. If a mode was inhibited due to feedback, we would have seen greater reflection intensity. Instead, the measured reflection intensity parallels the transmission intensity, which suggests that the modes seen in the reflection data are of another origin than feedback.

The external-source reflection spectra are similarly free of anything which would be consistent with the feedback mechanism, as indicated in Fig. 46. The only feature of note here is the sinusoidal oscillation in frequency. Since the source is highly coherent (3 kHz bandwidth corresponds to a coherence length of about 100 km), this oscillation is consistent with the phase of the reflected wave, again suggesting that the reflected signal measures only the magnitude of the field at the location of the antenna.

6.3 Analysis

Though the data seem to support at this point the conclusion that feedback cannot be responsible for the redistribution effects seen in the radiation from cavities of this type,

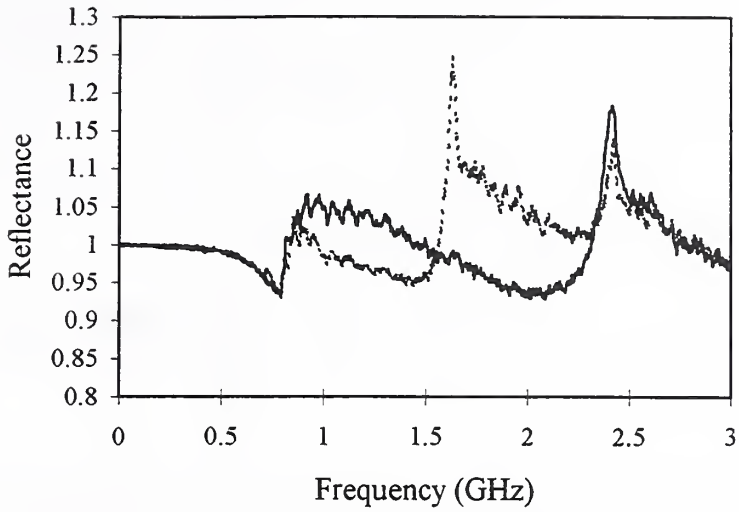

Figure 45: cw electrical reflection data for the monopole inside the cavity, at cavity center (solid line) and $l_c/4$ closer to the back mirror (dashed line).

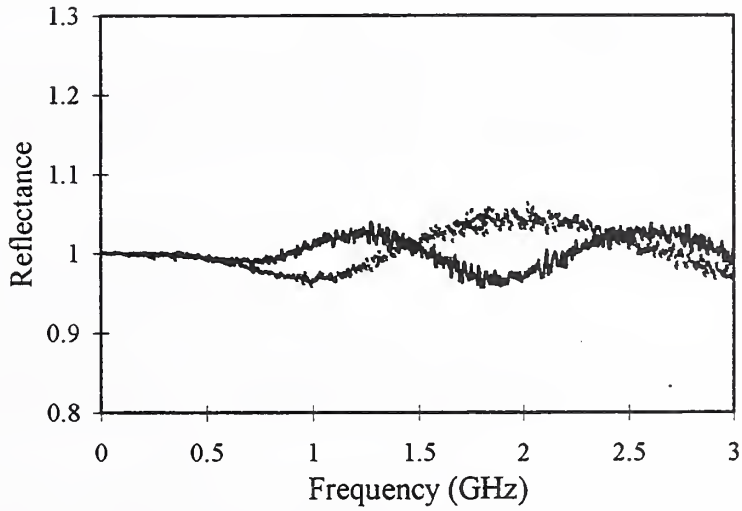

Figure 46: cw electrical reflection data for the monopole outside the cavity, at $l_c/2$ from the back mirror (solid line) and $l_c/4$ from it (dashed line).

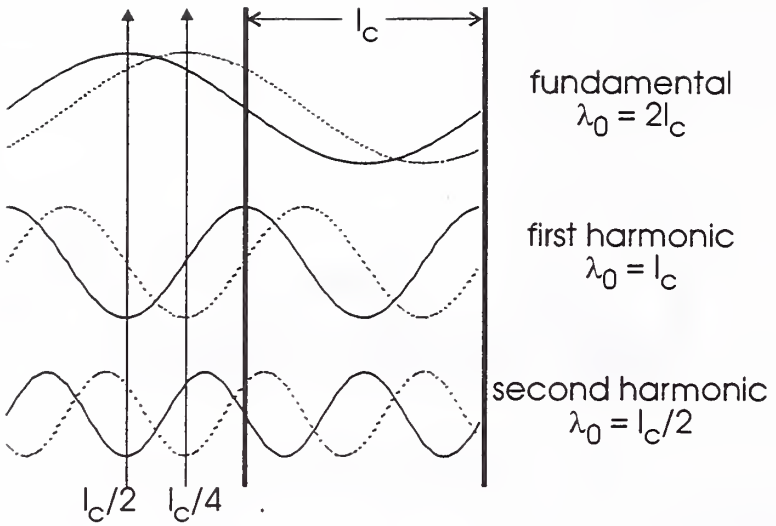

Figure 47: An illustration of the relative phase between emitter and cavity. For each of the modes (top = f_0, middle = $2f_0$, bottom = $3f_0$), the phase of the (frequency-resonant) wave as it enters the cavity changes with the position of the dipole.

there are a few inconsistencies that should be addressed first. There are in fact two: the first is the problem of localization dependence in the external-source transmission data, and the second is the discrepancies between the internal-source reflection spectra and both the external-source data and the transmission data.

6.3.1 Anomalous Localization Dependence

What is the origin of the localization dependence in Fig. 44? At first blush, it might seem that the explanation of this suppression effect lies in the coherence of the source and its proximity to the cavity. Then again, it is entirely possible that there is some kind of feedback mechanism at work.

As pictured in Fig. 47, the source itself, being relatively coherent, produces waves of very definite phase and frequency. The cavity also has a preferred phase: it is selective not only of frequencies but also of the phases of the waves entering it. Specifically, even those waves of frequency equal to one of the cavity modes will be attenuated if they do not have nulls at the mirrors. Thus, the phenomenon of Fig. 44 could be a manifestation of this well-defined relative phase between cavity and emitter.

Considering the fundamental mode (the top drawing in Fig. 47), the dipole at $l_c/2$ behind the mirror will at resonance (f_0) emit a wave whose phase satisfies all the boundary conditions (since it has a null at the first mirror), whereas the dipole at $l_c/4$ will not. For the first harmonic, the dipole at $l_c/4$ has the right phase, but the one at $l_c/2$ does not, a situation exactly the reverse of the data. For the second harmonic, $l_c/2$ should work but $l_c/4$ should not. A careful examination of this construction will reveal that the dipole's position is simply an extension of the cavity boundary conditions; there is no new constraint added.

Table 1: Table of phase relationships for the dipole outside the cavity. The entrant phase indicates whether or not the wave going into the cavity has a null at the mirror (+ = yes, − = no) and the reflected phase indicates whether the wave returning to the dipole has the same phase as the emitted wave (0 = null at dipole). A + thus indicates that the mode will be enhanced, and a − indicates that it will be suppressed. The transmission data are also listed for comparison.

Mode	Dipole Position	Entrant Phase	Reflected Phase	cw Data
f_0	$l_c/2$	+	−	+?
	$l_c/4$	−	0	−?
$2f_0$	$l_c/2$	−	+	+
	$l_c/4$	+	−	−
$3f_0$	$l_c/2$	+	−	+
	$l_c/4$	−	+	+

The resonance condition might also be that a standing wave should be set up outside the cavity. In this case, the relevant quantity is the phase of the reflected wave when it returns to the dipole position. This, too, falls short of a complete explanation of the data, as shown in Table 1. Since this is also the condition for feedback (an antinode at the dipole position for enhancement), that mechanism cannot be responsible for the data, either.

It is thus more likely that the suppression of the first harmonic in the $l_c/4$ spectrum is due to electrical coupling of the dipole to the ground plane, that is, shorting of the electrical signal. This shorting, due to induced currents in the mesh and the ground plane, is more significant in the cw experiment because the currents are also continuous. In the pulsed case, the current has much more time to dissipate between pulses. That it happens only for the antenna position closest to the cavity is also a manifestation of the time and distance required for the current to dissipate, and the fact that it happens only at lower frequencies is most likely due to the change in absorption by the mesh at different frequencies.

6.3.2 Feedback in Planar Cavities

There is some question as to whether feedback is at all significant in planar cavities. Since the mode degeneracy in the ideal Fabry-Perot etalon is one, the emitter couples to a resonant field in only one spatial direction. As Heinzen[93] has shown, increasing the mode degeneracy (as in a confocal resonator) greatly enhances the coupling of the emitter to its own radiated field.

The observations in the reflected electrical signals measured in this experiment are inconsistent with the assumption of feedback. They are in fact more consistent with re-absorption of a portion of the standing field by the dipole. The modes in Fig. 45 show clearly the frequencies where the cavity does or does not set up a large, resonant, standing field, and the modes seen in reflection exactly follow those seen in transmission. The more plausible

explanation is thus that the reflected wave is simply a measure of the field strength at the dipole position and that feedback is not occurring, at least in the dipole itself.

In this context, the sinusoidal backgrounds in the reflectance spectra (both internal and external) make a great deal of sense. In both cases, the magnitude of the field should have a weak sinusoidal frequency dependence. Recall that in Eq. 14, for the field emitted by the dipole inside the cavity, there was a cosine term in the numerator. When it is outside, as shown above, the reflected and emitted waves will interfere to create a different field magnitude, again through a sinusoidal relationship.

The discrepancy in the mode suppression of Fig. 44, the cw optical transmission spectrum, is therefore probably not due to feedback, which would depend on the relative phase of the reflected wave. Not only is there no evidence of this in the reflected signal, but the prediction of feedback is inconsistent with the data.

The last feature to be discussed is the sharp dip near the fundamental in the internal reflectance spectrum (Fig. 45). Due to its sharp character, it is tempting to conclude that this is a cavity-induced feature, perhaps a manifestation of feedback. However, this dip would correspond to an increase in transmission of the fundamental mode, which is clearly not the case in the data, and none of the models predict enhancement of the fundamental for both dipole positions (only for cavity center). Again, this inconsistency fits more comfortably into the somewhat more mundane descriptions of absorption by the mesh mirrors or electrical shorting.

In the final analysis, the purpose of this experiment has been well-served. The data presented above show that radiative redistribution is not indicative of feedback, and that the redistribution for a dipole inside a cavity is much more pronounced than for one outside the cavity.

7 Cavity Coupling in VCSELs

7.1 Multimode VCSEL Experiments

Even if feedback effects are lacking in the somewhat idealized microwave experiment, the question of what will happen in a VCSEL structure with distributed mirrors of higher reflectivity remains. As shown in Ch. 5, the resonant field in a VCSEL cavity can be large enough to cause resonant re-absorption effects such as Rabi splitting, so there is some difference between the simple Fabry-Perot structure of the microwave experiments and a real VCSEL device.

In addition, as the dipole is moved out of the cavity into the mirrors, there must also be a transition region, where the behavior slowly changes from "inside-cavity" to "outside-cavity." When it is inside the cavity, the dipole emits into cavity modes as in the normal way (described in Ch. 3); when it is fully outside the cavity, it should look like a localized dipole transmitting through (or reflecting off) an etalon, much like the transmission (reflectance) spectra of Fig. 40 (Fig. 93).

This question is not purely academic. Referring back to the proposed device of Fig. 6, the

coupled-cavity design driven by a single quantum well in an intermediate mirror, it is relevant to ask at what point a dipole in a mirror will stop coupling into cavity modes effectively. This places constraints on the design of the mirror, since the intermediate mirror cannot be thicker than twice the effective "coupling length" of the emitter (into the cavities). For the device in Fig. 5, the multimode, multi-quantum well device, there is concern with the growth accuracy needed to couple selectively into the different, closely spaced modes.

To answer these questions, four different VCSEL designs were fabricated and measured. Two had quantum wells in the cavity, the other two had quantum wells in the mirror. By comparing the surface-normal emission spectra from all four against each other and against the emission models (described in detail in App. B), we can gain some insight into how the coupling changes and whether or not the proposed devices might work.

7.1.1 Specimen Descriptions

The four specimens, as mentioned above, fall into two categories: quantum wells inside the cavity and within the mirrors. In all other respects, the four devices were of identical design. The length of the cavity was such that at least three modes could be defined within the stop band and two weaker modes could also be identified at the edges of the high-reflectance band. (In some of the actual devices, theses modes were fairly strong as later data will show.) Table 2 lists the design parameters for the first two VCSELs, with quantum wells inside the cavity. The structure CD1 called for a QW at the exact center of the cavity, whereas CD2 placed the QW 50 nm closer to the bottom mirror stack.

The difference in mode coupling between these two designs is depicted in Fig. 48, showing the three dominant modes at 782, 798, and 815 nm. At cavity center (roughly 4.55 μm in the graphs), the first and third modes have nodes, and the second has an antinode. Only fifty nanometers away from this point, however, the opposite situation pertains: the first and third modes are at maximum, and the second is at a null. By moving the QW just 50 nm in the cavity, it should be possible to completely reverse the coupling into the various modes.

The design parameters for the VCSELs with the QWs outside the cavity, in the top mirror, are shown in Table 3. The choice of the sixth mirror pair was determined by calculating the effective cavity length (by a $1/e$ method). This placement thus allows both quantum wells to be outside the effective cavity length.

In this case, the QW was moved by the thickness of one mirror layer, 59.68 nm. The phase relationship between the standing fields of the three modes near the position of the QW in the mirror, shown in Fig. 49, does not show the phase shifts between modes evident in Fig. 48. In fact, Fig. 49 suggests that all the modes are nearly in phase at this point in the mirror, which would mean that none of them couple differently when the QW is moved. However, there are a few other factors to take into account.

These fields represent one wavelength out of a small continuum which make up the actual mode. Especially in the mirror regions, the field strength prediction can vary dramatically with wavelength, and it is difficult to exactly determine the resonance wavelength (even in the model). In addition, small variations in the construction parameters can also shift the fields relative to each other. Since the standing field is set up in the mirrors, these

Table 2: Design parameters for the multimode VCSELs with QWs inside the cavity spacer. The last DBR pair in the top mirror is adjusted to include the optical thickness of the cap layer. (mly = monolayers.)

Layer	Material	CD1 Thickness (nm)	CD1 # pairs	CD2 Thickness (nm)	CD2 # pairs
Buffer	GaAs	500.00	1	500.00	1
DBR B1	AlAs	65.51	22	65.51	22
DBR B2	$Al_{0.3}Ga_{0.7}As$	58.21	22	58.21	22
DBR B3 (phase slip)	AlAs	65.51	1	65.51	1
Cavity Spacer 1	$Al_{0.3}Ga_{0.7}As$	1862.64	1	1812.64	1
QW	GaAs	5.94 (21 mly)	1	5.37 (19 mly)	1
Cavity Spacer 2	$Al_{0.3}Ga_{0.7}As$	1862.64	1	1912.64	1
DBR T1	AlAs	65.51	21	65.51	21
DBR T2	$Al_{0.3}Ga_{0.7}As$	58.21	21	58.21	21
DBR T1a	AlAs	65.51	1	65.51	1
DBR T2a	$Al_{0.3}Ga_{0.7}As$	42.49	1	42.49	1
Cap	GaAs	15.16	1	15.16	1

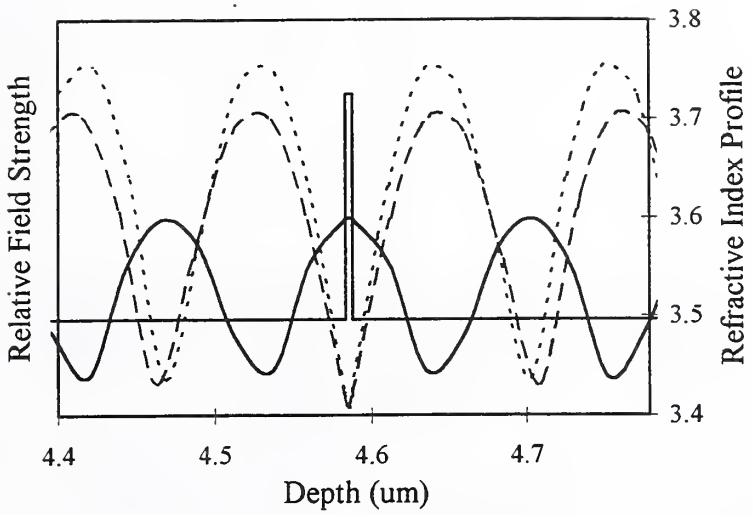

Figure 48: Mode fields of the multimode VCSELs, near the center of the cavity spacer where the QWs were placed. From top to bottom, the projected modes are in order of wavelength: approximately 782 nm (dotted line), 798 nm (solid line), and 815 nm (dashed line). The refractive index profile for the QW at cavity center (CD1) is also shown (solid line) for reference.

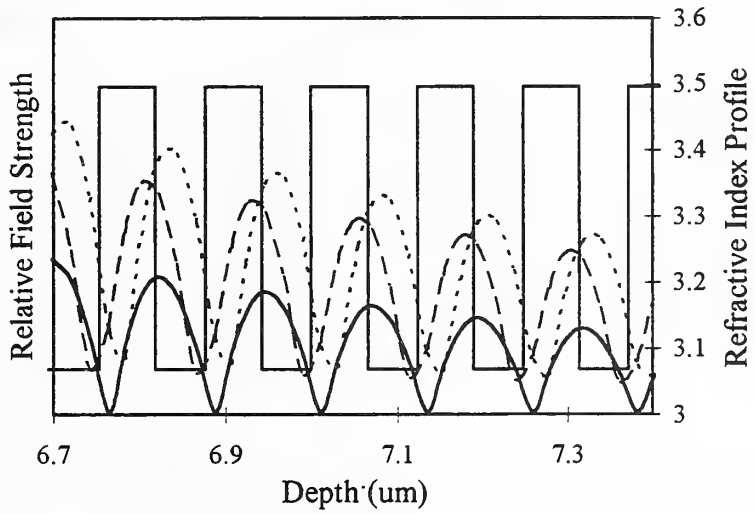

Figure 49: Mode fields of the multimode VCSELs, near the sixth mirror pair where the QWs were placed.

Table 3: Design parameters for the multimode VCSELs with QWs inside the cavity spacer. The last DBR pair in the top mirror is adjusted to include the optical thickness of the cap layer. Top DBR layer 3 is also adjusted for the optical thickness of the quantum well.

Layer	Material	MD1 Thickness (nm)	MD1 # pairs	MD2 Thickness (nm)	MD2 # pairs
Buffer	GaAs	500.00	1	500.00	1
DBR B1	AlAs	65.51	22	65.51	22
DBR B2	$Al_{0.3}Ga_{0.7}As$	58.21	22	58.21	22
DBR B3	AlAs	65.51	1	65.51	1
Cavity Spacer	$Al_{0.3}Ga_{0.7}As$	3725.28	1	3725.28	1
DBR T1	AlAs	65.51	5	65.51	5
DBR T2	$Al_{0.3}Ga_{0.7}As$	58.21	5	58.21	5
DBR T3	AlAs	—	—	59.68	1
QW	GaAs	5.94 (21 mly) (21 mly)	1	5.94 (21 mly) (21 mly)	1
DBR T3	AlAs	59.68	1	—	—
DBR T4	$Al_{0.3}Ga_{0.7}As$	58.21	1	58.21	1
DBR T5	AlAs	65.51	13	65.51	13
DBR T6	$Al_{0.3}Ga_{0.7}As$	58.21	13	58.21	13
DBR T5a	AlAs	65.51	1	65.51	1
DBR T6a	$Al_{0.3}Ga_{0.7}As$	42.49	1	42.49	1
Cap	GaAs	15.16	1	15.16	1

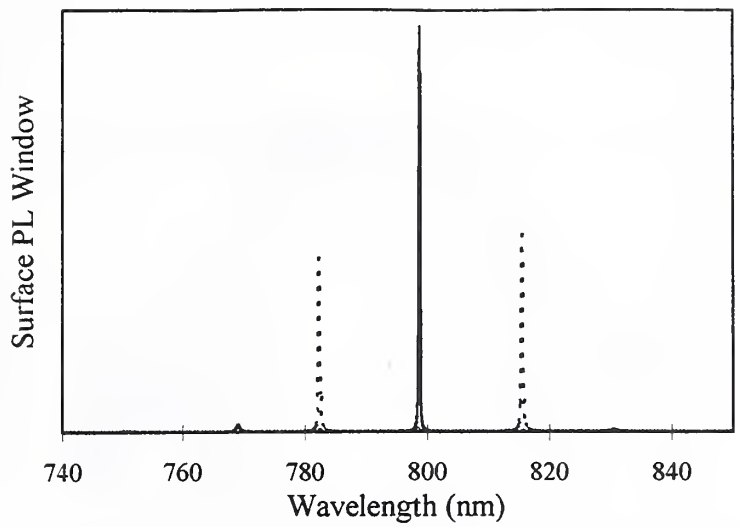

Figure 50: Emission models for the multimode VCSELs with quantum wells inside the cavity. The solid line is for the VCSEL with the QW at the center of the cavity (CD1), the dashed for the QW 50 nm off center (CD2).

uncertainties have more impact in the mirror regions than in the cavity. In short, there is reason to believe that the field predictions in the mirrors are less reliable than their cavity counterparts, and this illustrates the fact that estimating mode coupling from predicted field distributions should not be expected to yield highly accurate results.

We therefore expect that the QWs at different positions in the mirrors could couple into the cavity modes differently, if they couple into the cavity modes at all.

7.1.2 Emission Models

The emission spectrum for an arbitrary VCSEL device can be predicted using the technique of Sec. 3.3.1, described in further detail in Appendix B. Based on the descriptions given above, and using cross-sectional data consistent with the quantum wells as designed, the predictions for the multimode VCSEL emission spectra are as shown in Figs. 50 and 51.

As indicated by the field distributions above, the emission windows for the VCSELs with QWs inside the cavity spacer show a dramatic shift in mode coupling (see Fig. 50). The CD1 device should couple more strongly into the mode at roughly 798 nm, whereas the CD2 device should couple into the other two modes at 782 and 815 nm. This is exactly the expectation arrived at from the analysis of the fields.

The external-QW devices, on the other hand, show a less predictable response. The QW at the fifth high/low index interface couples into the lowest mode (782 nm) with greatest intensity, but the QW at the sixth low/high interface couples into the side mode at about 768 nm the strongest. In each case, the prediction does not exclude any of the modes to the same degree as in the internal-QW case.

However, as explained in the discussion of the field profiles, this prediction can vary quite a bit with small variations in the construction parameters. It is hardly possible to expect a

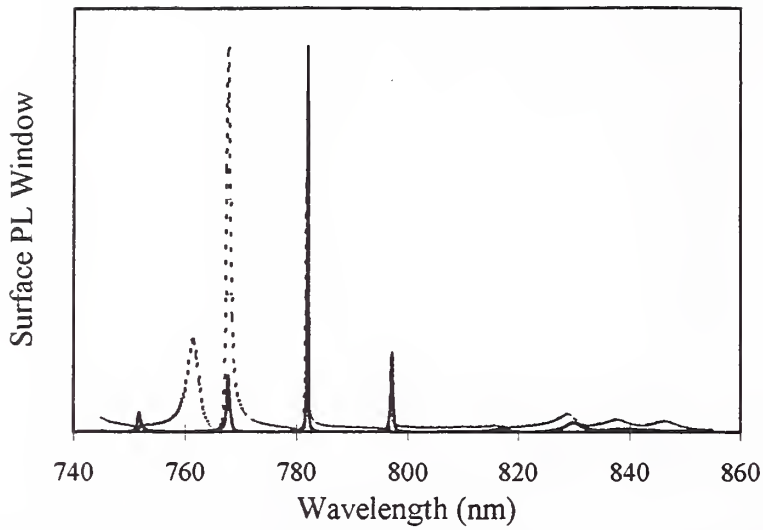

Figure 51: Emission models for the multimode VCSELs with quantum wells outside the cavity. The solid line is for the VCSEL with the QW at the fifth high/low index interface (MD1), the dashed for the QW one mirror layer above that (MD2).

good fit in this case, where the coupling is very sensitive to small variations in the standing fields, without knowing the systematic variations in the real structure. Thus the first step in improving the emission spectra predictions for the structures in this study is to generate a match to their reflectance signatures in order to determine the construction parameters more accurately.

7.1.3 Reflectance Metrology

The reflectance data for the four structures, along with the best-fit model (for the layer thicknesses; see App. B), are shown in Figs. 52 through 55.

The parameters used to generate these fits are given in Tables 4 and 5. As is evident from the fit parameters, these structures all exhibit the slight thickness gradient (resulting in mirror mismatch; see Appendix B) which is characteristic of MBE-grown material.

Though the fit is indeed good near the high reflectance band, there is a slight shift in the periodicity of the interference fringes near the long and short wavelength ends of the spectrum. This can be attributed to either dispersive changes in optical thickness (implying a refractive index inaccuracy) or to higher-order effects (beyond mirror mismatch) in the thickness variation. In this case, however, the fit in the region of interest is quite good and should suffice for accurate predictions of emission spectra.

7.2 Multimode VCSEL Results

The measured emission spectra for the two internal-QW structures are shown in Figs. 56 and 57. Also shown are the predicted emission spectra based on the corrected thicknesses determined from the reflectance models, as described above. The predicted emission spectra

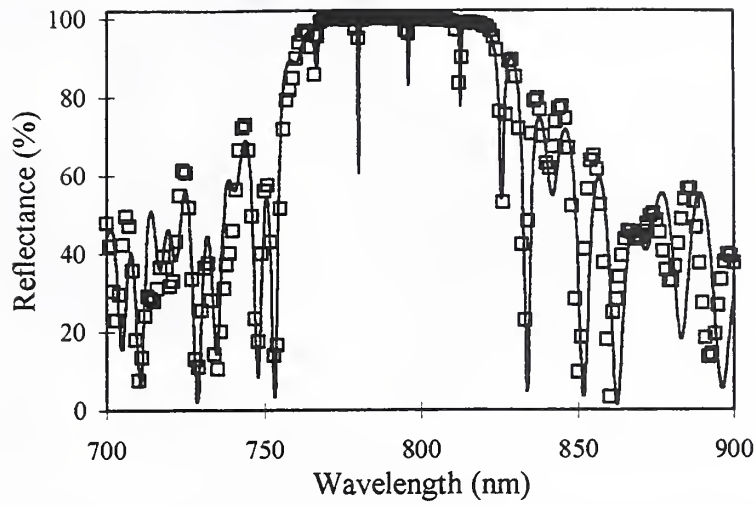

Figure 52: Reflectance spectrum and model of the first internal-QW VCSEL device, CD1. The open squares are the data; the solid line is the best-fit numerical match.

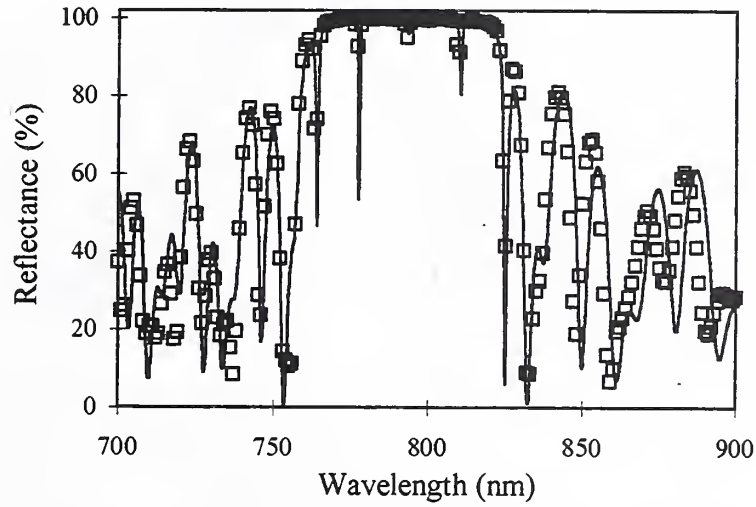

Figure 53: Reflectance spectrum and model of the second internal-QW VCSEL device, CD2. The open squares are the data; the solid line is the best fit numerical match.

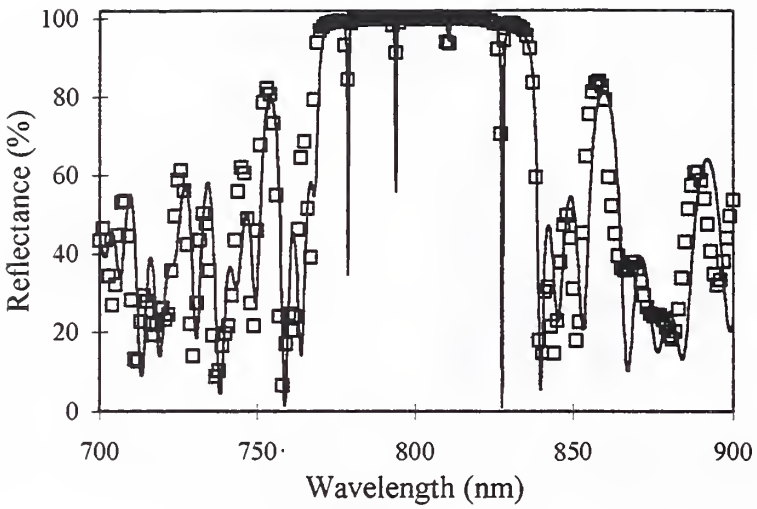

Figure 54: Reflectance spectrum and model of the first external-QW VCSEL device, MD1. The open squares are the data; the solid line is the best fit numerical match.

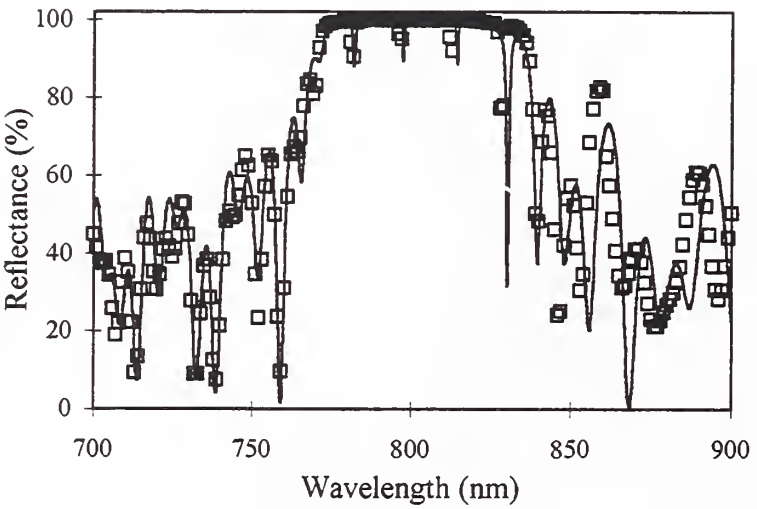

Figure 55: Reflectance spectrum and model of the second external-QW VCSEL device, MD2. The open squares are the data; the solid line is the best fit numerical match.

Table 4: Modeling parameters for the multimode VCSELs with QWs inside the cavity spacer, used to generate the fits described in the text.

Layer	Material	CD1 Thickness (nm)	CD1 # pairs	CD2 Thickness (nm)	CD2 # pairs
DBR B1	AlAs	65.68	22	65.19	22
DBR B2	$Al_{0.3}Ga_{0.7}As$	58.31	22	57.88	22
DBR B3	AlAs	65.68	1	65.19	1
Cavity Spacer	$Al_{0.3}Ga_{0.7}As$	3717.47	1	3700.96	1
DBR T1	AlAs	64.58	21	64.80	21
DBR T2	$Al_{0.3}Ga_{0.7}As$	57.33	21	57.54	21
DBR T1a	AlAs	64.45	1	64.67	1
DBR T2a	$Al_{0.3}Ga_{0.7}As$	42.15	1	42.24	1
Cap	GaAs	15.04	1	15.07	1

Table 5: Modeling parameters for the multimode VCSELs with QWs inside the cavity spacer.

Layer	Material	MD1 Thickness (nm)	MD1 # pairs	MD2 Thickness (nm)	MD2 # pairs
DBR B1	AlAs	66.07	22	66.40	22
DBR B2	$Al_{0.3}Ga_{0.7}As$	58.74	22	59.03	22
DBR B3	AlAs	66.07	1	66.40	1
Cavity Spacer	$Al_{0.3}Ga_{0.7}As$	3807.60	1	3833.84	1
DBR T1	AlAs	65.67	5	65.34	5
DBR T2	$Al_{0.3}Ga_{0.7}As$	58.38	5	58.09	5
DBR T3	AlAs	—	—	59.20	1
DBR T3	AlAs	59.50	1	—	—
DBR T4	$Al_{0.3}Ga_{0.7}As$	58.38	1	58.09	1
DBR T5	AlAs	65.67	13	65.34	13
DBR T6	$Al_{0.3}Ga_{0.7}As$	58.38	13	58.09	13
DBR T5a	AlAs	65.67	1	65.21	1
DBR T6a	$Al_{0.3}Ga_{0.7}As$	42.36	1	42.06	1
Cap	GaAs	15.11	1	15.01	1

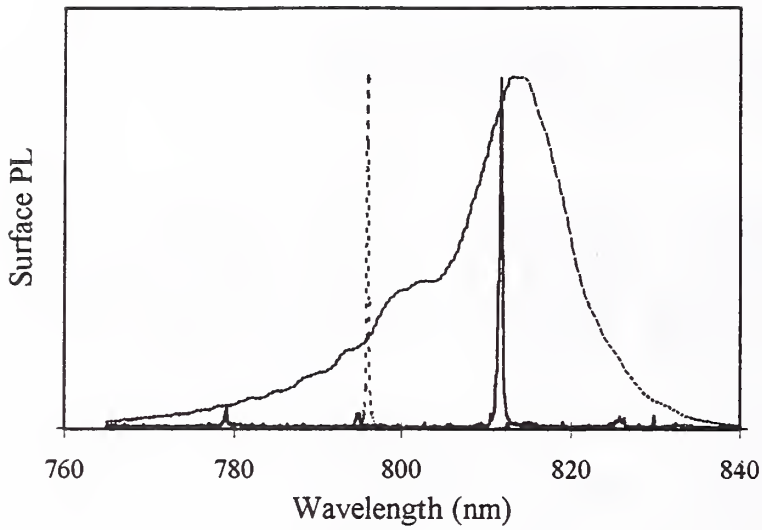

Figure 56: Emission spectra for the VCSEL with a QW in the center of its cavity. The solid line is the measured surface-normal emission, the dashed line is the cross-sectional spectrum, and the dotted line is the prediction based on the reflectance fit and the XPL data.

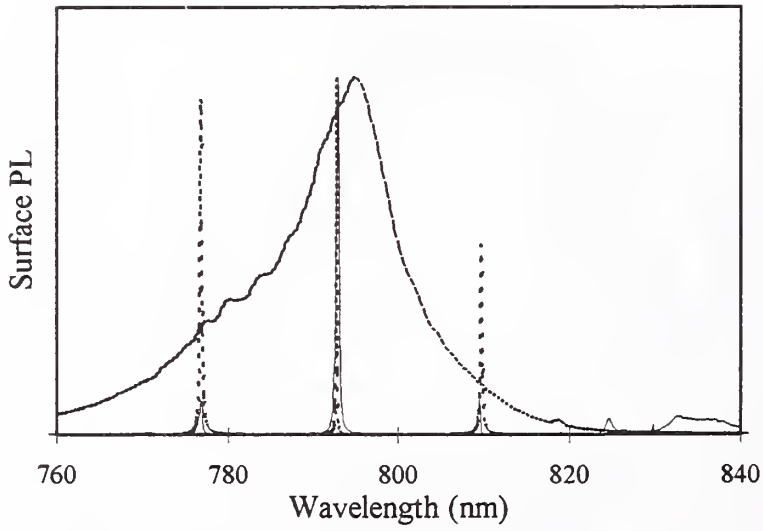

Figure 57: Emission spectra for the VCSEL with the QW 50 nm off the center of the cavity: NPL (solid line), XPL (dashed line), and predicted NPL spectrum (dotted line).

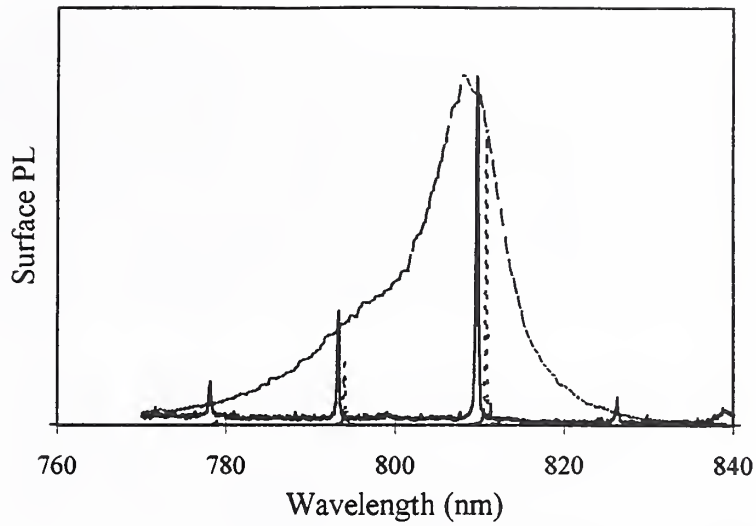

Figure 58: Emission spectra for the external-QW VCSEL (QW at fifth H/L interface).

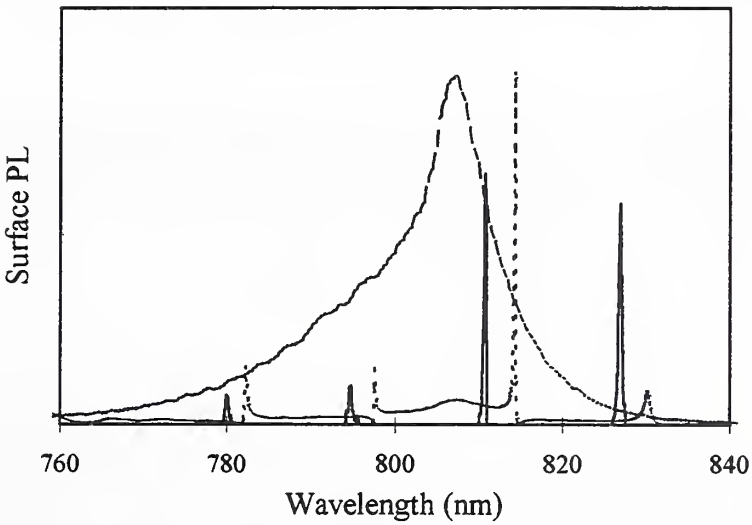

Figure 59: Emission spectra for the VCSEL with a QW at the sixth L/H interface.

have been adjusted to include the QW response, as measured by XPL. In each graph, the XPL spectrum has been included for reference.

Figure 56, for the QW in the center of the cavity, is qualitatively what was expected from the predictions: there is only one strong mode. Unfortunately, the mode that emits the strongest (#3 at about 815 nm) is not the mode which was predicted (#2 at about 798 nm). Similarly, the model for the QW offset from the center predicts that the second mode should be the strongest, but also predicts a much stronger response from the first and third modes.

In contrast, the match between predictions and data for the external-QW structures is much better than for the internal-QWs. Figures 58 and 59 show the measured surface-normal emission, the predicted emission and the measured side emission for the two VCSEL structures with QWs in the mirrors.

For the MD1 structure, the measured mode wavelengths are slightly shorter than pre-

dicted, but the relative intensities are more accurate than Figs. 56 and 57. This trend is continued in the spectra for the MD2 structure, where the mode wavelength shift has increased, but the relative intensity prediction has remained accurate. For all of the VCSEL structures, the intensity ratio between the different modes remains constant and reproducible at varying power levels. Since the substrate rotation was stopped for 15 min during each growth (at the end of the cavity spacer), the uniformity is not comparable to a constantly rotated wafer. However, within a small region, the measurements were roughly constant; the modes over approximately 0.5 mm square section might shift as much as 0.2 nm in either direction.

The discrepancies between the mode wavelengths in Figs. 58 and 59 (the design models) and Fig. 51 (the actual external-QW structures) can be attributed to imprecision in the growth, as evidenced in the reflection data (Figs. 54 and 55). However, the shift between the predicted and measured emission spectra for the external-QW structures (Figs. 58 and 59) is beyond the uncertainty in the measurement.

7.3 Analysis

One goal of the VCSEL experiments was to determine the feasibility of two devices proposed at the beginning of this work. As the answers to those questions include much of the physics and metrology central to the problem and to this work, it suffices here to frame the response in terms of the devices in Figs. 5 and 6.

7.3.1 The Three-Color VCSEL

This device depends most strongly on lithographic control and the control of coupling QWs in the cavity into the different modes. As is evident from the device schematic of Fig. 5c and the design of the CD1 and CD2 structures above, the contact mesas must be accurate within 100 nm or so, which is near the limit of some advanced process techniques such as reactive ion beam etching. In any event, the actual fabrication of this device is well beyond the scope of this work, so we are left with the consideration of how well the mode coupling can be controlled.

Of particular concern is the aberration in the coupling predictions for the two internal-QW devices. There are several possible explanations for the error, but perhaps the most significant are: (1) the model is inaccurate; (2) there is another phenomenon at work in these structures (CD1 and CD2) only; and (3) the QWs are not at the expected locations due to inaccuracy in the growth.

The first possibility is that the model is inaccurate. This explanation suggests that all the emission spectra should be inaccurate, but this is not the case. Indeed, as shown in Appendix B, the model does predict emission spectra with a fair degree of accuracy. However, it bears the most investigation.

Because the model is very sensitive to variations in construction parameters, it is logical to try to gauge that sensitivity. To start with, the mismatch of the mirrors could be expected to have an effect on the emission model. However, removing this mismatch does not have

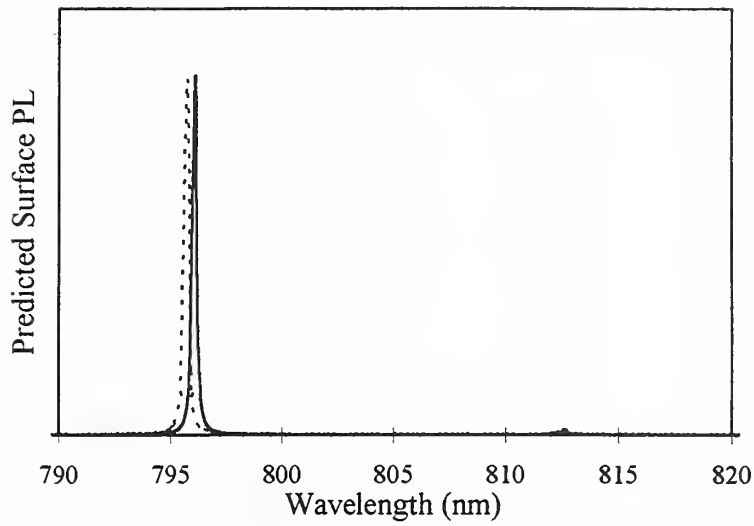

Figure 60: The effect of mirror mismatch on the emission spectrum of the CD1 device. The solid line is the model which uses the thicknesses listed in the text, the dashed line uses the same parameters, with the mirror thicknesses identical.

the desired effect on the emission spectrum, as shown in Fig. 60, where the original model is compared with one that uses constant thicknesses (64.97 nm/AlAs and 57.68 nm/AlGaAs) for both top and bottom mirrors. The wavelength of the mode shifts slightly, but the relative intensities of the modes remain the same.

Though the model of Fig. 18 suggested that there should be little difference in the reflectance spectra for 0° and 6° collection, it is worthwhile to examine the corresponding effect on the emission. Figure 61 shows that, as in the case of reflectance, there is little effect from a low-NA objective.

There is also the possibility of inaccuracy in the index models used; Appendix B discusses at length this aspect which can have a sizeable impact on the emission spectrum. However, this type of error simply shifts the entire spectrum, whereas the spectra above indicate that the positioning of the modes in wavelength space is correct, but that the coupling into the various modes is not.

The second possibility, another physical phenomenon at work, is also unlikely. The length of the cavity spacers precludes any sort of feedback effect, which would not explain the CD1 discrepancy in any event. Since there is only one QW in each structure, there cannot be any kind of dipole-dipole coupling at work. Heating of the QW by the pump is also ruled out due to the stability of the spectra with pump power and the fact that mode wavelengths do not shift (heating also does not explain the CD2 differences). Index shifts due to absorption of the pump by the mirrors are also not significant for the same reason.

This leaves the idea that the QWs or the cavity spacers were misgrown, which could not be directly verified by transmission electron microscopy or a similar analysis technique. However, this implies that the MBE process used could not be controlled within 50 nm, which is inconsistent with a large body of other data on the machine. Run sheets for the CD1 and CD2 structures indicate that they were grown according to specifications. Though

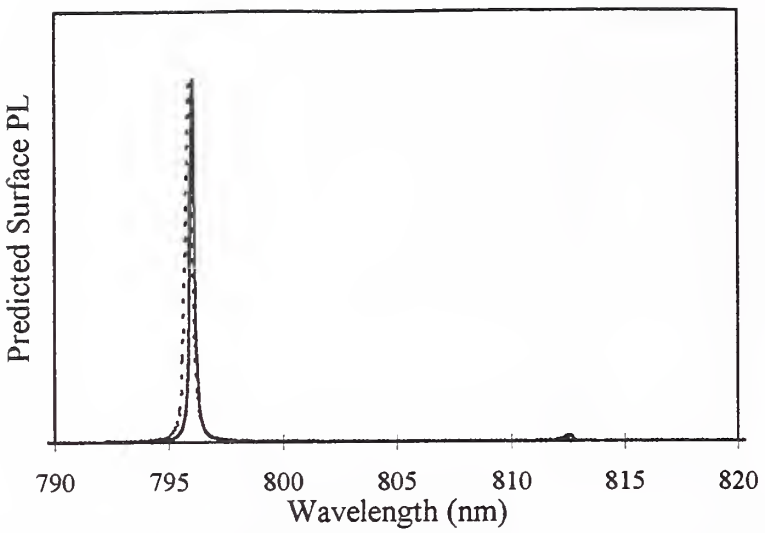

Figure 61: The effect of the 6° collection angle of the objective used to take the emission spectra. The solid line is for 0°; the dashed for 6°.

a growth problem could easily explain the discrepancies between the data and model, it is unlikely at best. Yet the most probable causes of the differences are inaccurate growth or inaccurate modeling, and in this case, there is more evidence to support the accuracy of the model.

At the end of the day, the important point is that the coupling into the various modes from QWs inside the cavity spacer can be controlled, even if that coupling cannot be predicted accurately. Such a device as the one pictured in Fig. 5 is thus feasible from a physical standpoint.

7.3.2 The Two-Cavity VCSEL

In the case of the two-cavity device, the salient concern is whether or not the QWs in the intermediate mirror still couple into the cavity modes as they would if they were inside the cavity spacer. From the fact that the spectra of Figs. 58 and 59 look more like emission spectra than reflection spectra (as in Fig. 93), the coupling is obviously more cavity-like than not.

There is, however, another question to ponder. Specifically, the spectra of Figs. 58 and 59 show a larger wavelength shift of the modes than do Figs. 56 and 57. It is possible that there could be some sort of mode pulling effect in the mirrors which does not exist in the cavity, but a short comparison can resolve this.

Table 6 lists the mode frequencies for all the devices in this study, as determined by reflectance measurements (1 nm/0.01 nm interval), reflectance modeling (0.5 nm interval), PL measurements (0.1 nm interval), and PL modeling (0.1 nm interval). This comparison makes it clear that none of the wavelength discrepancies are prohibitive in terms of device performance: all are less than about 1 nm. Also, the reflection and emission models are consistent in their predictions of the mode positions since they agree in all cases to within

Table 6: Mode wavelengths of the four devices discussed in the text. The first column also lists the technique by which they were determined: RS = reflectance spectroscopy, HRRS = high-resolution (0.01 nm) reflectance spectroscopy, RM = reflectance modeling, PL = surface-normal photoluminescence, PM = luminescence modeling.

Structure/ Method	Mode 0 (766 nm)	Mode 1 (782 nm)	Mode 2 (798 nm)	Mode 3 (815 nm)	Mode 4 (827 nm)
CD1 – RS	766	780	796	812	—
– RM	765.5	780	796	812.5	—
– PL	766.1	779.2	794.9	811.7	—
– PM	766.6	779.8	796.1	812.6	—
CD2 – RS	763	777	794	810	—
– RM	764	777.5	793.5	810.5	—
– PL	—	776.8	792.8	809.4	—
– PM	—	776.9	792.8	809.4	—
MD1 – RS	—	779	794	811	827
– HRRS	—	777.78	792.92	809.35	825.92
– RM	—	779	794	811	827.5
– PL	—	778.1	793.3	809.7	826.3
– PM	—	779.1	794.3	810.9	827.7
MD2 – RS	—	782	797	813	828
– RM	—	782	797.5	814	830
– PL	—	780	794.8	810.8	826.9
– PM	—	782.4	797.8	814.5	830.2

the accuracy of the reflectance model, 0.5 nm. In addition, the main disagreement seems to be between the NPL data and the reflectance data (or either of the models). The high-resolution data taken on MD1 at exactly the same location as the NPL spectra reveal that the shift in the external-QW emission spectra is most likely due to variations across the wafer.

Again, none of these limitations or inaccuracies are sufficient to prohibit the operation of the device. Furthermore, the differences in the NPL spectra of Figs. 58 and 59, while not as pronounced as those between the internal-QW structures, are sizable enough and reproducible enough to allow control of mode coupling even when the QW is placed in a mirror, outside the effective cavity length of the device.

8 Conclusion

8.1 Contributions

At the outset of this document, a list was presented summarizing the contributions of this work. It therefore seems appropriate to re-examine those contributions in light of the data and analyses that have been discussed in the body of this work.

1. *First documentation and demonstration of a novel measurement technique for semiconductor heterostructures — cross-sectional photoluminescence — and first measurement of side emission from VCSELs.*

2. *First application of XPL and XPL depth-profiling to the metrology of buried-layer semiconductor structures.*

   This technique was discussed at length in Ch. 4, including many applications to and metrology of VCSELs. Further applications are discussed in Appendix A. All of the VCSEL experiments in this work, from the emitter coupling study of Ch. 5 to the mode coupling experiments in VCSELs of Ch. 7, have relied heavily on this technique. For the first publication of a detailed study of this measurement method, the reader is advised to consult to Ref. [10].

3. *First extension of conventional multilayer modeling techniques to the problem of light emission inside a multilayer resonator.*

   This modeling, which is described fully in Appendix B, has also been used throughout the work, and to great extent in Ch. 7. This work has shown (and shows further in Appendix B) the limitations and capabilities of this model in predicting the emission spectrum from a VCSEL device.

4. *First observation of cavity-induced effects on the side emission from a quantum well in a VCSEL cavity.*

5. *Assessment of side emission as a tool for probing cavity coupling effects in VCSELs.*

   The spectra of Ch. 5 demonstrated that excitons farther inside the cavity than those near an edge facet exhibited mode splitting which were best explained by coupling of emitter and cavity modes. Numerical results were obtained which agreed with the predictions of a quantum-mechanical model of Rabi oscillation. Beyond this, the experiment demonstrated the fact that the side emission measurement (XPL) can discern changes to the scalar properties of excitons in VCSEL structures simply by changing the pump orientation. In the context of Rabi splitting, this shows that the observed mode splitting is an actual change to the emitter energy configuration, rather than a filtering effect which is dependent on the direction of emission. The omnidirectional nature of this change highlights the fact that the linear dispersion approach to mode splitting and the coupled-oscillator energy perturbation approach (in this work taken quantum-mechanically) describe two distinct effects, rather than just different views of the same effect.

6. *First comparison of pulsed (no-feedback) and continuous-wave (feedback) emitters in a plane-parallel resonator.*

   The microwave experiments of Ch. 6 were designed to probe exactly this effect. The results of these experiments showed that changes in the emission pattern of a dipole in a cavity do not perforce indicate feedback at work. It is erroneous to equate intensity modification with decay rate modification, as these data have clearly shown. The comparison of the two cases — pulsed and cw — shows that even when the emitter is decoupled from its own radiation, the energy redistribution for an emitter inside a cavity is much stronger than when it is outside.

7. *First experimental test of coupling of quantum wells in DBRs to cavity modes.*

   This was the subject of Ch. 7, which showed that this coupling was very sensitive to QW (dipole) positioning, both inside the cavity and in the DBR mirror, outside the effective cavity length. The control of this effect has ramifications for VCSEL devices which could effect important areas of technology such as wavelength division multiplexing.

8.2 General

We believe that this work has indeed influenced the three areas of study which it set out to explore: metrology, technology, and basic science. In the area of VCSEL metrology, we have demonstrated a new technique that yields valuable information about properties of the structure which are important to the ultimate device performance, such as the coupling of QW emission into the cavity modes. This technique and the modeling used with it are easily extensible to in-situ application, so that growth parameters can be adjusted in real time to create a higher yield of working devices.

In the technology aspect, this Technical Note has shown that it is possible to design less conventional VCSEL structures, such as coupled cavities being driven by a single QW, and expect them to work. Much of the field to this point has remained focused on the short-cavity regime, but this work shows that there are possibilities in multimode devices which have not fully been explored at this point. These possibilities could present a sizeable boon to applications such as long-haul communications, optical data storage, and optical computing.

Most of all, this Technical Note has demonstrated that apparent spontaneous emission modification in VCSELs must be examined carefully. There are two distinct types of coupling at work in these structures and their manifestations are often very similar. This is the first work to clearly delineate these effects and show that not all short-cavity VCSEL behavior is due to emitter-cavity coupling. This is not a limitation or a negation, but a liberation: It may not be neccesary to achieve emitter-cavity coupling to induce some of the desired effects such as thresholdless lasing. If the existence, mechanisms, and regimes of the coupling phenomena at work are known, then it becomes that much easier to harness them.

References

[1] Raja, M.Y.A.; Brueck, S.R.J.; Osinski, M.; Schaus, C.F.; McInerney, J.G.; Brennan, T.M.; and Hammons, B.E. Appl. Phys. Lett. 53: 1678 1988.

[2] Corzine, S.W.; Geels, R.S.; Yan, R.H.; Scott, J.W.; Coldren, L.A.; and Gourley, P.L. Boston 1988. Lasers and Electro-Optics Society.

[3] Raja, M. Y.A.; Brueck, S. R.J.; Scully, M.O.; and Lee, C. Phys. Rev. A 44: 4599 1991.

[4] Mukherjee, A.; Mahbobzadeh, M.; Schaus, C.F.; and Brueck, S.R.J. IEEE Photon. Tech. Lett. 2: 857 1990.

[5] Stanley, R.P.; Houdré, R.; Oesterle, U.; Ilegems, M.; and Weisbuch, C. Appl. Phys. Lett. 65: 2093 1994.

[6] Yamamoto, Y.; Machida, S.; Igeta, K.; and Horikoshi, Y. *Coherence and Quantum Optics VI* page 1249. Plenum Press New York 1990.

[7] DeMartini, F.; Marrocco, M.; Mataloni, P.; Murra, D.; and Loudon, R. J. Opt. Soc. Am. B 10: 360 1993.

[8] Huffaker, D.L.; Deppe, D.G.; Kumar, K.; and Rogers, T.J. Appl. Phys. Lett. 65: 97 1994.

[9] Yablonovitch, E. Phys. Rev. Lett. 58: 2059 1987.

[10] Schaafsma, D.T. and Christensen, D.H. J. Appl. Phys. 78: 694 1995.

[11] Seeley, F.B.; Alexander, J.E.; Connaster, R.W.; Conway, J.S.; and Dowling, J.P. Am. J. Phys. 61: 545 1993.

[12] Fabry, C. and Perot, A. Ann. Chim. Phys. 16: 115 1899.

[13] Blodgett, K.B. and Langmuir, I. Phys. Rev. 51: 964 1938.

[14] Stratton, J.A. *Electromagnetic Theory.* McGraw Hill New York 1941.

[15] Born, M. *Optik.* Julius Springer Berlin 1933.

[16] Vossen, J.L. and Kern, W. *Thin Film Processes.* Academic Press New York 1978. Gives a good overview of all the coating technologies; references are given to historical developments.

[17] Blodgett, K.B. Phys. Rev. 57: 921 1940.

[18] Mooney, R.L. J. Opt. Soc. Am. 35: 574 1945.

[19] Caballero, D.L. J. Opt. Soc. Am. 37: 176 1947.

[20] Dufour, C. and Herpin, A. Rev. Opt. 32: 321 1953.

[21] Epstein, L.I. J. Opt. Soc. Am. 42: 806 1952.

[22] Crook, A.W. J. Opt. Soc. Am. 38(11): 954 1948.

[23] Weinstein, W. J. Opt. Soc. Am. 37: 576 1947.

[24] Abelès, F. Ann. d Physique 5: 611 1950.

[25] Dobrowolski, J.A. Appl. Opt. 4: 937 1965.

[26] Sossi, L. Eesti NSV Tead. Akad. Toim. Fuus. Mat. 23: 229 1974.

[27] Heavens, O.S. and Liddell, H.M. Opt. Acta 15: 129 1968.

[28] van der Laan, C.J. and Frankena, H.J. Appl. Opt. 17: 538 1978.

[29] Bloom, A.L. Appl. Opt. 20: 66 1981.

[30] Wild, W.J. and Buhay, H. Opt. Lett. 11: 745 1986.

[31] Dobrowolski, J.A. and Kemp, R.A. Appl. Opt. 31: 3807 1992.

[32] Afromowitz, M.A. Sol. St. Comm. 15: 59 1974.

[33] Adachi, S. J. Appl. Phys. 66: 6030 1989.

[34] Jensen, B. and Torabi, A. IEEE J. Quant. Elec. QE-19: 877 1983.

[35] Snyder, P.G.; Woollam, J.A.; Alterovitz, S.A.; and Johs, B. J. Appl. Phys. 68: 5925 1990.

[36] Jenkins, D.W. J. Appl. Phys. 68: 1848 1990.

[37] Terry, Jr., F.L. J. Appl. Phys. 70: 409 1991. The form of the dielectric constant given by Eq.(56) is slightly different than that given in this reference: a factor of 1 has been added to make the model fit the data as reported in Terry's paper. (It is most likely that this was simply an omission, since the fits match only with the addition.)

[38] Marple, D.T.F. J. Appl. Phys. 35: 1241 1964.

[39] Casey, Jr., H.C.; Sell, D.D.; and Panish, M.B. Appl. Phys. Lett. 24: 63 1974.

[40] Sell, D.D.; Casey, Jr., H.C.; and Wecht, K.W. J. Appl. Phys. 45: 2650 1974.

[41] Yao, H.; Snyder, P.G.; and Woollam, J.A. J. Appl. Phys. 70: 3261 1991.

[42] Aspnes, D.E.; Kelso, S.M.; Logan, R.A.; and Bhat, R. J. Appl. Phys. 60: 754 1986.

[43] Reynolds, D.C.; Bajaj, K.K.; Litton, C.W.; Peters, G.; Yu, P.W.; and Parsons, J.D. J. Appl. Phys. 61: 342 1986.

[44] Casey, H.C. and Panish, M.B. *Heterostructure Lasers.* Academic Press San Diego 1978.

[45] Keuch, T.F.; Wolford, D.J.; Potemski, R.; Bradley, J.A.; Kelleher, K.H.; Yan, D.; Farrell, J.P.; Lesser, P.M.S.; and Pollak, F.H. Appl. Phys. Lett. 51: 505 1987.

[46] Bosio, C.; Staehli, J.L.; Guzzi, M.; Burri, G.; and Logan, R.A. Phys. Rev. B 38: 3263 1988.

[47] Lautenschlager, P.; Garriga, M.; Logothetidis, S.; and Cardona, M. Phys. Rev. B 35: 9174 1987.

[48] Logothetidis, S.; Viña, L.; and Cardona, M. Phys. Rev. B 31: 947 1985.

[49] Lautenschlager, P.; Garriga, M.; and Cardona, M. Phys. Rev. B 36: 4813 1987.

[50] Logothetidis, S.; Cardona, M.; and Garriga, M. Phys. Rev. B 43: 11950 1991.

[51] Gopalan, S.; Lautenschlager, P.; and Cardona, M. Phys. Rev. B 35: 5577 1987.

[52] Christensen, D.H.; Pellegrino, J.G.; Hickernell, R.K.; Crochière, S.M.; Parsons, C.A.; and Rai, R.S. J. Appl. Phys. 72: 5982 1992.

[53] Hickernell, R.K.; Christensen, D.H.; Pellegrino, J.G.; Wang, Jin; and Leburton, Jean-Pierre. J. Appl. Phys. 75: 3056 1994.

[54] Kahen, K.B. and Leburton, J.P. Appl. Phys. Lett. 49: 734 1986.

[55] Wang, J.; Leburton, J.P.; and Zucker, J.E. IEEE J. Quant. Elec. 30: 989 1994.

[56] Christensen, D.H.; Hickernell, R.K.; Schaafsma, D.T.; Pellegrino, J.G.; McCollum, M.J.; Hill, J.R.; and Rai, R.S. In Glembocki, O.J., editor, *Spectroscopic Characterization Techniques for Semiconductor Technology V* Proc.SPIE, vol.2141 page 177 Bellingham, WA 1994. SPIE Publications.

[57] Kelvin, Lord (Sir W. Thompson). *Reprints of Papers on Electrostatics and Radiating Systems.* Macmillan London second edition 1884.

[58] Maxwell, J.C. *Treatise on Electricity and Magnetism.* Dover New York third edition 1954.

[59] Sommerfeld, A. Ann. Phys. 28: 665 1909.

[60] Fong, C.Y. and Kittel, C. Am. J. Phys. 35: 1091 1967.

[61] Pumplin, J. Am. J. Phys. 37: 737 1969.

[62] Glasser, M.L. Am. J. Phys. 38: 415 1970.

[63] Ianovici, M. and Morf, J.-J. IEEE Trans. EI-12: 165 1977.

[64] Hague, B. *Electromagnetic Problems in Electrical Engineering.* Oxford University Press London 1929.

[65] Silvester, P. Proc. IEEE 115: 43 1968.

[66] Stehle, P. Phys. Rev. A 2: 102 1970.

[67] Lindell, I.V. and Alanen, E. IEEE Trans. AP-32: 126,841,1027 1984.

[68] Fang, D.G.; Yang, J.J.; and Delisle, G.Y. Proc. IEE 135H: 297 1988.

[69] Chow, Y.L.; Yang, J.J.; Fang, D.G.; and Howard, G.E. IEEE Trans. Microwave Theory and Tech. 39: 588 1991.

[70] Kipp, R.A. and Chan, C.H. IEEE Trans. Microwave Theory and Tech. 42: 860 1994.

[71] Barton, G. *Elements of Green's Functions and Propagation.* Clarendon Press Oxford 1989.

[72] Dowling, J.P.; Scully, M.O.; and DeMartini, F. Opt. Commun. 82: 415 1991.

[73] Dowling, J.P. and Bowden, C.M. Phys. Rev. A 46: 612 1992.

[74] Milonni, P.W. and Knight, P.L. Opt. Commun. 9: 119 1973.

[75] Lamb, W.E. and Retherford, R.C. Phys. Rev. 72: 241 1947.

[76] Bethe, H.A. Phys. Rev. 72: 339 1947.

[77] Purcell, E.M. Phys. Rev. 69: 681 1946.

[78] Drexhage, K.H. *Progress in Optics* volume 12 page 165. North-Holland Amsterdam 1974.

[79] Goy, P.; Raimond, J.M.; Gross, M.; and Haroche, S. Phys. Rev. Lett. 50: 1903 1983.

[80] Hulet, R.G.; Hilfer, E.S.; and Kleppner, D. Phys. Rev. Lett. 55: 2137 1985.

[81] Heinzen, D.J. and Feld, M.S. Phys. Rev. Lett. 59: 192 1987.

[82] DeMartini, F.; Innocenti, G.; Jacobovitz, G.R.; and Mataloni, P. Phys. Rev. Lett. 59: 2955 1987.

[83] Einstein, A. Phys. Z. 18: 121 1917.

[84] Sakurai, J.J. *Advanced Quantum Mechanics.* Addison-Wesley Publishing Reading, MA 1967.

[85] Loudon, R. *The Quantum Theory of Light.* Clarendon Press Oxford 1983.

[86] Sargent, M.; Scully, M.O.; and Lamb, W.E. *Laser Physics.* Addison-Wesley Publishing Reading, MA 1974.

[87] Cohen-Tannoudji, C.; Dupont-Roc, J.; and Grynberg, G. *Atom-Photon Interactions.* Wiley Interscience New York 1992.

[88] Barut, A.O. and Kraus, J. Foundations of Physics 13: 189 1983.

[89] Barut, A.O. and van Heule, J.F. Phys. Rev. A 32: 3187 1985.

[90] Barut, A.O.; Dowling, J.P.; and van Heule, J.F. Phys. Rev. A 38: 4405 1988.

[91] Barut, A.O. and Dowling, J.P. Phys. Rev. A 41: 2284 1990.

[92] Crisp, M.D. Phys. Rev. A 43: 4058 1991.

[93] Heinzen, D.J. *Radiative Decay and Level Shift of an Atom in an Optical Resonator.* PhD thesis Massachusetts Institute of Technology 1988.

[94] Pankove, J.I. RCA patent report 1963.

[95] Melngailis, I. Appl. Phys. Lett. 6: 59 1965.

[96] Scifres, D.R.; Burnham, R.D.; and Streifer, W. Appl. Phys. Lett. 26: 48 1975.

[97] Springthorpe, A.J. Appl. Phys. Lett. 31: 524 1977.

[98] Soda, H.; Iga, K.; Kitahara, C.; and Suematsu, Y. Japn. J. Appl. Phys. 18: 2239 1979.

[99] Okuda, H.; Soda, H.; Moriki, K.; Motegi, Y.; and Iga, K. Japn. J. Appl. Phys. 20: L563 1981.

[100] Soda, H.; Motegi, Y.; and Iga, K. IEEE J. Quant. Elec. QE-19: 1035 1983.

[101] Passner, A.; Gibbs, H.M.; Gossard, A.C.; McCall, S.L; Venkatesan, T.N.C.; and Wiegmann, W. IEEE J. Quant. Elec. QE-16: 1283 1980.

[102] Ogura, M.; Hata, T.; Kawai, N.J.; and Yao, T. Japn. J. Appl. Phys. 22: L112 1983.

[103] Kojima, K.; Noda, S.; Mitsunaga, K.; Kyuma, K.; Hamanaka, K.; and Nakayama, T. Appl. Phys. Lett. 50: 227 1987.

[104] Jewell, J.L.; Harbison, J.P.; Scherer, A.; Lee, Y.H.; and Florez, L.T. IEEE J. Quant. Elec. 27: 1332 1991.

[105] Peters, M.B.; Young, D.B.; Peters, F.H.; Scott, J.W.; Thibeault, B.J.; and Coldren, L.A. IEEE Photon. Tech. Lett. 6: 31 1994.

[106] Chalmers, S.A.; Lear, K.L.; and Killeen, K.P. Appl. Phys. Lett. 62: 1585 1993.

[107] Tai, K.; Yang, L.; Want, Y.H.; Wynn, J.D.; and Cho, A.Y. Appl. Phys. Lett. 56: 2496 1990.

[108] Lu, B.; Zhou, P.; Cheng, J.; and Malloy, K.J. In Jewell, J.L., editor, *Vertical-Cavity Surface-Emitting Laser Arrays* volume 2147 page 12 Bellingham, WA 1994. SPIE Publications.

[109] McMahon, C.H.; Bae, J.W.; Menoni, C.S.; Patel, D.; Temkin, H.; Brusenbach, P.; and Leibenguth, R. Appl. Phys. Lett. 66: 2171 1995.

[110] Young, D.B.; Scott, J.W.; Peters, F.H.; Thibeault, B.J.; Corzine, S.W.; Peters, M.G.; Lee, S.-L.; and Coldren, L.A. IEEE Photon. Tech. Lett. 5: 129 1993.

[111] Tai, K.; Fischer, R.J.; Wang, K.W.; Chu, S. N.G.; and Cho, A.Y. Electron. Lett. 25: 1644 1989.

[112] Lee, Y.H.; Jewell, J.L.; Scherer, A.; McCall, S.L.; Harbison, J.P.; and Florez, L.T. Electron. Lett. 25: 1377 1989.

[113] Huffaker, D.L. and Deppe, D.G. Appl. Phys. Lett. 67: 2594 1995.

[114] Tauber, D.; Wang, G.; Geels, R.S.; Bowers, J.E.; and Coldren, L.A. Appl. Phys. Lett. 62: 325 1993.

[115] Dziura, T.G.; Yang, Y.J.; Fernandez, R.; and Wang, S.C. In Jewell, J.L., editor, *Vertical-Cavity Surface-Emitting Laser Arrays* volume 2147 page 40 Bellingham, WA 1994. SPIE Publications.

[116] Michalzik, R. and Ebeling, K.J. IEEE J. Quant. Elec. 29: 1963 1993.

[117] Vakhshoori, D.; Novothny, R.A.; Leibenguth, R.E.; and Wynn, J.D. In Jewell, J.L., editor, *Vertical-Cavity Surface-Emitting Laser Arrays* volume 2147 page 22 Bellingham, WA 1994. SPIE Publications.

[118] Kobyashi, T.; Segawa, T.; Morimoto, A.; and Sueta, T. In *43rd Fall Meeting of the Japanese Society of Applied Physics* Tokyo 1982. Japanese Applied Physics Society. in Japanese.

[119] DeMartini, F. and Jacobovitz, J.R. Phys. Rev. Lett. 60: 1711 1988.

[120] Yokoyama, H.; Nishi, K.; Anan, T.; Nambu, Y.; Brorson, S.D.; Ippen, E.P.; and Suzuki, M. Opt. Quant. Elec. 24: 5245 1992.

[121] Lau, K.Y.; Derry, P.L.; and Yariv, A. Appl. Phys. Lett. 52: 88 1988. Calculates the low threshold current limit of edge emitting QW lasers to be 0.55 mA (but does not convert to a current density).

[122] Wipiejewski, T.; Panzlaff, K.; Zeeb, E.; and Ebeling, K.J. In Jewell, J.L., editor, *Vertical-Cavity Surface-Emitting Laser Arrays* volume 2147 page 48 Bellingham, WA 1994. SPIE Publications.

[123] Chang-Hasnain, C.J.; Wu, Y.A.; Li, G.S.; Hasnain, G.; Choquete, K.D.; Caneau, C.; and Florez, L.T. Appl. Phys. Lett. 63: 1307 1993. Reports a threshold of 490 A/cm^2, which seems to be the lowest to date.

[124] Yamamoto, Y.; Machida, S.; and Björk, G. Surf. Sci. 267: 605 1992.

[125] Yamamoto, Y.; Machida, S.; and Björk, G. Opt. Quant. Elec. 24: S215 1992.

[126] Yamamoto, Y.; Matinaga, F.; Machida, S.; Karlsson, A.; Jacobson, J.; Björk, G.; and Mukai, T. J. de Physique IV 3: 39 1993.

[127] Houdré, R.; Stanley, R.P.; Oesterle, U.; Ilegems, M.; and Weisbuch, C. J. de Physique IV 3: 51 1993.

[128] Zhu, Yifu; Gauthier, Daniel J.; Morin, S.E.; Wu, Qilin; Carmichael, H.J.; and Mossberg, T.W. Phys. Rev. Lett. 64: 2499 1990.

[129] Huang, Z.; Lei, C.; Deppe, D.G.; Lin, C.C.; Pinzone, C.J.; and Dupuis, R.D. Appl. Phys. Lett. 61: 2961 1992.

[130] Lei, C.; Huang, Z.; Deppe, D.G.; Pinzone, C.J.; and Dupuis, R.D. J. Appl. Phys. 73: 2700 1993.

[131] Schnitzer, I.; Yablonovitch, E.; Caneau, C.; and Gmitter, T.J. Appl. Phys. Lett. 62: 131 1993.

[132] Rabi, I.I. Phys. Rev. 51: 652 1937.

[133] Jaynes, E.T. and Cummings, F.W. Proc. IEEE 51: 89 1963.

[134] Agarwal, G.S. J. Opt. Soc. Am. B 2: 480 1985.

[135] Weisbuch, C.; Houdré, R.; and Stanley, R.P. *Spontaneous Emission and Laser Oscillation in Microcavities* page 109. CRC Press Boca Raton 1995.

[136] Jackson, J.D. *Classical Electrodynamics.* Wiley New York 1975.

[137] Airy, G.B. Phil. Mag. 2: 20 1833.

[138] Verdeyen, J.T. *Laser Electronics.* Prentice-Hall Englewood Cliffs, NJ 1981.

[139] Yariv, A. *Optical Electronics.* Holt, Reinhart, and Winston New York 3rd edition 1985.

[140] Yariv, A. *Quantum Electronics.* John Wiley & Sons New York 3rd edition 1989.

[141] Fowles, G.R. *Introduction to Modern Optics.* Dover New York 2nd edition 1975.

[142] Born, Max and Wolf, Emil. *Principles of Optics.* Pergamon Press Oxford 1980.

[143] Sakurai, J.J. *Modern Quantum Mechanics.* Benjamin/Cummings Publishing Menlo Park, CA 1985.

[144] Weisbuch, C. and Vinter, B. *Quantum Semiconductor Structures.* Academic Press Boston 1991.

[145] The modeling of QW refractive indices used in parts of this work was done by J.-P. Leburton and others at the University of Illinois in collaboration with modeling efforts at NIST. This model is documented in Ref.[55].

[146] Young, M. *Optics and Lasers Including Fibers and Optical Waveguides.* Springer-Verlag Berlin 1993.

[147] Zarem, H.A.; Lebens, J.A.; Nordstrom, K.B.; Sercel, P.C.; Sanders, S.; Eng, L.E.; Yariv, A.; and Vahala, K.J. Appl. Phys. Lett. 55: 2622 1989.

[148] Andreani, L.C. and Pasquarello, A. Phys. Rev. B 42: 8928 1990. cited in [135].

[149] Kanda, M. IEEE Trans. Ant. Prop. AP-26: 439 1978.

[150] Guido, L.J.; Holonyak, Jr., N.; Hsieh, C.; Kliski, R.W.; Plano, W.E.; Burnham, R.D.; Thornton, R.L.; Epler, J.E.; and Paoli, T.L. J. Appl. Phys. 61: 1372 1987.

[151] Schlesinger, T.E. and Keuch, T. Appl. Phys. Lett. 49: 519 1986.

[152] Sallese, J.M.; Taylor, S.; Buhlmann, H.J.; Carlin, J.F.; Rudra, A.; Houdré, R.; and Ilegems, M. Appl. Phys. Lett. 65: 341 1994.

[153] Casey, Jr., H.C.; Sell, D.D.; and Wecht, K.W. J. Appl. Phys. 46: 250 1975.

[154] Philipp, H.R. and Ehrenreich, H. Phys. Rev. 129: 1550 1963.

[155] Yim, W.M. J. Appl. Phys. 42: 2854 1971.

[156] Fern, R.E. and Onton, A. J. Appl. Phys. 42: 3499 1971.

[157] Monemar, B.; Shih, K.K.; and Pettit, G.D. J. Appl. Phys. 47: 2604 1976.

[158] van der Ziel, J.P. and Gossard, A.C. J. Appl. Phys. 48: 3018 1977.

[159] Burkhard, H.; Dinges, H.W.; and Kuphal, E. J. Appl. Phys. 53: 655 1982.

[160] Garriga, M; Lautenschlager, P.; Cardona, M.; and Ploog, K. Sol. St. Comm. 61: 157 1987.

[161] Greene, R.L.; Bajaj, K.K.; and Phelps, D.E. Phys. Rev. B 29: 1807 1984.

[162] Bastard, G.; Mendez, E.E.; Chang, L.L.; and Esaki, L. Phys. Rev. B 26: 1974 1982.

[163] Miller, R.C.; Kleinman, D.A.; and Gossard, A.C. Phys. Rev. B 29: 7085 1984.

[164] Lawaetz, P. Phys. Rev. B 4: 3460 1971.

[165] Braunstein, R. and Kane, E.O. J. Phys. Chem. Solids 23: 1423 1962.

[166] Cardona, M. J. Phys. Chem. Solids 24: 1543 1963.

[167] Vrehen, Q. H.F. J. Phys. Chem. Solids 29: 129 1968.

[168] Stillman, G.E.; Wolfe, C.M.; and Dimmock, J.O. Sol. St. Comm. 7: 921 1969.

[169] Mears, A.L. and Stradling, R.A. J. Phys. C 4: L22 1971.

[170] Blakemore, J.S. J. Appl. Phys. 53: 520 1982.

[171] Ji, G.; Huang, D.; Reddy, U.K.; Unlu, H.; Henderson, T.S.; and Morkoç, H. J. Vac. Sci. Technol. B 5: 1346 1987.

[172] Ľ. Hrivnák. Appl. Phys. Lett. 56: 2425 1990.

[173] Barut, A.O. and Dowling, J.P. Phys. Rev. A 36: 649 1987.

[174] Sparnaay, M.J. Physica 24: 751 1958.

[175] Sukenik, C.I.; Boshier, M.G.; Cho, D.; Sandoghdar, V.; and Hinds, E.A. Phys. Rev. Lett. 70: 560 1993.

[176] Casimir, H. B.G. Proc. Kon. Ned. Akad. Wetenschap. B 51: 793 1948.

[177] Casimir, H. B.G. and Polder, D. Phys. Rev. 73: 360 1948.

A Interdiffusion in GaAs Quantum Wells

Vacancy-enhanced diffusion plays a large role in compound semiconductor devices in general and a critical role in VCSEL devices in particular. The exchange of crystal ions through a vacancy site in the lattice can lead to large changes in the optical response of vertical-cavity laser devices: the mirror response can flatten, broaden, or even shift in wavelength (due to changes in the refractive index profile), and the quantum wells can interdiffuse with their own barriers, causing the peak of the gain medium to shift. As the normal fabrication of VCSEL devices involves high-temperature processing (even during the growth), diffusion effects are of great concern to making a viable laser device.

The traditional model of atomic diffusion processes in crystalline semiconductors is based on the assumption that the rate at which defects are introduced into the solid is a function only of the ambient vapor and the Fermi energy of the solid. This model ignores, among other things, the vacancies introduced by the substrate and by the epitaxial growth technology.

A model developed by workers at Yale University and tested in conjunction with this work offers a more comprehensive view of diffusion processes. This model views the annealing of an epitaxial structure as a three-phase equilibrium problem between the annealing ambient (vapor phase), the epitaxial layers (solid phase), and the substrate (solid phase). It allows defect concentrations to equilibrate under the thermal profile created during the annealing and can take into account many growth techniques and substrate types.

The test of this model was performed using the cross-sectional photoluminescence (XPL) technique described in Ch. 4. The XPL measurements allowed the parameter space of the interdiffusion experiment to be folded down to a more manageable size, incorporating several parameters into a simultaneous measurement. Specifically, a "basis" specimen was grown and then divided into several pieces to be annealed under different conditions. The design of the growth included five GaAs quantum wells (in AlGaAs barriers), spaced roughly 1 μm apart, which would span different temperatures during a single annealing and which would probe different regions of the specimen, either closer to the surface or to the substrate, where the defect concentration might vary (see Fig. 62). In fact, many studies of interdiffusion have been limited to regions very close to the surface[150] or cryogenic temperatures[151, 152]. XPL alleviates both of these constraints.

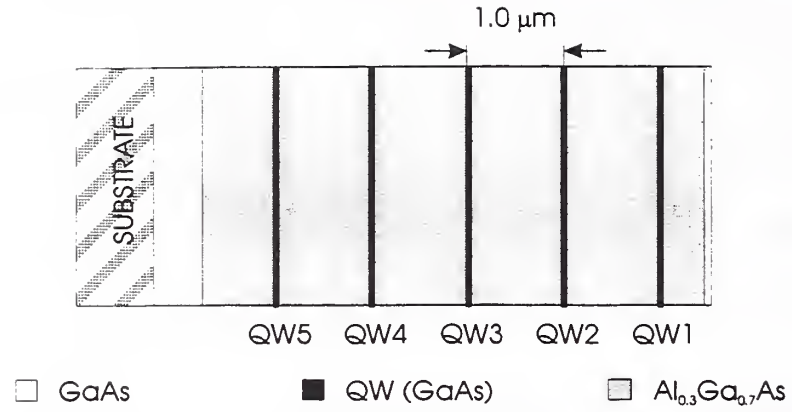

Figure 62: The structure used for the annealing tests. QW1 is closest to the surface and QW5 is closest to the substrate.

Given that the As stoichiometry throughout the specimen was roughly uniform, the biggest changes were to be expected from movement of the group-III atoms, Al and Ga. Specifically, interdiffusion of Al into the quantum wells would cause a change in the barrier profile, and hence a change in the energy levels and the emission energy of the quantum well, mostly due to a thinning of the well. Using XPL, the emission peak of each QW in the structure could be probed individually and the shift of those peaks with annealing conditions could be fit to the three-phase model.

The model itself is simply a set of coupled differential equations governing the migration of defects and host atoms in the crystal:

$$\begin{aligned} \frac{\partial}{\partial t}\Big([C_{Al}](x,t)\Big) &= D^0_{Al-Ga}\frac{\partial}{\partial x}\left\{[C_{defect}](x,t)\frac{\partial}{\partial x}\Big([C_{Al}](x,t)\Big)\right\} \\ \frac{\partial}{\partial t}\Big([C_{defect}](x,t)\Big) &= D_{defect}\frac{\partial^2}{\partial x^2}\Big([C_{defect}](x,t)\Big), \end{aligned} \tag{47}$$

where $[C_{Al}]$ is the aluminum atom concentration, $[C_{defect}]$ is the defect concentration, and D^0_{Al-Ga} and D_{defect} are the diffusion coefficients for group-III atoms and defects. As this process is vacancy-enhanced, the actual Al-Ga interdiffusion coefficient depends also on the concentration of vacancies, viz.:

$$D_{Al-Ga} = D^0_{Al-Ga} \times [C_{defect}]^n \tag{48}$$

(in this case, the dependence is linear; $n = 1$.)

The concentration of defects at the surface is a function only of the annealing overpressure (or the partial pressure of arsenic in the annealing ambient), P_{As_4}, and the annealing temperature T_{ann}, whereas the defect concentration in the epilayer and substrate depends on T_{ann} and the stoichiometry of the layer (substrate). The concentration of aluminum as

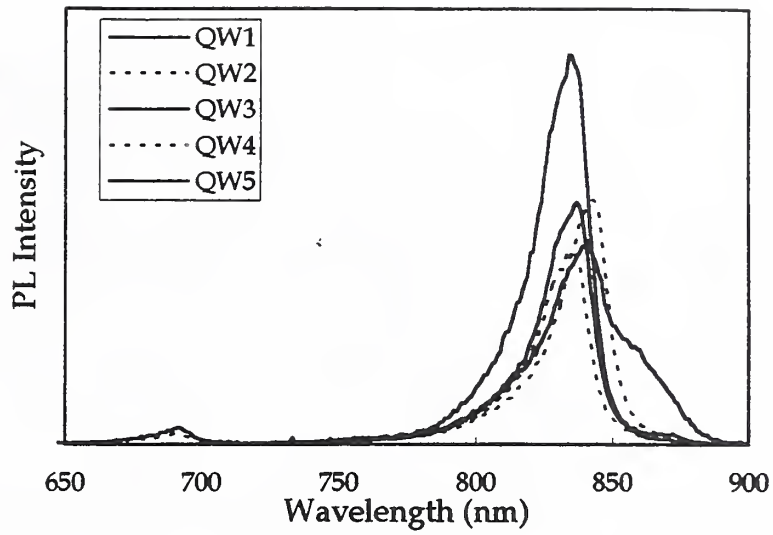

Figure 63: Cross-sectional PL spectra of the unannealed specimen.

a function of time and position is thus dependent on five parameters: the two diffusion coefficients D^0_{Al-Ga} and D_{defect}, and the three intial defect concentrations $[C_{defect}]^0_{surface}$, $[C_{defect}]^0_{epilayer}$, and $[C_{defect}]^0_{substrate}$. Once the Al concentration is known, the energy levels of the QW can be solved numerically and the emission peak energy obtained. Conversely, a standard curve-fitting algorithm can be used to reduce the peak shift data from the annealed QWs to a set of consistent parameters, since the the five QWs in the structure correspond to the size of the parameter space for a given annealing temperature and pressure. A number of specimens are needed to map out the time and temperature and pressure regimes.

Figure 63 shows the XPL spectra for the portion of the specimen left unannealed. All five QWs are clearly resolved, though surface-normal identification at room temperature would be at best difficult. The small peak on the short-wavelength end of the spectrum is the barrier emission. The emission peaks of the same QWs after annealing are shown in Fig. 64. Again, all five QWs are resolved individually by the XPL technique and their energy peaks can be used to generate a single set of fit parameters, as described above. Uncertainties in this determination can be further reduced by fitting the energy shift as a function of annealing time (for example). For the series of specimens including the two in Figs. 63 and 64, the time evolution of the Al concentration profile (peak energy shift) is shown in Fig. 65. The modeled shifts (lines) were generated using a single set of parameters and then following the time evolution of the Al concentration across each QW.

This fit is very good and serves as something of a verification of the three-phase model, the strength of which is the unique parameter determination (i.e., self-consistency in spatio-temporal variation). In addition, it highlights the utility of the XPL technique, which in this case has provided valuable information that is completely unavailable to or very difficult to obtain from surface probes.

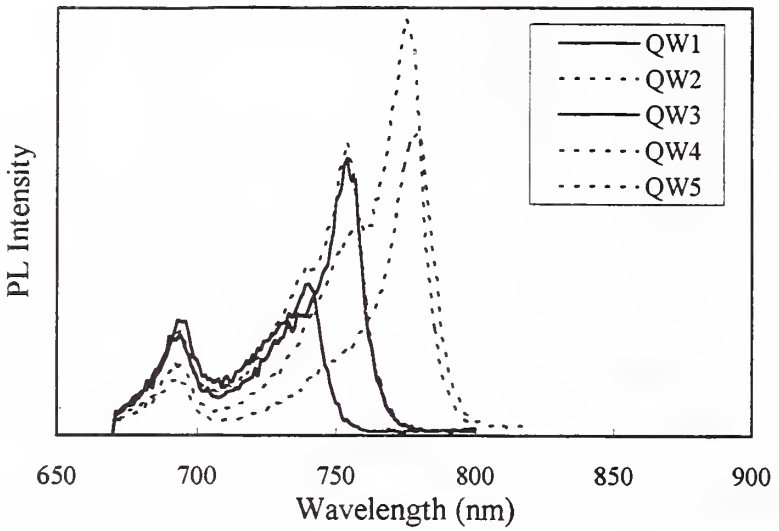

Figure 64: Cross-sectional PL spectra of the annealed specimen. The specimen was annealed for 3 h at 835°C in 1 atm As overpressure.

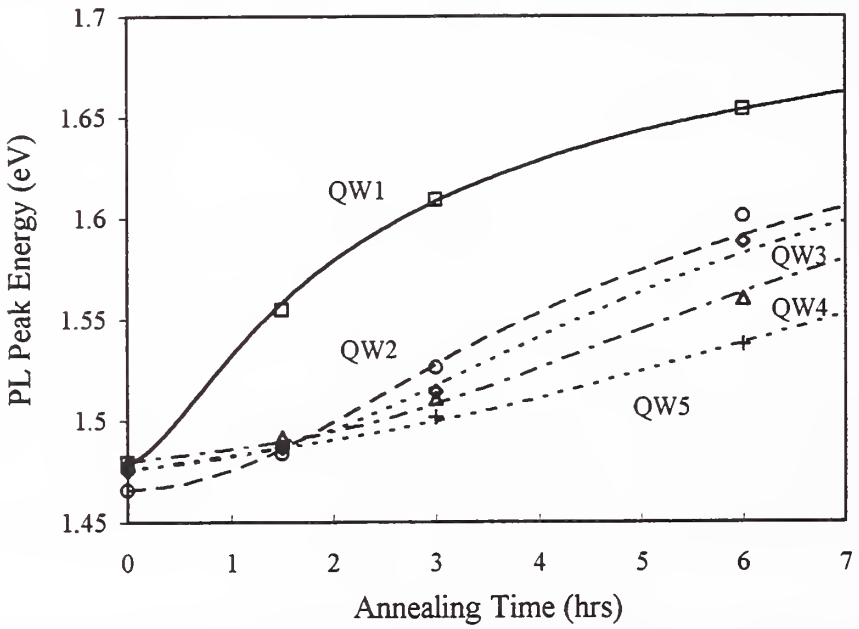

Figure 65: Emission peak as a function of annealing time for the five quantum wells in the annealing test. The data are the points, fitted by the solid or dashed lines of the model using a single set of parameters.

B Multilayer Modeling

B.1 Modeling Optical Response in VCSELs

Even the simplest VCSEL structure is a complex photonic object. As discussed in the preceeding chapters, the coupling of light into a cavity mode and the feedback coupling of light in a mode to the emitter itself are both dependent on the precise magnitude of the standing field in the cavity. Sophisticated optical models are required not only to predict emission responses and hence gauge cavity coupling effects, but also to estimate the magnitude of the coupling. Since small variations in the construction parameters (thickness, alloy composition, etc.) can greatly impact the optical response, a model which is very sensitive to variations in those parameters is also quite valuable. Furthermore, the basic metrology of VCSELs is also well served by greater information on systematic variations. Many of these variations can be quite accurately assessed with spectral reflectance modeling.

B.1.1 Reflectance Spectra and General Prescriptions

The modeling of the spectral reflectance, as performed in this work, followed the standard prescription dictated by propagating electric fields across the interfaces using the appropriate Fresnel coefficients. Specifically, for a wave traveling from medium j into medium $j+1$,

$$\left(\frac{E_t}{E_0}\right)^{TE}_{j,j+1} = t^{TE}_{j,j+1} = \frac{2n_j \cos\theta_j}{n_j \cos\theta_j + \left(\frac{\mu_j}{\mu_{j+1}}\right) n_{j+1} \cos\theta_{j+1}} \tag{49}$$

$$\left(\frac{E_r}{E_0}\right)^{TE}_{j,j+1} = r^{TE}_{j,j+1} = \frac{n_j \cos\theta_j - \left(\frac{\mu_j}{\mu_{j+1}}\right) \cos\theta_{j+1}}{n_j \cos\theta_j + \left(\frac{\mu_j}{\mu_{j+1}}\right) n_{j+1} \cos\theta_{j+1}} \tag{50}$$

for the TE part of the wave, and

$$\left(\frac{E_t}{E_0}\right)^{TM}_{j,j+1} = t^{TM}_{j,j+1} = \frac{2n_j/\cos\theta_j}{\frac{n_j}{\cos\theta_j} + \left(\frac{\mu_j}{\mu_{j+1}}\right) \frac{n_{j+1}}{\cos\theta_{j+1}}} \tag{51}$$

$$\left(\frac{E_r}{E_0}\right)^{TM}_{j,j+1} = r^{TM}_{j,j+1} = \frac{\left(\frac{\mu_j}{\mu_{j+1}}\right) \frac{n_{j+1}}{\cos\theta_{j+1}} - \frac{n_j}{\cos\theta_j}}{\frac{n_j}{\cos\theta_j} + \left(\frac{\mu_j}{\mu_{j+1}}\right) n_{j+1} \cos\theta_{j+1}} \tag{52}$$

for the TM part. μ is the susceptibility of the material; n is its refractive index — which in general is a complex number — and the angles θ are defined by Re{Snell's law}. The iterative reflection coefficient for layer j, representing reflections from all layers below j, is then

$$\rho_j = \frac{r_{j,j+1} + \rho_{j+1} e^{i2\phi_{j+1}}}{1 + r_{j,j+1}\rho_{j+1} e^{i2\phi_{j+1}}}, \tag{53}$$

where $\phi_{j,j+1} = n_{j+1}\omega c z_{j+1} \cos\theta_{j+1}$ is the phase change across layer $j+1$ and z_{j+1} is the thickness of the layer. If the layers are numbered increasingly (from 1 to j_{MAX}) as one

moves down from the reflecting surface, the coefficient $\rho_{j_{MAX}}$ must be taken to be zero (where the light escapes the back surface of the structure). The field (intensity) reflectance coefficient is then ρ_1 ($|\rho_1|^2$). This approach is valid also for a subset of a complete structure — e.g., a number of pairs taken from a mirror.

As the spectral reflectance is determined by the *optical* thickness (the product of refractive index and physical thickness) of the layers in the structure, the reflectance modeling must be coupled with other techniques such as X-ray diffraction (see Sec. 4.5.2) to determine the physical thicknesses. However, some trends can be identified with the aid of other optical techniques such as XPL, and the modeling of both emission and reflectance can yield valuable information about both construction parameters and basic physics in VCSELs. These modeling techniques are covered in greater detail later in this chapter (Sec. B.2); at this juncture, it is more instructive to discuss the emission modeling.

B.1.2 Emission Modeling

A number of the specimens examined for this work contained a number of quantum wells, mostly in a distributed quantum well configuration as described earlier (Fig. 4). Thus, it was necessary to find a modeling technique which would allow for variations such as multiple quantum wells. In order to use the internal-source Fabry-Perot equation (Eq. 14 or 15) for a VCSEL with an arbitrary number of quantum wells, under realistic collection conditions, the following prescription can be used:

1. A single QW (just above layer q) is selected and all the layers above and below it are segregated into two distinct parts.

2. The reflectances of the two parts are calculated using the above method (Eq. 53), yielding new complex reflection and transmission coefficients, r_q^T, r_q^B, t_q^T and t_q^B, corresponding to the top and bottom "effective mirrors."

3. These coefficients are then used in Eq. 15,

$$|t_q|^2 = |t_q^T|^2 \frac{\left(1 + |r_q^B|^2 + 2|r_q^B|^2 \cos\left[\frac{2n_q\omega z_q}{c}\right]\right)}{1 + |r_q^T|^2|r_q^B|^2 - 2|r_q^T||r_q^B| \cos\left[\frac{2\omega(n_q z_q + n_{q-1} z_{q-1})}{c}\right]}, \tag{54}$$

   where z_q is the distance from the QW to the interface directly below layer q. Note that if $n_q = n_{q-1}$, the equation reduces to the standard form for a QW in a cavity.

4. The preceding steps are repeated for each emitter in the structure and the results are then summed together, weighting each transmission result by the excitation level at the corresponding quantum well. This weighting is found by evaluating the pump field strength at the position of the quantum well,

$$T = \sum_{q=q_0}^{q_{max}} |t_q|^2 |E(z = z_{QW})|^2, \tag{55}$$

and the pump field distribution is found by much the same means as outlined above. It is possible to sum all the emitters coherently (using the electric field strengths) or incoherently (using intensities); further discussion of this point is made in Sec. B.2.4.

5. T is then summed over the collection angle of the optical system, repeating the calculation above for each angle in the summation. This sum approximates the integral

$$\int_0^{\theta_c} T(\theta) d\theta,$$

where θ_c is the collection angle (e.g., 40.5° for the 40× objective).

Other allowances may also be made to allow for the finite thickness of the quantum wells and for lowering the significance of the interfaces of the QW in the emission spectrum. Some of these ideas are explored later in this chapter (Sec. B.2).

B.1.3 Index Models

The index model used for the $Al_xGa_{1-x}As$ system is that of Terry[37], which is a fit of nine harmonic oscillators,

$$\epsilon = 1 + \sum_{m=1}^{9} A_m \left(\frac{1}{\mathcal{E} + \mathcal{E}_m + \imath\Gamma_m} - \frac{1}{\mathcal{E} - \mathcal{E}_m + \imath\Gamma_m} \right), \tag{56}$$

where ϵ is the complex dielectric constant ($n = \sqrt{\epsilon}$), A_m is the amplitude of the m^{th} oscillator, $\mathcal{E}_m$ is its center energy, Γ_m is its damping coefficient, and $\mathcal{E}$ is the photon energy. This provides an excellent fit to the data taken by Aspnes et al[42] for the entire composition range of the $Al_xGa_{1-x}As$ alloy. However, as mentioned in Ch. 2, the data uncertainty is large enough to allow matches to several different models. Two sets of data, taken by Aspnes and by Casey et al.[39], are shown with the model given above in: Figs. 66 for the real part and 67 for the imaginary part of GaAs (x=0); Figs. 68 and 69 for $Al_{0.315}Ga_{0.695}As$; and Figs. 70 and 71 for $Al_{0.804}Ga_{0.196}As$. The comparisons of data are for GaAs; data for the $Al_xGa_{1-x}As$ system are extremely limited and difficult to compare because few measurements have been made at corresponding alloy compositions. There are also little data for the near infrared region, from approximately 1 μm to 2 μm, particularly for the ternary alloys (i.e., not GaAs or AlAs). Figure 72 shows the spectral coverage of the data from various references for this material system.

Figure 73 shows two models for the emission function of a typical VCSEL structure, differing only in the refractive index of the AlGaAs layers. The model which shifts the alloy content by 5% moves the emission peak by 3 nm and drops its intensity by about 40%. The model with a constant offset of 0.05 to the real part of the index moves the peak 11 nm and lowers the intensity by 50%. As 0.05 is not an uncommon discrepancy between many models and data sets, it is apparent that the accuracy of the data is much more important than accurate determination of alloy content. For any sophisticated modeling effort, therefore, the accuracy of refractive index models — for *bulk* materials as well as quantum wells and superlattices — is of critical importance.

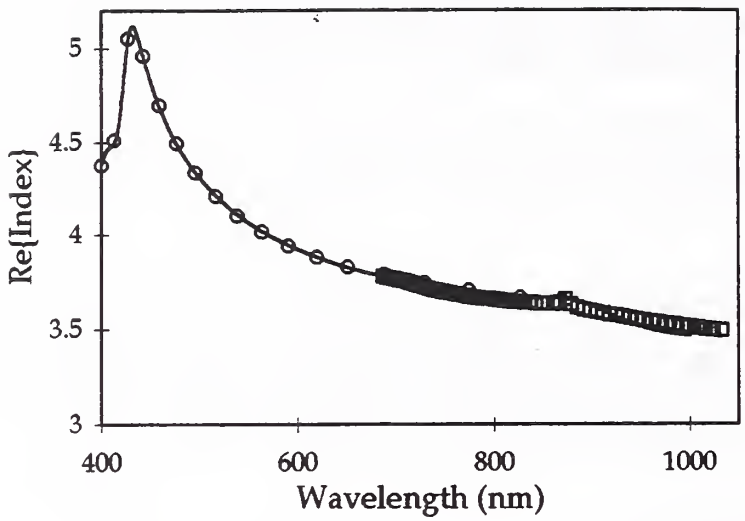

Figure 66: Comparison of refractive index data (real part) and models for the $Al_xGa_{1-x}As$ system for $x = 0$ (GaAs). The solid line is Terry's model, the open circles are Aspnes' data and the squares are the data of Casey, Sell, and Panish (references in the text).

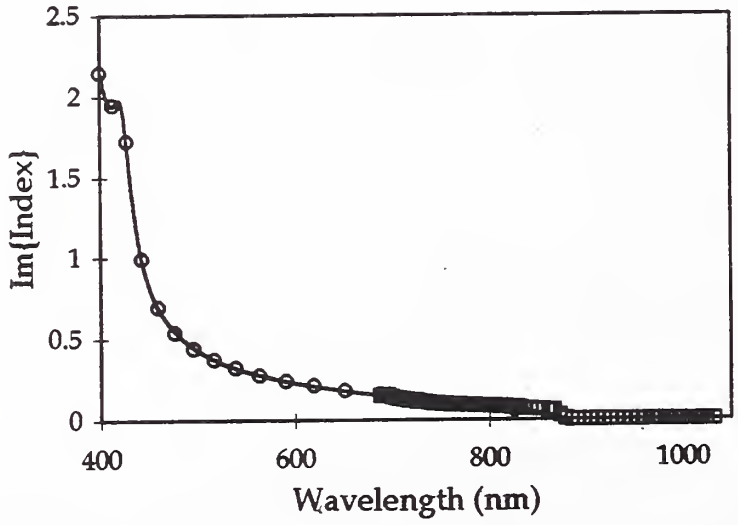

Figure 67: Comparison of refractive-index data (imaginary part) and models for the $Al_xGa_{1-x}As$ system for $x = 0$ (GaAs). The solid line is Terry's model, the open circles are Aspnes' data and the squares are the data of Casey, Sell, and Wecht[153].

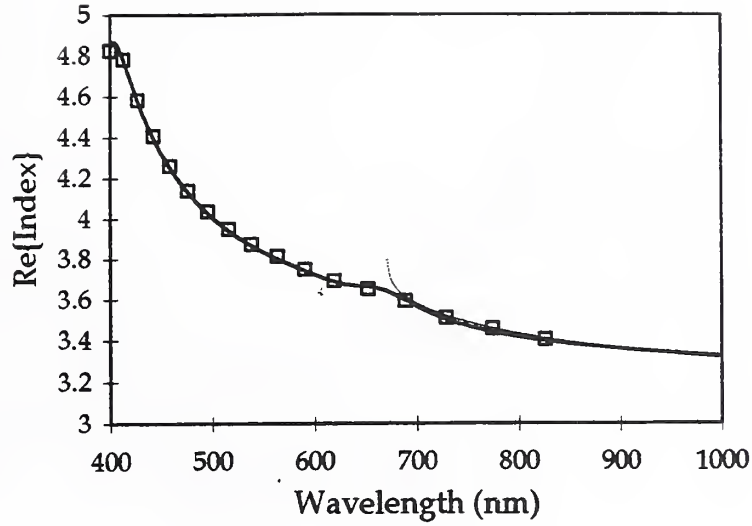

Figure 68: Comparison of refractive index data (real part) and models for the $Al_xGa_{1-x}As$ system for $x = 0.315$. The solid line is Terry's model, the dashed line is the model of Afromowitz[32], and the open circles are Aspnes' data.

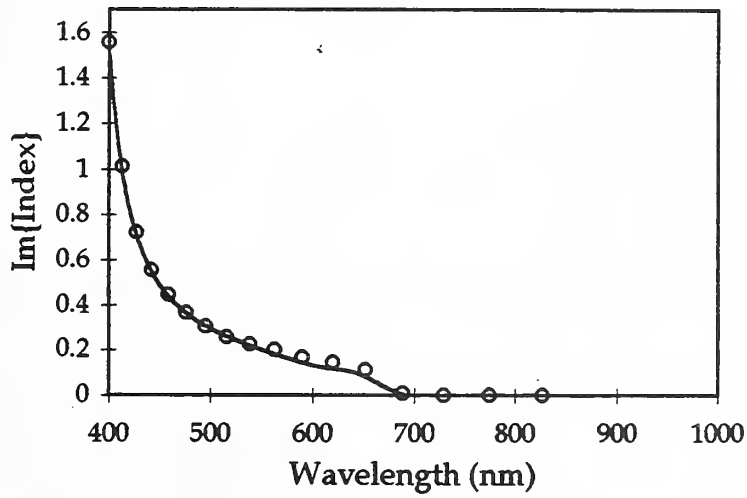

Figure 69: Comparison of refractive index data (imaginary part) and models for the $Al_xGa_{1-x}As$ system for $x = 0.315$. The solid line is Terry's model and the open circles are Aspnes' data.

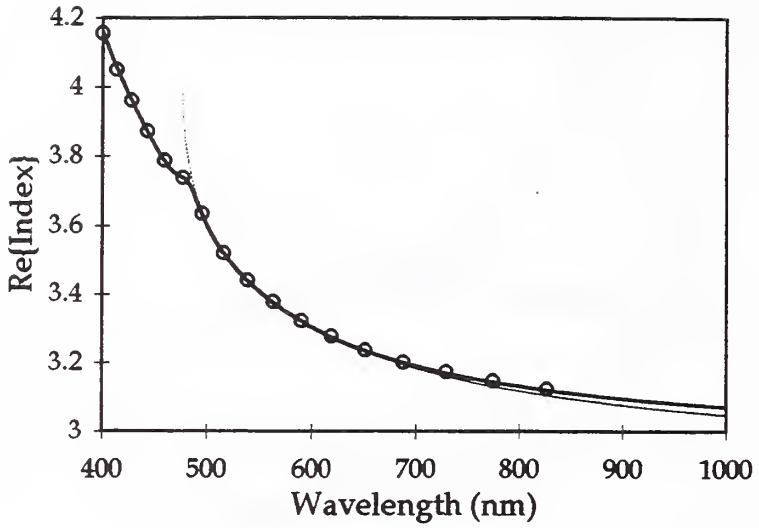

Figure 70: Comparison of refractive index data (real part) and models for the $Al_xGa_{1-x}As$ system for $x = 0.804$. The solid line is Terry's model, the dashed line is the model of Afromowitz[32], and the open circles are Aspnes' data.

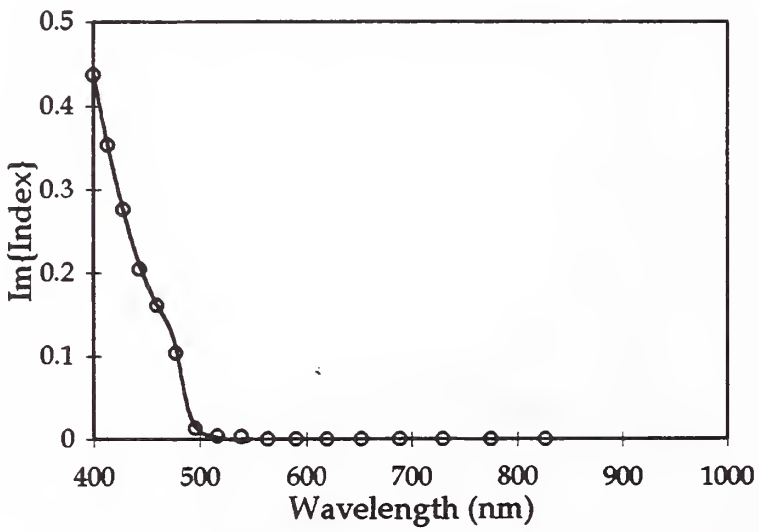

Figure 71: Comparison of refractive index data (imaginary part) and models for the $Al_xGa_{1-x}As$ system for $x = 0.804$. The solid line is Terry's model and the open circles are Aspnes' data.

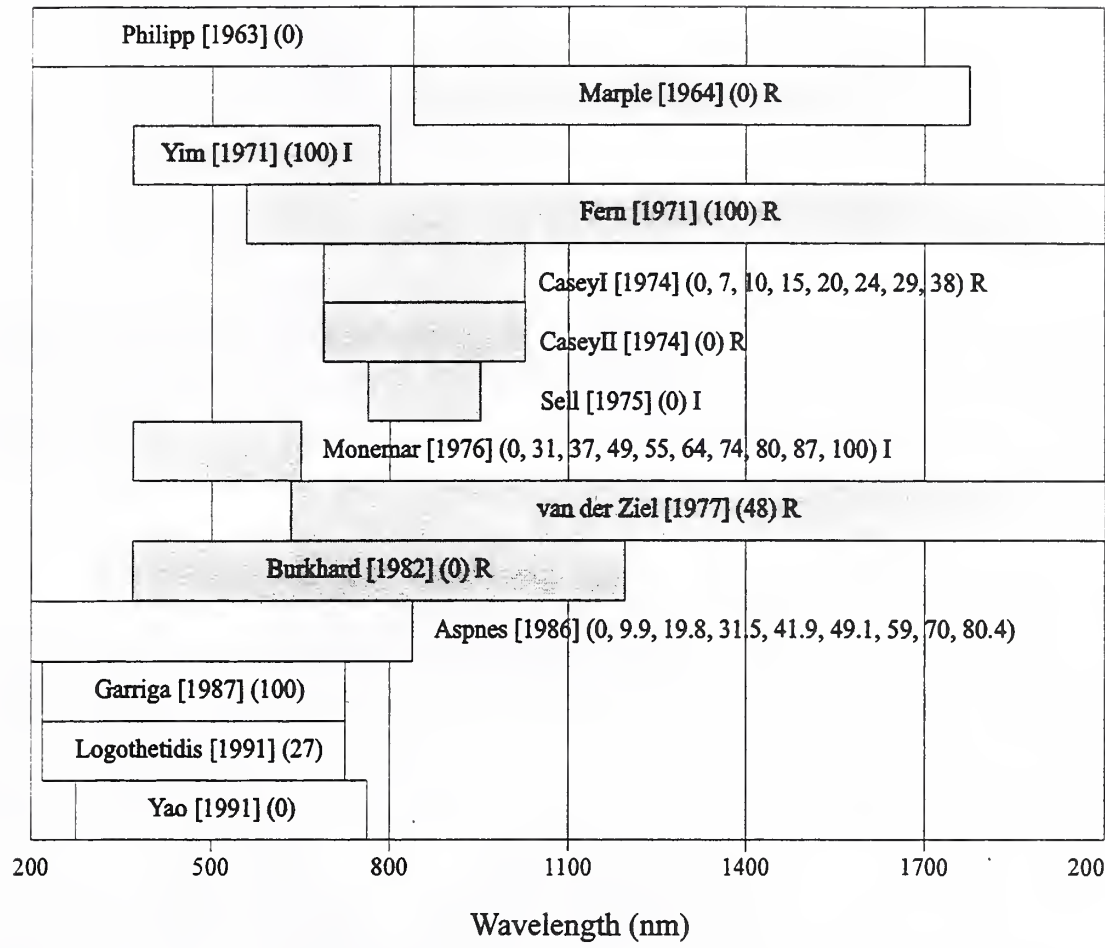

Figure 72: Spectral coverage of room-temperature index data in the $Al_xGa_{1-x}As$ system in the UV/VIS/NIR range. Boxes stand for the range of the data; open boxes are data with both Re{n} and Im{n}, shaded represent data for only one part, which is denoted by R for Re{n} and I for Im{n}. Brackets indicate the year of the study, parentheses the alloy compositions studied (in %). The references are as follows: Philipp[154], Marple[38], Yim[155], Fern[156], CaseyI[39], CaseyII[153], Sell[40], Monemar[157], van der Ziel[158], Burkhard[159], Aspnes[42], Garriga[160], Logothetidis[50], and Yao[41]. The heaviest concentration of data is apparently in the visible region from about 500 to 900 nm.

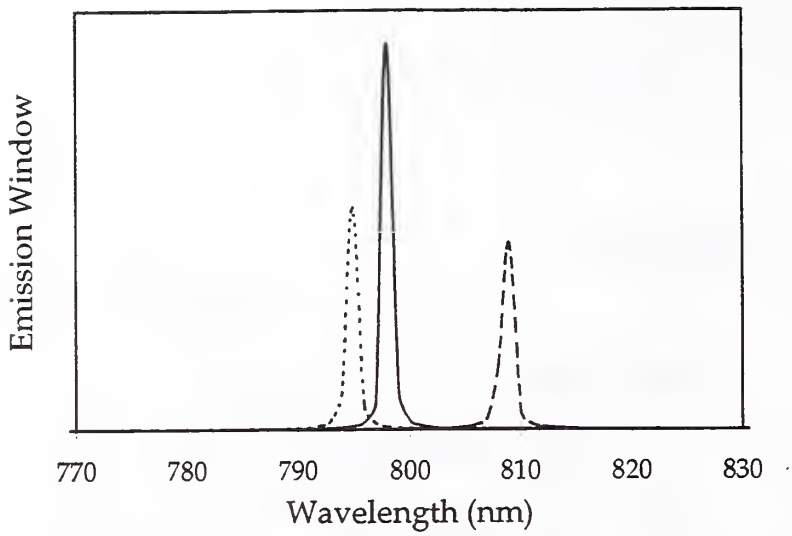

Figure 73: Emission window comparison for slight differences in the refractive index. The solid line is the "baseline" calculation, using the Terry model for all layers. The dotted line is the same calculation with the alloy content in the AlGaAs layers increased by 5%. The dashed line is the original calculation (Terry's model) with a constant factor of 0.05 added to the real part of the AlGaAs refractive index.

B.1.4 Pump Field Distributions

If the coefficients in Eq 53 are solved in terms of the incident intensity of the pump beam, the spatial distribution of the electric field of the pump can be mapped out inside the structure. As shown in Fig. 74, the profiles can vary dramatically for different structures and different wavelengths (and different incidence angles). This distribution can lead to much higher fields in the absorbing regions of the structure than the free-space field and a more rapid onset of thermal effects.

It is thus possible, by using different wavelengths, perhaps at different angles, to selectively excite different regions in a VCSEL device (provided those regions will absorb the wavelength of light used). In an optically pumped, periodic-gain device, for example, the distribution of the pump field should factor into the design along with the resonant field distribution.

Another factor to be considered with the distribution of the pump field is the absorption of the pump by layers in the structure. In particular, in a VCSEL where the cavity is AlGaAs and the mirrors are AlGaAs and AlAs (or GaAs), the absorption band in the near-IR and visible is quite broad. Optical excitation of these materials leads to free carrier generation, which in turn yields a change in the refractive index. A change in the index, of course, means that the optical thickness of the material has changed and thus the quarter-wave condition that was satisfied before may not be any longer. In essence, this effect is a kind of "bleaching" of the VCSEL by the pump: a high pump intensity and highly absorbing mirrors lead to the demise of the mirror reflectivity and shifting (and eventually Q-degradation) of the cavity modes. However, this effect is also easy to detect: When the mirrors begin to

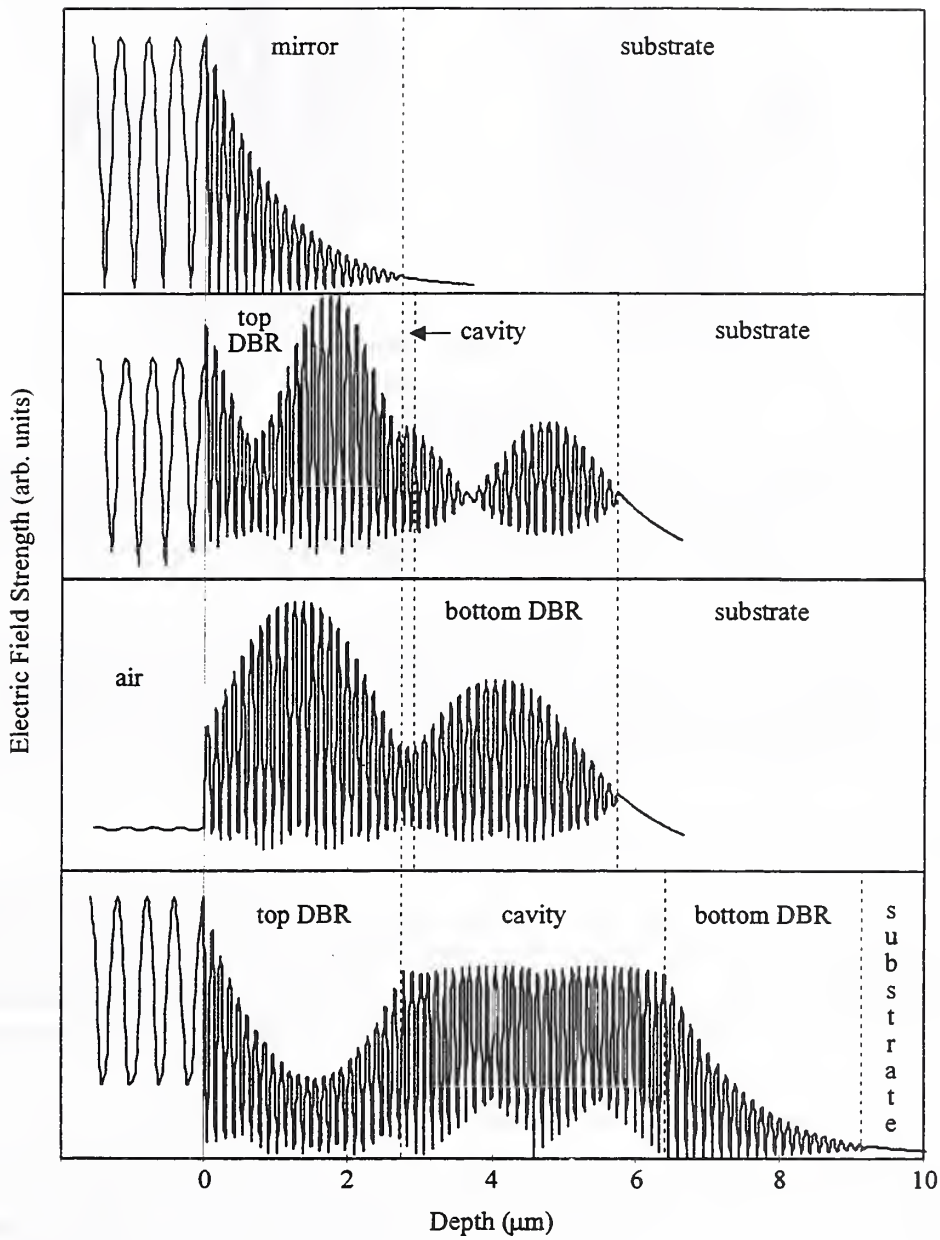

Figure 74: Comparison of pump field distributions for various structures and wavelengths. The curve at the top is a simple mirror structure with no cavity flaw. The next plot is a one-wavelength cavity VCSEL pumped at a wavelength corresponding to one of the minima in its interference fringes, and the third curve is the same VCSEL pumped at the nearest fringe maximum. The bottom graph is a 16-λ cavity pumped at a fringe minimum. The distance scale (horizontal axis) is constant in all four graphs.

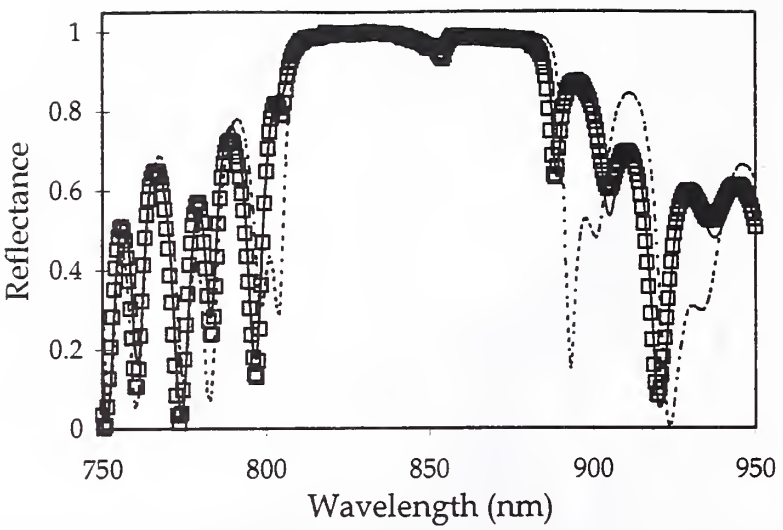

Figure 75: An example of changes in the optical response of a VCSEL due to slight variations in construction parameters. In this case, the model (solid line) that best fits the data (squares) is the one that includes a 3% thickness gradient (compare with the uniform-mirror model represented by the dashed line).

bleach, the modes will shift and the measured spectrum will change. In general, the stability of the mirrors under optical pumping can be more easily ascertained than the stability of the quantum well inside the VCSEL.

B.2 Measurement and Modeling Results

When all the factors are put together, the result is an accurate match to the optical response of the VCSEL. However, a number of variations, when taken into account in the model, can improve the agreement between predictions and data dramatically. The modeling of a typical DQW VCSEL device, then, might proceed in a fashion similar to that presented below.

B.2.1 Determination of Construction Parameters

Naturally, the first step is to determine the basic parameters of the device. Reflectance and X-ray diffraction can determine the average mirror pair thickness. XPL can determine the alloy compositions and the QW emission peak. Yet the story does not end there.

One example of how the reflectance data can change with a systematic variation is shown in Fig. 75. Two models are shown, along with the data (the open squares): The first (dashed line) uses only the best-fit optical thicknesses for the mirror pairs and the cavity spacer; the second includes a 3% physical thickness gradient, thinning the layers from the bottom to the top. (This corresponds to the case of decreasing growth rates over a long growth run, as is often the case with MBE.) The fit using the 3% gradient is quite a bit better than the uniform case, but it is also noticeably better than a simple mismatched-mirror fit (not shown in Fig. 75).

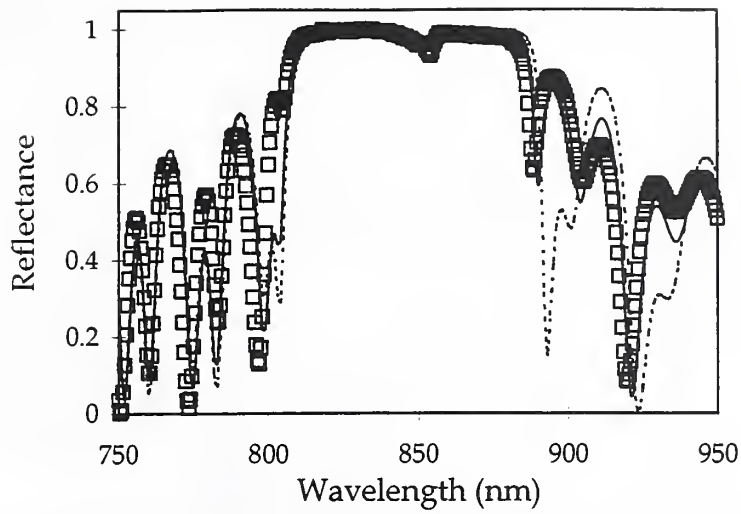

Figure 76: An example of the effect of compositional gradients in a VCSEL structure. Here, the uniform model is again the dashed line and the squares the data, but the solid line is the best fit using a compositional gradient of 8% over the AlGaAs layers.

That this situation corresponds to a change in *physical* thickness is evidenced in part by Fig. 76. The same reflectance data are here best fit by an 8% alloy composition gradient, in the same direction as the thickness gradient used previously. As a shift of 8% can be easily detected by XPL measurements on the two mirrors (or by depth profiling as documented in [10]), this comparison permits the conclusion that the gradient is indeed a physical thickness change.

B.2.2 Pump Field Weighting

For a multiple quantum well structure, the distribution of the optical pump field can also influence the relative amplitudes of the different emitters, since each quantum well will be excited in proportion to the magnitude of the pump field at its location. Following step 4 in the outline of Sec. B.1.2 above, each emitter in the final summation can be weighted according to the intensity of the pump field at its location.

Naturally, this weighting, and hence the emission, will change with the wavelength of the pump field. The difference between emission spectra weighted for different pump wavelengths is exemplified in Fig. 77. In this example, the intensities of the first two modes of the VCSEL drop by a factor of two when the device is pumped at 750 nm rather than 700. Though this model does take into account the absorption of the AlGaAs layers in the pump field weighting, it does not include any corrections for shifts in the AlGaAs index due to free carrier generation, which should be negligible if the modes do not shift considerably.

B.2.3 Angular Integration

Since any Fabry-Perot etalon changes its pass wavelength with angle, it is not surprising to expect a VCSEL to do the same thing. When the emission from a VCSEL is observed with a

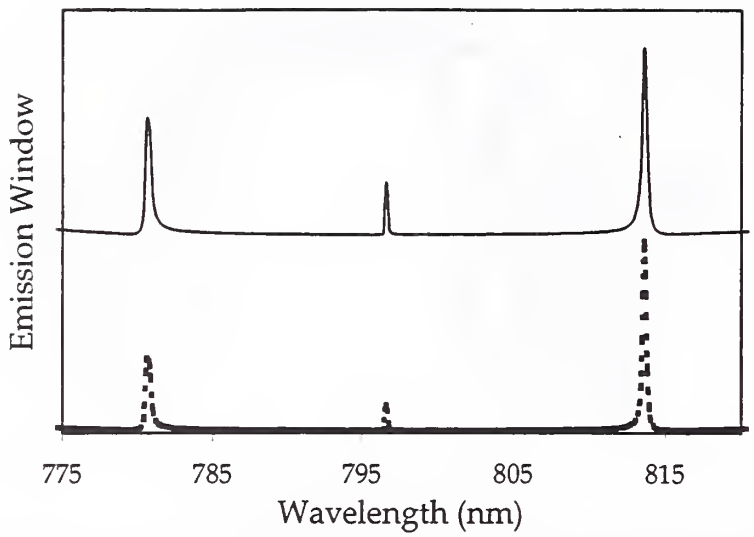

Figure 77: Pump-field emission weighting in a multimode, multiple (distributed) quantum well VCSEL. The solid line is the emission weighted for 700 nm excitation (with a baseline offset for clarity), the dotted line is the emission weighted for 760 nm pumping. Both curves are normalized to unity (at the mode peak near 813 nm), and the ratios of side mode peaks (700 nm excitation to 750 nm) in the two spectra are 0.6/1 (782 nm peak) and 0.5/1 (797 nm peak).

high-NA objective, the modeled response must be integrated over the whole collection angle.

When this is done for an ordinary mirror structure (embedded with quantum wells), the difference in spectra collected with two very different objectives (40× and 10×) is not overly remarkable. However, as shown in Fig. 78, the data for the simple mirror contains the same features as in the model (Fig. 79).

The situation for a VCSEL is somewhat different. As expected, the data show a broadening with increasing collection angle, which is limited to wavelengths shorter than the low-angle peak (Fig. 80). This is exactly what is expected of an etalon: the pass wavelength is reddest at normal incidence. Not coincidentally, the model shows the same broadening (Fig. 81). The halfwidths of the various spectra also match quite well: In both the data and the model, the halfwidth increases by 3 nm.

Finally, the model used here incorporates only TE Fresnel coefficients, thus indicating that the emission is dominated by the TE modes. This is logical because the emission is generated by quantum wells, and in particular by the heavy-hole recombination, which is perforce polarized in the plane of the QW. Thus, the preferred polarization along a given line of propagation is that which will both preserve the exciton polarization and lie perpendicular to the propagation vector. The situation is depicted in Fig. 82. A propagation vector at a given angle θ can have two distinct linear polarizations: one which is purely TE with respect to the mirrors (ε_{TE} in the drawing) and one which is a mixture of TE and TM (ε_{TE+TM}). However, our selection rules for the heavy holes dictate that the radiation must be polarized in the plane of the QW, which presumably is also the plane of the mirrors. Thus the heavy holes do not produce TM radiation. The light holes can only produce TM,

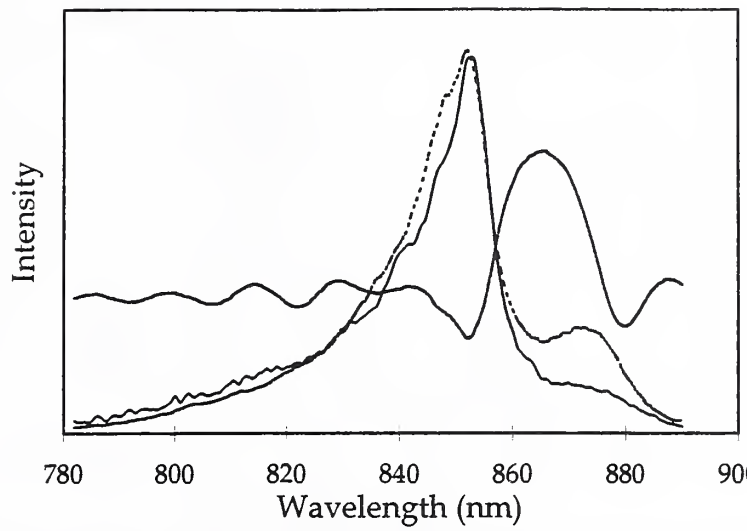

Figure 78: Emission spectra for a mirror stack embedded with quantum wells. Note the slight rise in the large-angle data (dotted line) on the long-wavelength side.

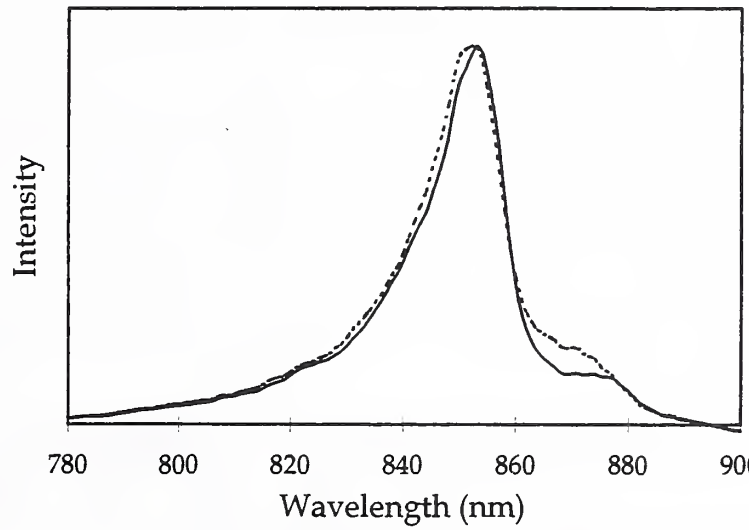

Figure 79: Emission model for the mirror stack. The slight rise in the large-angle data (dotted line) on the long-wavelength side is again present, corresponding to a dip in the reflectance (solid line).

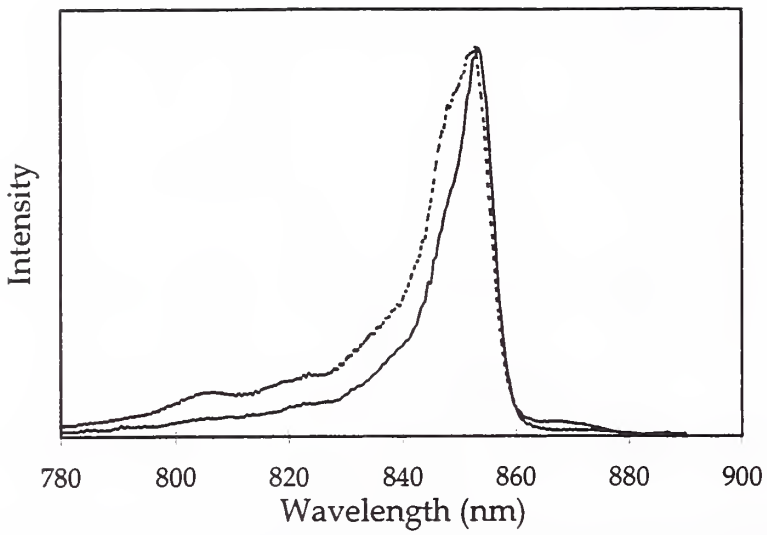

Figure 80: Emission spectra for a VCSEL (solid = 10×, dashed = 40×) showing the blue broadening characteristic of the Fabry-Perot structure.

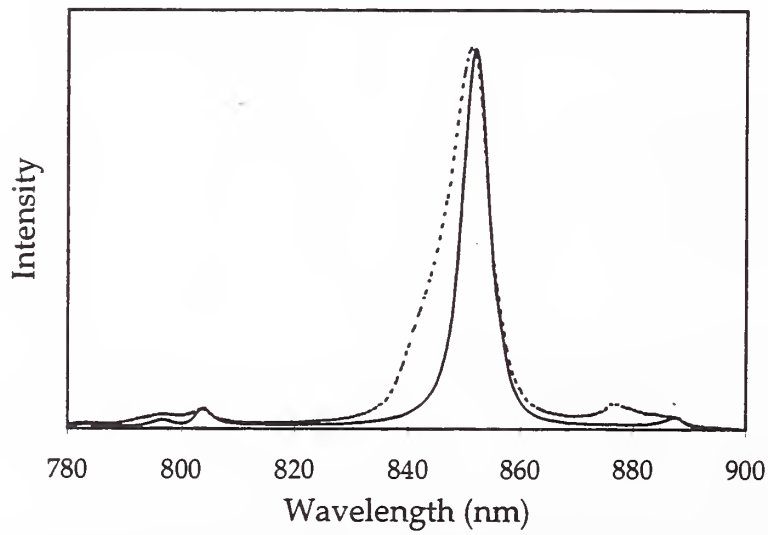

Figure 81: Emission model for the VCSEL structure (solid = 10×, dashed = 40×) showing the same blue broadening effect.

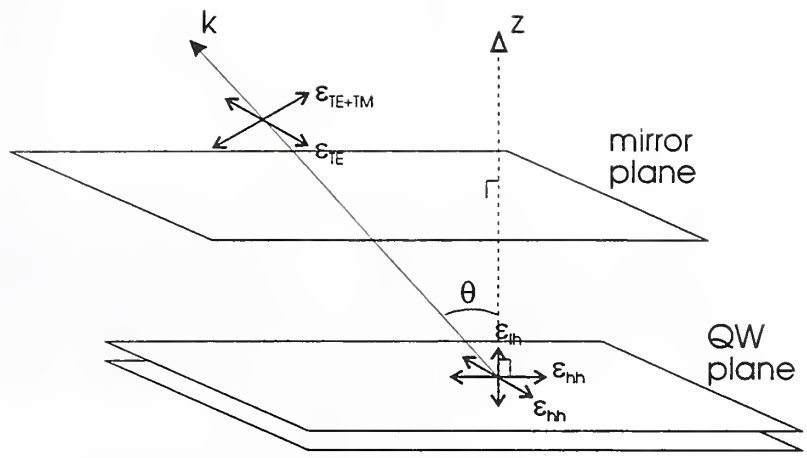

Figure 82: Surface-normal emission polarization from a VCSEL at a given angle θ. Heavy hole radiation is polarized in the plane of the QW, light holes perpendicular to it. The QW plane and the mirror planes are assumed to be parallel.

but they contribute little to the cavity modes (within the TIR angle), and obviously cannot contribute to the $\theta = 0$ emission since their radiation is polarized along that axis.

B.2.4 Coherent and Incoherent Summation

As stated earlier, the procedure in Sec. B.1.2 allows either incoherent (intensity) or coherent (field) summation of multiple emitters in a single structure. Coherent summation could be expected to apply if the emitters were close together, so that most of them would be within the average coherence length described by the spectral width of the spontaneous emission ($\Delta\nu = 1/\tau_c; \mathcal{L}_c = v\tau_c = c\tau_c/n$). For a QW typical of what has appeared in this work, with $\Delta\lambda = 18$ nm, $\Delta\nu \approx 8.25$ THz, the coherence time in air is only 0.1 ps, and the length in a material of index 3.5 or so is about 10 μm. As this is roughly the thickness of a typical VCSEL structure, it is worth investigating the impact of coherent emission on the mode spectrum.

The type of structure most likely to show strong evidence of this effect would be a multimode, distributed quantum well VCSEL, since the coherent coupling requires a series of quantum wells and since the DQW arrangement allows them to be spaced at $\lambda/2$ or $\lambda/4$ points, which would make the phase between emitters comparable to the round-trip phase in the cavity. Any interference effects from the coherent emission would then appear with such frequency as to be noticeable in the mode spectrum of a multimode device. The structures most suitable for this comparison then are a single-mode DQW VCSEL, a multimode $\lambda/2$-DQW VCSEL similar to the designs of Ch. 7, and a multimode $\lambda/4$-DQW VCSEL. Schematics of these structures are given in Fig. 83.

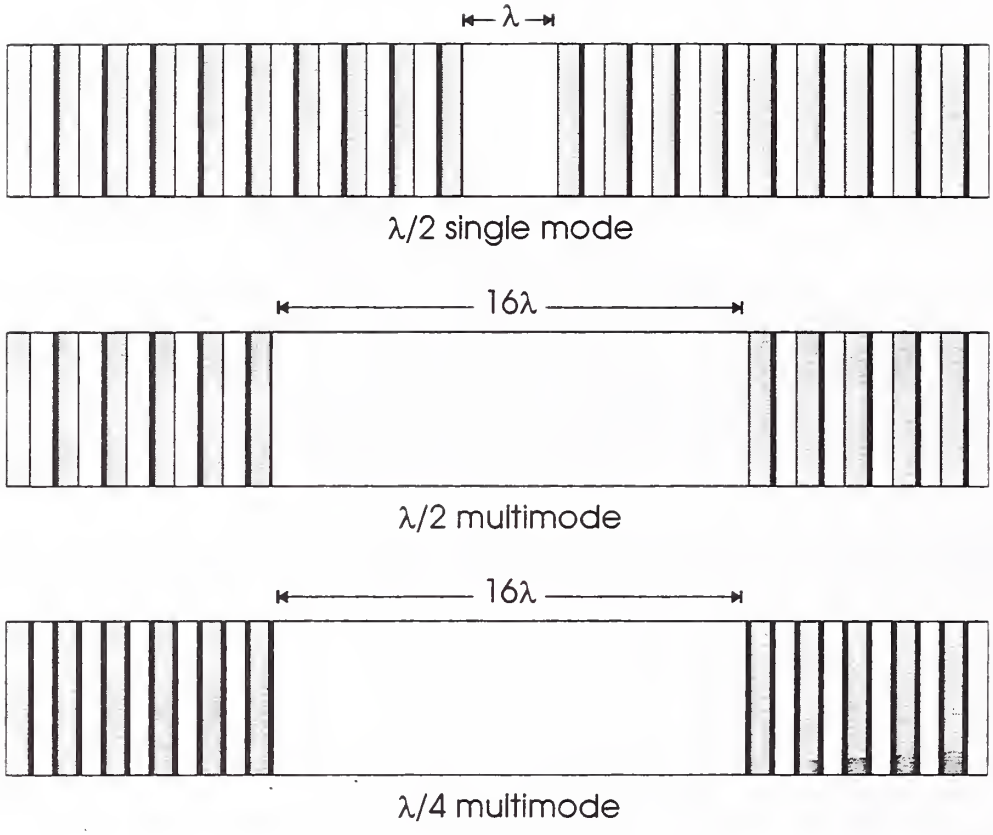

Figure 83: Schematics of the DQW VCSELs used in the modeling of emitter coherence. The top drawing is a single-mode VCSEL used as a control, the middle shows a multimode VCSEL with QWs in the mirrors spaced at $\lambda/2$, and the bottom is for a multimode VCSEL with the QWs spaced at $\lambda/4$.

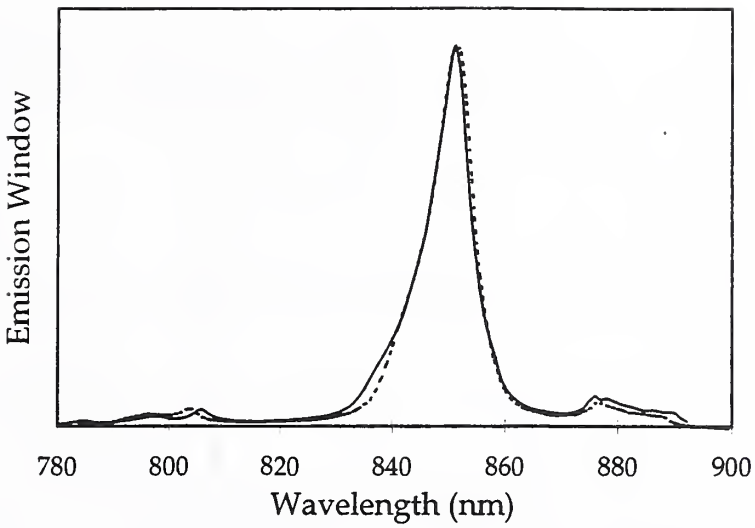

Figure 84: Emitter coherence in the single-mode DQW VCSEL structure. The solid line is the model which uses incoherent summation, the dashed line is the model which uses coherent summation of field amplitudes and phases.

Figure 84 shows the predicted emission for the single-mode VCSEL, illustrating that coherence between emitters does not have an impact on an isolated mode. In contrast, the effect on a multimode structure is quite profound, as shown in Fig. 85. Not only do the first two modes (at roughly 782 and 797 nm) drop in intensity when the emitter fields are added coherently, but the side modes (the broader peaks at either end of the spectrum) rise sharply. A similar effect occurs for the VCSEL with QWs spaced at $\lambda/4$ in the mirrors, as depicted in Fig. 86. The rise in the emission baseline from Fig. 85 to Fig. 86 is due to the increasing number of quantum wells in the structure and the impact of their absorption on the mirror reflectivity.

C Computing Energy Levels in Semiconductor Quantum Wells

In bulk material, the energy levels of the (degenerate) valence bands can be found from the Luttinger Hamiltonian, which includes the spin-orbit interaction, optionally including the $\mathbf{k} \cdot \mathbf{p}$ interaction to account for the crystal momentum. Neglecting the latter yields a simple dispersion for the energy levels of the doublet and quadruplet states, based on a set of effective masses:

$$\begin{aligned} J_z = \pm\frac{3}{2}: \quad & m_h/m_0 = 1/(\gamma_1 - 2\gamma_2) \\ J_z = \pm\frac{1}{2}: \quad & m_l/m_0 = 1/(\gamma_1 + 2\gamma_2), \end{aligned} \tag{57}$$

where γ_1 and γ_2 are the spin-orbit coupling (Luttinger) parameters for the material (proportional to interband coupling matrices). In a quantum well, however, treating the potential

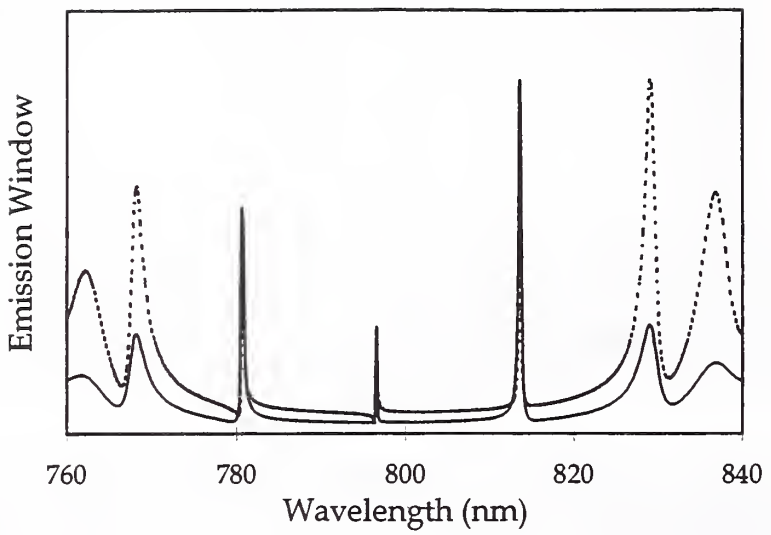

Figure 85: Emitter coherence in the multimode $\lambda/2$-DQW VCSEL structure. The solid line is the incoherent model, the dashed line is the coherent model. In the coherent model, the first two cavity modes (the narrowest lines) are roughly 1/2 and 1/10 the magnitude of the longest-wavelength mode.

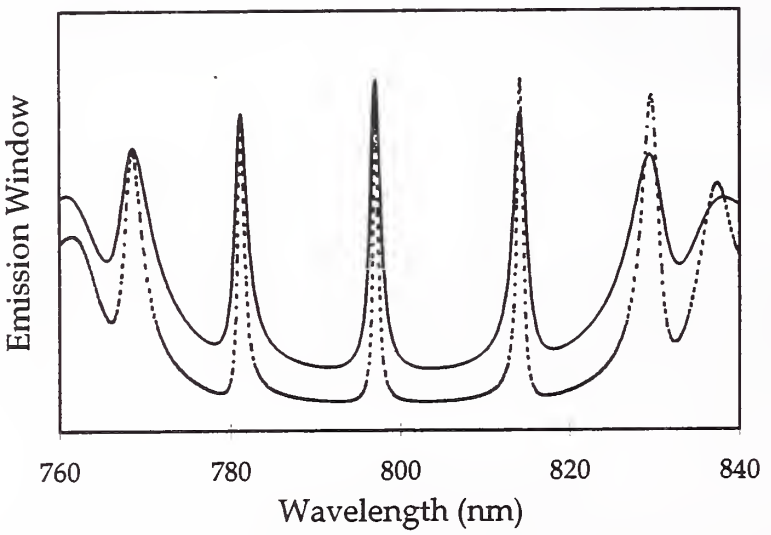

Figure 86: Emitter coherence in the multimode $\lambda/4$-DQW VCSEL structure. The solid line is the incoherent model, the dashed line is the coherent model.

variation to this Hamiltonian as a perturbation yields

$$J_z = \pm\frac{3}{2}: \quad m_h/m_0 = 1/(\gamma_1 + \gamma_2)$$
$$J_z = \pm\frac{1}{2}: \quad m_l/m_0 = 1/(\gamma_1 - \gamma_2), \tag{58}$$

This is the so-called "mass-reversal," where light holes become heavier than heavy ones in a quantum well. The first approximation to the energy levels in the well comes from solving

$$\mathcal{H} = \frac{-\hbar^2}{2\mu_\pm}\left[\frac{1}{\rho}\frac{\partial}{\partial\rho}\rho\frac{\partial}{\partial\rho} + \frac{1}{\rho^2}\frac{\partial^2}{\partial\phi^2}\right] - \frac{\hbar^2}{2m_e}\frac{\partial^2}{\partial z_e^2} - \frac{\hbar^2}{2m_\pm}\frac{\partial^2}{\partial z_h^2} - \frac{e^2}{\epsilon|\mathbf{r}_e - \mathbf{r}_h|} + \mathcal{V}_e(z_e) + \mathcal{V}_h(z_h), \tag{59}$$

in cylindrical coordinates, with $m_+(m_-)$ = heavy (light) hole effective mass along the quantization axis (as in Eq. 57, $\mu_+(\mu_-)$ = heavy (light) hole reduced mass in the plane of the quantum well, $\mathcal{V}_e(\mathcal{V}_h)$ = electron (hole) barrier potential, and ϵ is the dielectric constant. The assumption in using the transverse masses (Eq. 57) is that the quantization axis for the well is also a good quantization axis for the angular momentum of the particle. If the wavefunction is separable to the point where the boundary conditions can be applied on functions of z only, then the whole thing reduces to the normal case for a finite quantum well (with different masses in the well and in the barrier):

$$\kappa_{l,h}a = \begin{cases} k_{l,h}a\tan k_{l,h}a, & \text{even-parity solutions} \\ -k_{l,h}a\cot k_{l,h}a, & \text{odd-parity solutions} \end{cases}$$
$$k_{l,h}^2a^2 + (m^*_{(l,h),Q}/m_{(l,h),B})\kappa_{l,h}^2a^2 = \frac{2m^*_{(l,h),Q}V_0a^2}{\hbar^2}$$
$$\frac{\hbar^2}{2}\left(\frac{k_c^2}{m_c^*} + \frac{k_{l,h}^2}{m^*_{(l,h),Q}}\right) + \mathcal{E}_g = \mathcal{E}_{emis}. \tag{60}$$

$k_{l,h}$ is the wavenumber of the hole in the well, $\kappa_{l,h}$ is its wavenumber in the barrier, $2a$ is the thickness of the well, V_0 is the height of the barrier, and $m^*_{(l,h),Q}$ $(m^*_{(l,h),B})$ is the effective mass of the hole in the well (barrier). This model, as outlined by Greene, Bajaj and Phelps[161] and Bastard et al.[162], yields a fair agreement with the data of Miller et al.[163], especially if the exciton binding energy is taken into account.

Since the energy difference between the states depends intimately on the effective masses of the holes, it seems reasonable to look at the variation of these numbers in the literature. Table 7 lists a number of references for effective masses in GaAs, both in QWs and bulk material. The agreement on electron effective masses is very good and it is apparent that the QW and bulk masses are effectively the same. This is due to the accuracy of the parabolic approximation for the conduction band (i.e., that the electrons are more like free particles). The hole masses also do not change significantly between the bulk and QW cases (~ 0.08 to ~ 0.094 for light holes, ~ 0.34 to ~ 0.45 for the heavy), but the heavy hole mass shifts in the opposite direction predicted by the simple model.

The reason for this lies in the naïvity of the model. The actual problem for Bloch waves,

$$\psi_{\mathbf{k}}(\mathbf{r}) = u_{\mathbf{k}}(\mathbf{r})e^{i\mathbf{k}\cdot\mathbf{r}}, \tag{61}$$

Table 7: Effective masses in GaAs. † indicates low-temperature data. All data are for bulk materials, save for those denoted by ‡, which are QW or MQW data. The abbreviations for the method are: $\mathbf{k}\cdot\mathbf{p}$ = theoretical calculation using the $\mathbf{k}\cdot\mathbf{p}$ approach; CR = cyclotron resonance; IBMOA = inter-band magneto-optical absorption; MPC = magneto-photoconductivity; PLE = photoluminescence excitation; EHEC = electron/hole emission and capture; TS = transmission spectroscopy; and VC = varaitional calculation.

Reference for Data	Band Offset	Electrons	Holes		Method
		m_c/m_0	m_l/m_0	m_h/m_0	
Lawaetz[164]	–	0.067	0.074	0.62	$\mathbf{k}\cdot\mathbf{p}$
Braunstein†[165]	–	0.074	0.12	0.68	CR
Cardona[166]	–	0.07	0.1	1.0	$\mathbf{k}\cdot\mathbf{p}$
Vrehen†[167]	–	0.067	0.082	0.45	IBMOA
Stillman†[168]	–	0.0665	–	–	MPC
Mears†[169]	–	–	0.087	0.475	CR
Miller‡[163]	57/43	0.0665	0.094	0.34	PLE
Blakemore†[170]	–	0.067	0.084	0.47	EHEC
Ji‡[171]	67/33	–	0.094	0.34	TS (MQW)
Hrivnák‡[172]	69/31	0.074	0.099	–	VC

has a kinetic energy term that reduces to

$$\begin{aligned} -\hbar^2\hat{\nabla}^2\psi_{\mathbf{k}}(\mathbf{r}) &= -\hbar^2 e^{\imath\mathbf{k}\cdot\mathbf{r}}\left(\hat{\nabla}^2 u_{\mathbf{k}}(\mathbf{r}) + \imath\mathbf{k}\cdot\hat{\nabla}u_{\mathbf{k}}(\mathbf{r}) + \imath\hat{\nabla}u_{\mathbf{k}}(\mathbf{r})\cdot\mathbf{k} - k^2 u_{\mathbf{k}}(\mathbf{r})\right) \\ &= e^{\imath\mathbf{k}\cdot\mathbf{r}}\left(\imath\hbar\hat{\nabla} + \hbar\mathbf{k}\right)^2 u_{\mathbf{k}}(\mathbf{r}) \\ &= e^{\imath\mathbf{k}\cdot\mathbf{r}}(\mathbf{p} + \hbar\mathbf{k})^2 u_{\mathbf{k}}(\mathbf{r}). \end{aligned} \tag{62}$$

This amounts to correcting the particle momentum for the crystal momentum and can dramatically change the eigenvalues in a quantum well. In fact, the $\mathbf{k}\cdot\mathbf{p}$ interaction usually negates the mass-reveral effect.

On top of all this, the dominant recombination in quantum wells is excitonic, which means that the exciton binding energy is also released when the complex decays. Most often, the heavy hole binding is stronger than that for the light hole, but this does not cause a crossing of the emission levels. In GaAs QWs, the exact two-dimensional, infinite-barrier binding energy is about 4 QW Rydbergs, or about 12 to 16 meV (depending on the mass numbers used). In actual finite wells, the binding energy varies with the barrier composition and the width of the well; in the case of GaAs QWs in $Al_xGa_{1-x}As$, from about 1 to 3 Ryd, or about 3 to 12 meV. In any event, this is about 0.1% of the total energy of the system, so it is safe to neglect it in most cases.

Figure 87 shows the light- and heavy-hole splitting predicted by a simple model of a finite square well compared with XPL data on a number of QWs. The experimental thicknesses were taken from RHEED calibration and uncertainties are shown on the data points. The

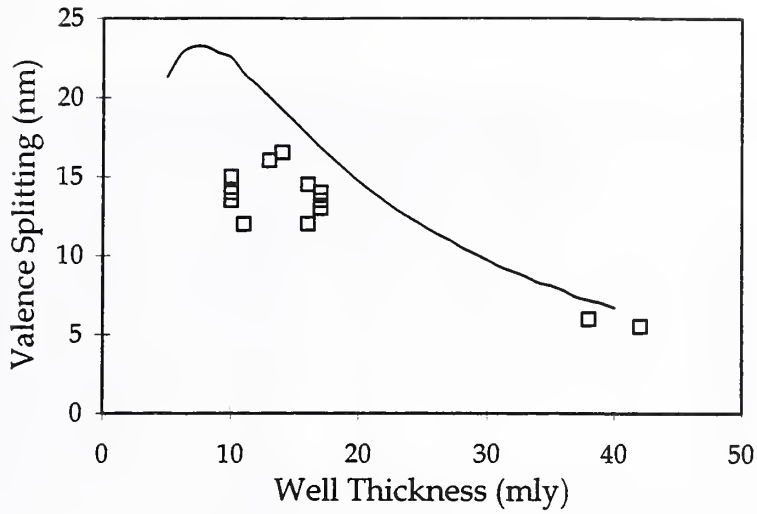

Figure 87: Comparison of XPL data on valence state splitting in QW emission energy and model as a function of well thickness (in monolayers). The barrier alloy composition in all cases was approximately 30% Al. The squares are the data; the solid line is the model. Exciton binding energies have been neglected.

effective masses used were those of Miller. If the experimental data are adjusted upward in thickness by roughly 8 mly, the fit to the model is significantly better, suggesting that either the masses are wrong or the RHEED thickness accuracy is lacking some eight monolayers. In any case, the data show that the splitting of the valence states can vary quite a bit for a given thickness (mostly due to interface problems in the thinner wells). Table 8 lists the specimens measured, along with both emission peaks, the fullwidth of those peaks, and the RHEED thickness.

In designing a VCSEL, the barrier composition is quite often the same as that used in the mirrors, so it is helpful to know what constraints are placed on the quantum well by the choice of AlGaAs alloy composition. As an example, Fig. 88 shows the energy shift of the light- and heavy-hole transitions as a function of well thickness. When the transition curves cross the straight line, the states become unbound, though electrons in the well can easily be thermalized beyond the barriers when the levels are very shallow. For comparison, the same data for a GaAs QW in pure AlAs barriers is shown in Fig. 89. Of course, changing the dimensions of the well also changes the number of bound states that it will support, as shown in Fig. 90. In most cases, the transitions of higher principal quantum number will have much lower transition strengths, effectively prohibiting band-to-band recombination from those states, but it is also possible to enhance those transitions (for example, with a cavity).

Changing the quantum well thickness is generally also a more accurate way to achieve the desired emission wavelength, and covers a much greater range (for a given barrier composition) than can be achieved by changing the barrier composition. As is evident from Fig. 91, even a thin well does not shift energy dramatically as the barrier composition moves. However, interface roughness or non-square barrier functions can have a pronounced impact on

Table 8: Table of XPL measurements on the hole emission from various QWs.

Specimen #	RHEED thickness (mly)	Predicted thickness (mly)	e_1-hh_1 peak (nm)	e_1-hh_1 FWHM (nm)	e_1-lh_1 peak (nm)	e_1-lh_1 FWHM (nm)
B063		10	774.5	15	760.5	33
B064		10	776	26	761	28
B068		11	781	29.5	769	20
B069		10	773.5	16	758.5	23
B070		10	776	16	762.5	19
B077		17	814	18.5	800	20
B079		14	801.5	15	785	18
B086		17	811.5	14	798	16
B090	18	14	797	13	785	—
B091	21	16	808.5	11.5	794	13
B092	21	16	807	12.5	795	17
B093	23	17	813.5	12.5	800.5	15
B094	19	13	795	14.5	779	18
N363		38	851	12	845	11.5
N471		42	854	15.5	848.5	15.5

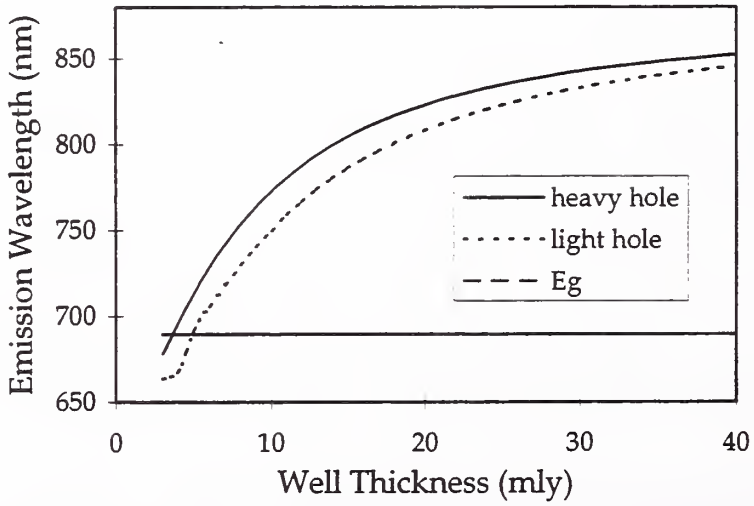

Figure 88: QW emission as a function of well thickness for a GaAs QW in $Al_{0.3}Ga_{0.7}As$, as predicted by the model described in the text. The horizontal line is the energy gap of the barrier.

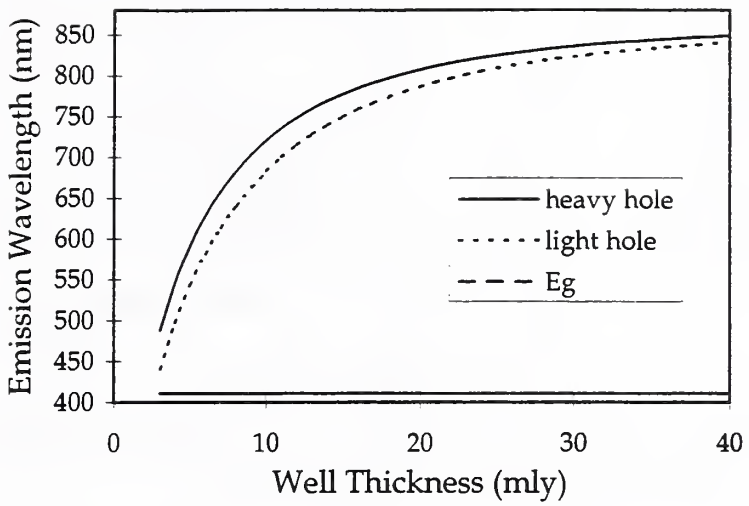

Figure 89: QW emission as a function of well thickness for a GaAs QW in AlAs, as predicted by the model described in the text. The straight line is the energy gap of AlAs.

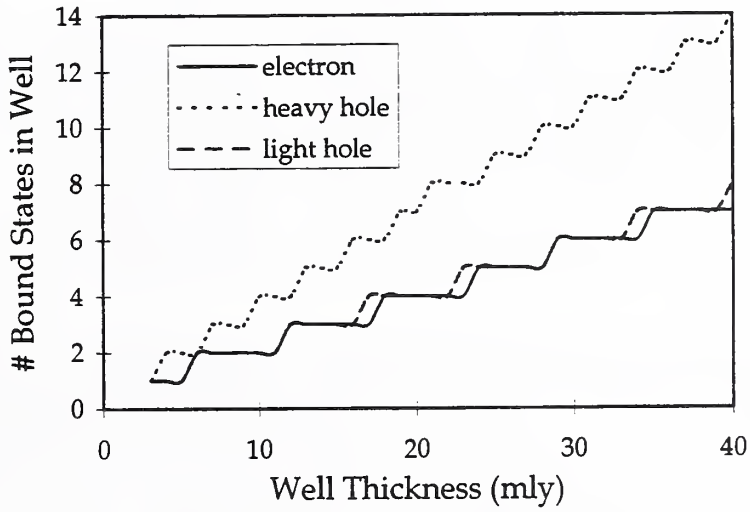

Figure 90: Bound states in a GaAs QW between AlAs barriers as a function of well thickness (in monolayers).

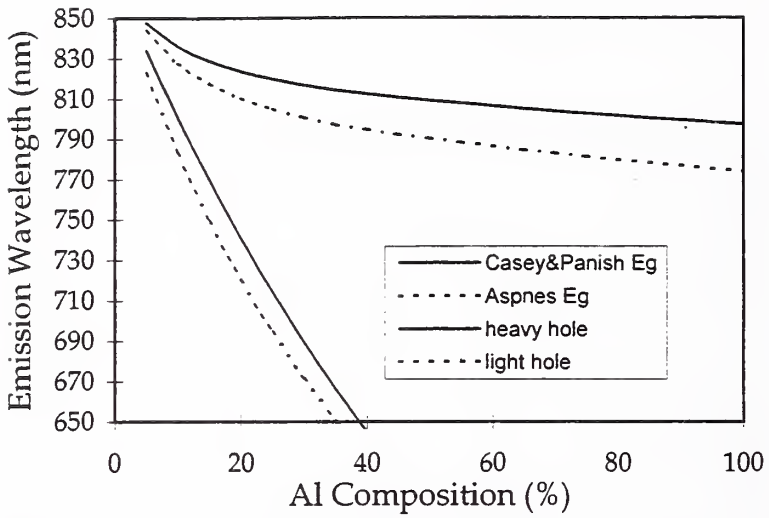

Figure 91: QW emission for an 18-monolayer GaAs well in AlGaAs barriers of varying composition. The lines nearest the left-hand vertical axis are two models of the energy gap of the barriers, indicating the depth of the bound states.

emission wavelengths as well as the sharpness of the peaks. For a VCSEL, this consideration is of much greater importance than the determination of the absolute barrier composition.

D The Image Method in Plane-Parallel Geometries

D.1 The Method of Images for a Fabry-Perot Etalon

The solution for the electromagnetic field inside a plane-parallel resonator can be solved directly using Fresnel analysis, as shown in Ch. 3, but there are other ways to arrive at the same result. One alternate method to the solving the problem is to use the method of images. Shown in the upper portion of Fig. 92 is a situation similar to the one depicted in Fig. 8: the dipole is located a distance $l_c - a$ from M_1 and a from M_2. It is simpler to do the problem using perfectly reflecting mirrors (and this is the approach taken in many examples in the literature[72, 74]); let us start here with the $R = 1$ case and later generalize this to $R \neq 1$.

The procedure for determining the locations and magnitudes of the images is simply to place an image to zero the potential on one mirror and then to compensate for that image on the other mirror with yet another image. According to the simple prescriptions in many electromagnetics texts (Jackson[136], for example), the solution for the field is strictly valid only in the "region of interest," usually taken to mean the space where no images are present. In this case, that interpretation restricts the solution to the space inside the mirrors.

I_1 corrects the potential on M_1 due to the source Q_0; it must be placed $2l_c - 2a$ from the origin because the dipole Q_0 (at the origin) is $l_c - a$ from M_1 and it must be negative (point down) because Q_0 is positive (points up). Similarly, I_2 performs the same service for M_2. I_3 is then the compensating image for I_2 across M_1 and I_4 accounts for I_1 across M_2. Table 9

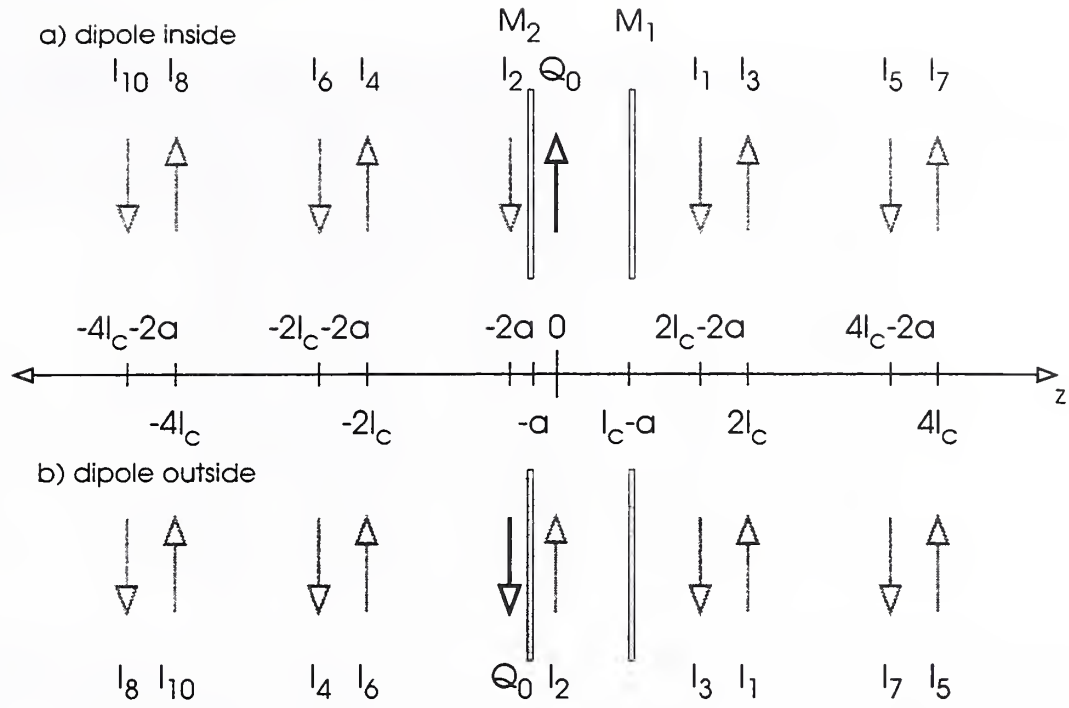

Figure 92: Image series for a dipole located (a) inside and (b) outside a Fabry-Perot cavity.

lists the first 10 images according to this formula.

Writing down the sum of all the fields from all of these dipoles, at a point ρ from the origin, gives:

$$\begin{aligned} E_k(\rho,t) \;=\; E_0 e^{\imath(k\rho-\omega t)}\Bigg[&\frac{1}{\rho} - \frac{e^{-\imath k(2\delta_C-2\delta_2)}}{\rho-2\delta_C+2\delta_2} - \frac{e^{\imath k2\delta_2}}{\rho+2\delta_2} + \frac{e^{-\imath k2\delta_C}}{\rho-2\delta_C} + \frac{e^{\imath k2\delta_C}}{\rho+2\delta_C} \\ &- \frac{e^{-\imath k(4\delta_C-2\delta_2)}}{\rho-4\delta_C+2\delta_2} - \frac{e^{\imath k(2\delta_C+2\delta_2)}}{\rho+2\delta_C+2\delta_2} + \frac{e^{-\imath k4\delta_C}}{\rho-4\delta_C} + \frac{e^{\imath k4\delta_C}}{\rho+4\delta_C} \\ &- \frac{e^{-\imath k(6\delta_C-2\delta_2)}}{\rho-6\delta_C+2\delta_2} - \frac{e^{\imath k(4\delta_C+2\delta_2)}}{\rho+4\delta_C+2\delta_2} + \cdots\Bigg]. \end{aligned} \tag{63}$$

The far-field version has been used here, but we might as easily substitute the full near-field expression. However, the same difficulty with summation as encountered above (Sec. 3.3.2) still applies to Eq. 63, except that in the case of perfect reflectors, there is no means of approximating the series as we did before (the series only decays by its $1/(\rho - m\alpha)$ dependence).

D.2 The Region of Interest

If this formalism is used to solve the problem illustrated in Fig. 92b, for the dipole outside the cavity, the series is identical to Eq. 63. Thus, if the source is interchanged with one of the images (I_2 in this case), the only difference in the series is the ordering of the images: in

Table 9: Table of images for a dipole inside a Fabry-Perot cavity.

Image (magnitude)	Corrects for (magnitude)	Across Mirror	Location (case a)
I_1 $(-)$	Q_0 $(+)$	M_1	$2l_c - 2a$
I_2 $(-)$	Q_0 $(+)$	M_2	$-2a$
I_3 $(+)$	I_2 $(-)$	M_1	$2l_c$
I_4 $(+)$	I_1 $(-)$	M_2	$-2l_c$
I_5 $(-)$	I_4 $(+)$	M_1	$4l_c - 2a$
I_6 $(-)$	I_3 $(+)$	M_2	$-2l_c - 2a$
I_7 $(+)$	I_6 $(-)$	M_1	$4l_c$
I_8 $(+)$	I_5 $(-)$	M_2	$-4l_c$
I_9 $(-)$ (not shown)	I_8 $(+)$	M_1	$6l_c - 2a$
I_{10} $(-)$	I_7 $(+)$	M_2	$-4l_c - 2a$

Fig. 92b, the positions of the pairs I_1 and I_3, I_4 and I_6, I_5 and I_7, etc. have been reversed. One might conclude from this that this exchange of the dipole with one of its fictitious images would yield similar spectral results to an observer outside the cavity.

However, we have already made the caveat that this solution is valid only in regions where there are no images, and there are images in all three regions (as defined by the physical boundaries of the problem) of Fig. 92b. Yet the solution of Eq. 63 is very close to the correct solution derived in Ch. 3, especially if all the singularities (the $[\rho - m\alpha]^{-1}$ terms) are removed. Still, if the dipole is placed outside the cavity and the singularities are discarded, the resulting expression still contains a dependence on the dipole's position:

$$\frac{E_k}{E_0} = \left[\frac{1}{\rho} - \frac{e^{\imath k 2\delta_2}}{\rho + 2\delta_2} + \frac{e^{\imath k 2\delta_C}}{\rho + 2\delta_C} - \frac{e^{\imath k(2\delta_C + 2\delta_2)}}{\rho + 2\delta_C + 2\delta_2} + \frac{e^{\imath k 4\delta_C}}{\rho + 4\delta_C} - \frac{e^{\imath k(4\delta_C + 2\delta_2)}}{\rho + 4\delta_C + 2\delta_2} + \cdots\right]. \tag{64}$$

In addition, what does the region of interest restriction mean when dielectrics are involved and images must be placed at the location of the source? Is it invalid to define an arbitrarily small region of interest outside the cavity (avoiding the singularities) or do the physical boundaries of the problem still define the region of interest (even though the image method is designed to allow them to be removed). Even if the original region of interest restriction applies, can the image method be modified to give a valid result (say by removing the singularities in the region of interest)?

This last question deserves some attention. By removing all the images on the observation side of the cavity, we have essentially taken out all the fields which are unphysical — that is, all those which emanate from distances closer to the observation point than the direct ray to the real source. The image charges on the observation side of the cavity have stronger fields than the source itself, so it is logical to discard them on this basis. As we shall see shortly,

Table 10: Table of images for a dipole and a Fabry-Perot cavity with imperfect mirrors, based on the plane-wave of amplitude r^m assumption. The "valid outside" field indicates whether or not the image causes a singularity and must be discarded when the cavity is observed from the outside.

Image	location	magnitude	valid outside?
I_1	$2l_c - 2a$	r_1	no
I_2	$-2a$	r_2	yes
I_3	$2l_c$	$r_1 r_2$	no
I_4	$-2l_c$	$r_1 r_2$	yes
I_5	$4l_c - 2a$	$r_1^2 r_2$	no
I_6	$-2l_c - 2a$	$r_1 r_2^2$	yes
I_7	$4l_c$	$r_1^2 r_2^2$	no
I_8	$-4l_c$	$r_1^2 r_2^2$	yes
I_9	$6l_c - 2a$	$r_1^3 r_2^2$	no
I_{10}	$-4l_c - 2a$	$r_1^2 r_2^3$	yes

this approach also falls short of validity.

D.3 Partially-Reflecting Mirrors

The problem of image magnitudes for partially-reflecting mirrors has only been treated sparsely in the literature, from my survey, and the clearest treatment there is that of Stehle[66]. He makes the assumption that the field of the m^{th} image can be described by a plane wave of amplitude R^m. If that same hypothesis is used here, taking the prescription for unequal mirrors to be one factor of r_i each time the correction "goes across" mirror i, then the series is as given in Table 10.

In this case the series is (with the observation-side images removed)

$$\begin{aligned}\frac{E_k}{E_0} = & \left[\frac{1}{\rho} - r_2\frac{e^{\imath k2\delta_2}}{\rho+2\delta_2} + r_1 r_2\frac{e^{\imath k2\delta_C}}{\rho+2\delta_C}\right. \\ & \left. - r_1 r_2^2\frac{e^{\imath k(2\delta_C+2\delta_2)}}{\rho+2\delta_C+2\delta_2} + r_1^2 r_2^2\frac{e^{\imath k4\delta_C}}{\rho+4\delta_C} - r_1^2 r_2^3\frac{e^{\imath k(4\delta_C+2\delta_2)}}{\rho+4\delta_C+2\delta_2} + \cdots\right],\end{aligned} \tag{65}$$

and if the plane-wave approximation is made here, the series can be summed to yield

$$\frac{E_k}{E_0} = \frac{1 + r_2 e^{\imath 2\delta_2}}{1 - r_1 r_2 e^{\imath 2\delta_C}}, \tag{66}$$

which is precisely the formula derived by Fresnel analysis, save for the absence of a multiplicative factor of t_1. A clue to the meaning of its absence may be deduced from the fact that this factor is not present in the Fresnel analysis for the field inside the cavity.

Thus, there is some reason to suspect that a modified image construction would yield a valid result, but before examining that possibility, let us first look at the assumption made about the magnitudes of the images. As shown in Jackson[136, pp. 147 ff.], the magnitudes of the image charges for a single dielectric interface are:

$$\begin{aligned} q' &= -\left(\frac{\epsilon_2 - \epsilon_1}{\epsilon_2 + \epsilon_1}\right) q \\ q'' &= \left(\frac{2\epsilon_2}{\epsilon_2 + \epsilon_1}\right) q. \end{aligned} \tag{67}$$

These formulas are arrived at by solving the boundary value problem for the set of charges, which is completely analogous to the manner in which Fresnel coefficients are derived. Thus, if we have an oscillating dipole and its image on either side of an imperfect mirror, the logical result is to have two images, one at the mirror point across the mirror and one at the position of the source, of magnitude given by the Fresnel coefficients. Specifically, if a single interface is considered, then there are three fields which must satisfy the boundary conditions (continuity of parallel components of **E** and **H**): the incident, reflected, and transmitted waves. This constraint is satisfied by placing an image dipole of magnitude r across the mirror and one of magnitude t at the position of the source (this convention is chosen because the phase of the image dipoles shown in Fig. 92 is consistent with reflection rather than transmission).

Now the situation becomes much more complex. We have an increasing number of images to contend with, as shown in Tables 11 and 12. This construction contains several correct behaviors: The transmission coefficients are included, the valid terms change from t_1 to t_2 when the observation side is changed, and the r factors again follow the proper geometric progression. On the other hand, the leading terms in this series do not contain a t_1 or t_2 dependence, which they clearly must since the light must escape the cavity.

At this point it is fairly safe to say that even if there is some question as to the amplitudes, the basic construction remains the same. The locations and phase factors of the images do not change when the mirrors drop from $R = 1$ to a lower value. The importance of this result is that the localization sensitivity persists with the locations (and phases) of the images.

Thus, if there is some image construction which gives a valid result outside the cavity, we suspect that it would have a localization sensitivity as in Eq. 65. If this construction continues to give valid results when the dipole is moved outside the cavity, then that same sensitivity to the position of the dipole relative to the cavity would remain intact. This is certainly something that can be tested experimentally.

D.4 Experimental Results

Some of the data pertinent to this discussion have already been presented in Ch. 6. Figures 41 and 42, the pulsed transmission data for the dipole inside and outside the cavity, represent exactly the sort of test needed to verify the localization sensitivity associated with the image solution presented in the preceeding section.

Table 11: Table of images for a dipole and a Fabry-Perot cavity with imperfect mirrors, using the exact prescription for dielectrics. The "valid outside" field indicates whether or not the image causes a singularity and must be discarded when the cavity is observed from the outside, beyond mirror 1.

Image	Mirror	Corrects for/ location	magnitude	valid outside?
I_1	Q_0/M_1	$2l_c - 2a$	r_1	no
I_1'	Q_0/M_1	0	t_1	yes?
I_2	Q_0/M_2	$-2a$	r_2	yes
I_2'	Q_0/M_2	0	t_2	yes?
I_3	$I_2/M1$	$2l_c$	r_1r_2	no
I_3'	I_2/M_1	$-2a$	t_1r_2	yes
I_3''	I_2'/M_1	$2l_c - 2a$	r_1t_2	no
I_3'''	I_2'/M_1	0	t_1t_2	yes?
I_4	I_1/M_2	$-2l_c$	r_1r_2	yes
I_4'	I_1/M_2	$2l_c - 2a$	r_1t_2	no
I_4''	I_1'/M_2	$-2a$	t_1r_2	yes
I_4'''	I_1'/M_2	0	t_1t_2	yes?
I_5	I_4/M_1	$4l_c - 2a$	$r_1^2r_2$	no
I_5'	I_4/M_1	$-2l_c$	$t_1r_1r_2$	no
I_5''	I_4'/M_1	0	$r_1^2t_2$	yes?
I_5'''	I_4'/M_1	$2l_c - 2a$	$t_1r_1t_2$	no
I_5^{iv}	I_4''/M_1	$2l_c$	$t_1r_1r_2$	no
I_5^{v}	I_4''/M_1	$-2a$	$t_1^2r_2$	yes
I_5^{vi}	I_4'''/M_1	$2l_c - 2a$	$t_1r_1t_2$	no
I_5^{vii}	I_4'''/M_1	0	$t_1^2t_2$	yes?

Table 12: Table of images for a dipole and a dielectric Fabry-Perot cavity with imperfect mirrors, showing only the series of images which corrects for the principal (unprimed) images.

Image	Mirror	Corrects for/ location	magnitude	valid outside?
I_1	Q_0/M_1	$2l_c - 2a$	r_1	no
I'_1	Q_0/M_1	0	t_1	yes?
I_2	Q_0/M_2	$-2a$	r_2	yes
I'_2	Q_0/M_2	0	t_2	yes?
I_3	$I_2/M1$	$2l_c$	r_1r_2	no
I'_3	I_2/M_1	$-2a$	t_1r_2	yes
I_4	I_1/M_2	$-2l_c$	r_1r_2	yes
I'_4	I_1/M_2	$2l_c - 2a$	r_1t_2	no
I_5	I_4/M_1	$4l_c - 2a$	$r_1^2r_2$	no
I'_5	I_4/M_1	$-2l_c$	$t_1r_1r_2$	no
I_6	I_3/M_2	$-2l_c - 2a$	$r_1r_2^2$	yes
I'_6	I_3/M_2	$2l_c$	$r_1r_2t_2$	no
I_7	I_6/M_1	$4l_c$	$r_1^2r_2^2$	no
I'_7	I_6/M_1	$-2l_c - 2a$	$t_1r_1r_2^2$	yes
I_8	I_5/M_2	$-4l_c$	$r_1^2r_2^2$	yes
I'_8	I_5/M_2	$4l_c - 2a$	$r_1^2r_2t_2$	no
I_9	I_8/M_1	$6l_c - 2a$	$r_1^3r_2^2$	no
I'_9	I_8/M_1	$-4l_c$	$t_1r_1^2r_2^2$	yes
I_{10}	I_7/M_2	$-4l_c - 2a$	$r_1^2r_2^3$	yes
I'_{10}	I_7/M_2	$4l_c$	$r_1^2r_2^2t_2$	no

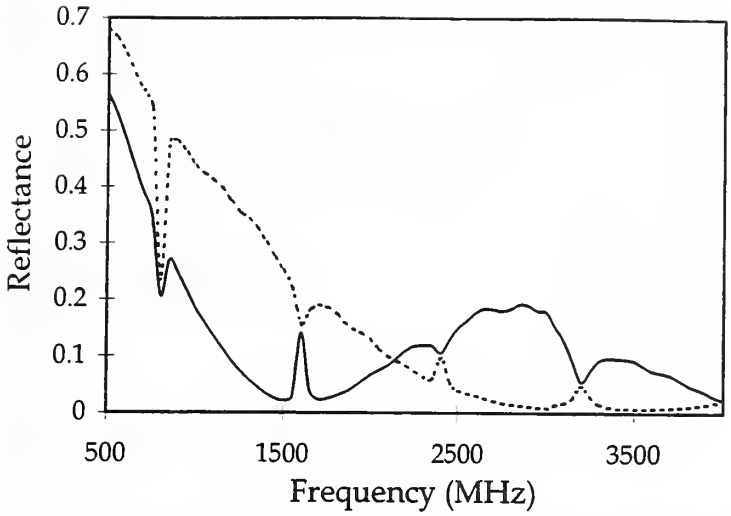

Figure 93: Predicted optical reflection spectrum for the microwave cavity.

As the reader may recall, Fig. 41, for the antenna at two different positions inside the cavity, showed a strong localization dependence in the emission spectrum which followed the predictions arrived at through Fresnel analysis. Figure 42, the spectra for the antenna outside the cavity, did not show any dependence on the antenna position at all. This is the antithesis of the prediction of the image constrution.

Though this evidence gives strong indication that this modified image method does not work, there is yet another test whose results ought to give conclusive evidence. The image construction predicts a reflection spectrum which looks very much like the transmission spectrum, as opposed to a normal reflection spectrum for a Fabry-Perot etalon. Yet the reflection spectrum predicted by Fresnel analysis more closely resembles the usual Fabry-Perot reflectance. Therefore, a simple reflectance measurement, with the antenna in front of the cavity, ought to clarify this distinction immediately.

The reflection spectrum predicted by counting waves (as in Sec. 3.3.1) is not independent of source location when the source itself is visible to the detector and very close to the cavity. This prediction, as shown in Fig. 93, is of an entirely different character than those for the transmission spectrum, whether for the dipole inside (Fig. 39) or outside (Fig. 40).

The reflection spectra for the monopole outside the cavity (Fig. 94), however, show that the reflectance measurement is not quite as straightforward as the transmittance measurement in the time domain. While there are some differences in the two spectra for half- and quarter-cavity-length spacings, much of the signal is washed out by the very large direct pulse, which distorts the ratio between itself and subsequent pulses.

However, the reflection spectra in Fig. 94 quite clearly do not match the predictions of the image method (Fig. 39) as well as they do those of the standard wave-counting method (Fig. 93). Not only does the symmetry of exchanging a dipole with one of its fictitious images not exist, but the image construction used to arrive at this hypothesis must be flawed as well. In light of this, it is sensible to ask why.

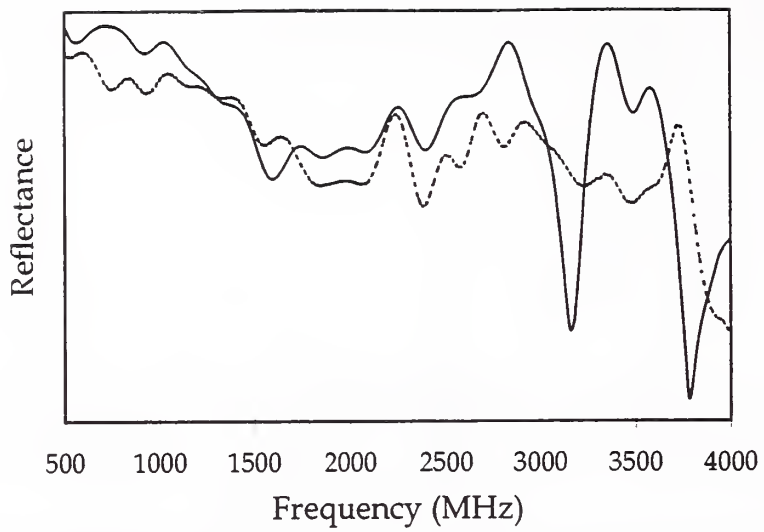

Figure 94: Optical reflection spectra for the monopole outside the cavity. The solid line is a half-cavity-length spacing in front of the cavity, dashed is a quarter-cavity-length.

D.5 Return to Validity

The parallel-plate resonator problem (from the standpoint of images) can actually be viewed as an evolution of the problem of the standard point dipole in front of a mirror, as depicted in Fig. 95. As the mirrors bend around to form a plane-parallel system, the region of interest remains isolated inside them, and the original half-space where the solution is valid is condensed into a wedge and then eventually a slab.

Put simply, the physical boundaries of the problem define the region of interest or the region of validity for the image method and there appears to be no way around this restriction. Though it is tempting to think of the infinite series of Eq. 14 as a series of images (especially since this is one of the only problems of simple geometry in electrostatics which requires an infinite series of images), there does not seem to be a rigorous (or obvious) connection between conventional image theory and such an ad-hoc hypothesis.

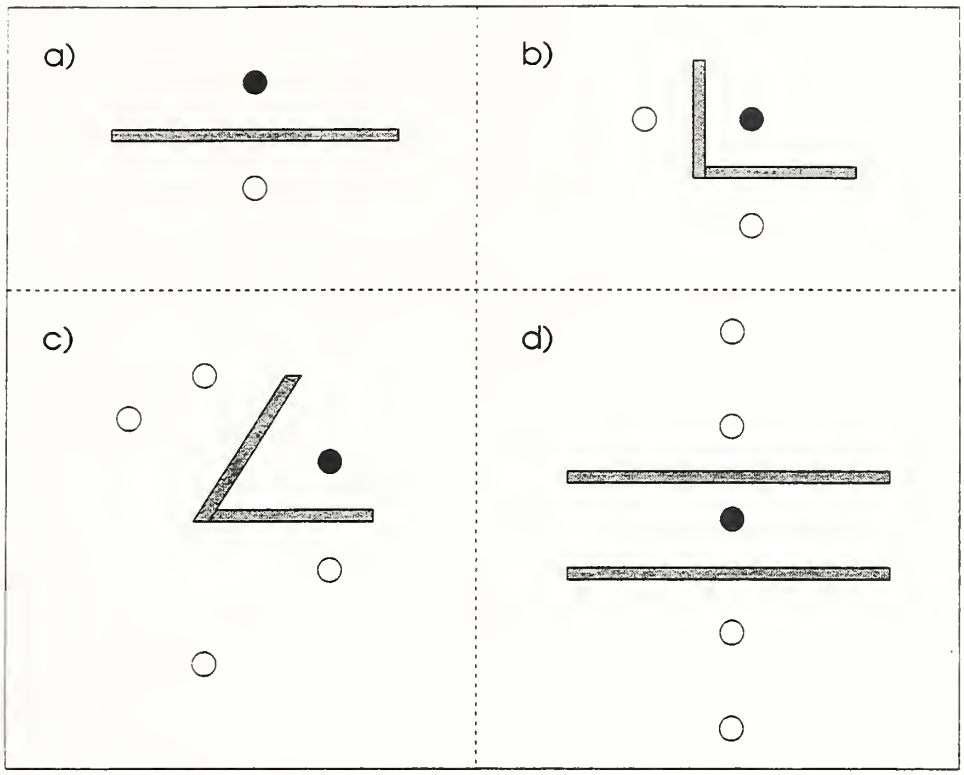

Figure 95: The evolution of the plane-parallel image construction from that for a single mirror. The top-left drawing (a) shows an isolated dipole and its image for an infinite plane mirror. The next (b) is the image construction for a bent mirror opening at a right angle, now having two images. The solution with two images works for opening angles $\geq \pi/2$, but acute opening angles (c) generate a larger number of images, gradually becoming infinite as the mirror planes become parallel and their junction is allowed to open (d). This also helps to clarify the region of interest, as discussed in the text.